RICE UNIVERSITY

Engineering nanoparticle-protein associations for protein crystal nucleation and nanoparticle arrangement

by

Denise N. Benoit

A THESIS SUBMITTED
IN PARTIAL FULFILLMENT OF THE
REQUIREMENTS FOR THE DEGREE

Doctor of Philosophy

APPROVED THESIS COMMITTEE

Dr. Vicki Colvin, Chair
Kenneth S. Pitzer-Schlumberger Professor, Chemistry
Vice Provost for Research

Dr. Yousif Shamoo
Associate Professor, Biochemistry and Cellular Biology
Wiess Career Development Chair
Director, Institute of Biosciences and Bioengineering

Dr. Jeffrey Hartgerink
Associate Professor, Chemistry

HOUSTON, TEXAS

ABSTRACT

Engineering nanoparticle-protein associations for protein crystal nucleation and nanoparticle arrangement

By

Denise N Benoit

Engineering the nanoparticle - protein association offers a new way to form protein crystals as well as new approaches for arrangement of nanoparticles. Central to this control is the nanoparticle surface. By conjugating polymers on the surface with controlled molecular weights many properties of the nanoparticle can be changed including its size, stability in buffers and the association of proteins with its surface. Large molecular weight poly(ethylene glycol) (PEG) coatings allow for weak associations between proteins and nanoparticles. These interactions can lead to changes in how proteins crystallize. In particular, they decrease the time to nucleation and expand the range of conditions over which protein crystals form. Interestingly, when PEG chain lengths are too short then protein association is minimized and these effects are not observed. One important feature of protein crystals nucleated with nanoparticles is that the nanoparticles are incorporated into the crystals. What results are nanoparticles placed at well-defined distances in composite protein-nanoparticle crystals. Crystals on the size scale of 10 - 100 micrometers exhibit optical absorbance, fluorescence and super paramagnetic behavior derivative from the incorporated nanomaterials. The arrangement of nanoparticles into three dimensional arrays also gives rise to new and interesting

physical and chemical properties, such as fluorescence enhancement and varied magnetic response. In addition, anisotropic nanomaterials aligned throughout the composite crystal have polarization dependent optical properties.

ACKNOWLEDGMENTS

This thesis is dedicated to my family; Jason, Annabelle and my parents.

I would like to first acknowledge my advisor, Vicki Colvin, for allowing me the opportunity to learn and grow under her guidance. The encouragement, creative perspective and freedom she has provided over the years have given me a unique opportunity to develop a cross disciplinary project that has made me a more rounded and independent scientist.

Next, I have had the honor of spending four years in a multidisciplinary training program through the Gulf Coast Consortium. It was through this fellowship that I first got to work with Dr. Yousif Shamoo. I have really enjoyed the perspective of being integrated into two laboratories. I thank the Keck Center for allowing me to be a part of your wonderful training program. In addition, I really appreciated the open door feeling that Dr. Shamoo has provided and thank him for so many discussions and conversations. He exposed me to biology and structural biology techniques and effectively launched my project into new and exciting directions.

My deepest gratitude and thanks go to those I have had the opportunity to call colleagues over the past 6 years; particularly members from the Colvin, Shamoo, and Hafner Labs. The amount of knowledge, guidance, support, experience, and life experiences I have gained from these people are too numerous to mention. Special acknowledgment to a few: Dr. Huiguang Zhu, he has helped produce many of the materials and methods used within my project, his research ideas and suggestions are always thought provoking and I

appreciate his willingness to sit and explain them over a cup of coffee or breakfast taco when necessary. Dr. Carolina Avendano has provided an amazing ‘can-do’ attitude to the Colvin lab and changed the work environment for the better; she has brought knowledge and understanding to some of the most complex topics in my research. Dr. Zuzanna Lewicka, has been a wonderful collaborator and I appreciated her hard work, quick turn around and brutal honesty. Teresa Champion, she may not have collaborated on data collection, but she has provided more answers and help than anyone else. She is an asset to the Colvin Lab and I appreciate all that she has done for me

Collaborators outside the Colvin Lab include Kasia Walkiewicz from the Shamoo lab, and Courtney Payne from the Hafner Lab. Kasia I would like to thank for her patience and never saying to my face that I am stupid for not knowing how to pour a gel or mount a crystal. Courtney Payne, I will forever be grateful for her materials, methods, and exposure to the physical elements in my project, and I commend her on an amazing attention to detail and unwavering pursuit of perfection.

I have had the honor of mentoring a set of undergraduate researchers that I would like to thank for their hard work: Montoya Savala, Ajoke Williams, Raymond Verm, Gustavo Resendiz, Michael Lillierose and Naushaba Ali.

I am grateful to the SEA staff; Dr. Wenhua Guo, Angelo Bendetto, Bo Chen and Chris Pennington for the extensive amount of instrument training, support, guidance and maintenance they have to do to keep everyone at Rice working.

Beyond research and classes, in graduate school I have also learned to love teaching and connecting with the community. For that I thank: Dr. Mary McHale, Dr. Carolyn

Nichol, Dr. John Hutchinson, Dr. Bruce Wiseman, Dr. Michelle Gilbertson, Dr. Kristen Kulinowski, and Dr. Crystal Weber.

Thank you to the people that have made this time in graduate school so bearable, my friends: Amanda, Eoghan, Sophia, Alvin, Jorge, Lesley, Nicky, Jonathan, Kelley, Elizabeth, JT, Erika, Arjun, Chris, Seung Soo, Ming Jung, Hema, Natalia, Gabby, Arash, Nasim, John,

Last but not least is my amazing supportive family which includes my parents, sister and her family, brothers and their families. I am probably one of the only graduate students that had her whole family get involved in her project. Not only did my mom spark in me a strong set of basic inquiry skills but she helped me write and edit this entire thesis, as well as work in the lab with me on occasion when she has come to visit. My brother Jeremy, the math guru wizard extraordinaire, typed up the equations in Chapter 3, and sat on the phone guiding me though radial distribution functions, while bunkered down due to tornados! I thank my sister, Jessica, for her encouragement, understanding and assistance with computer graphic designs and figure layout. Her husband, Rich, for basic presentation skills and "word smithing" my best emails, letters and drafts. But more than anything I would like to acknowledge my wonderful, amazing, and brilliant husband and little girl. Jason is responsible for a number of the protein crystal pictures and all of my success. And Annabelle has to take credit for some of the discoveries, she did spend her first three months in the lab with me – I hope that means she will grow up with a love for science. I love you both, Jason and Annabelle.

CONTENTS

LIST OF FIGURES

LIST OF TABLES

LIST OF EQUATIONS

Chapter 1

LITERATURE REVIEW

Central to the work within this thesis is an understanding of how to control protein – nanoparticle associations though surface engineering of the particle with a grafted polymer. Preferential nanoparticle – protein associations are then applied to the nucleation of crystals and assembly of 3D nanoparticle arrangements.

1.1. PROTEIN – NANOPARTICLE ASSOCIATIONS

On a molecular level the biological response to any foreign object is the rapid adsorption of multitudes of proteins to the surface, and nanoparticles are no exception to this rule. Associations with any of the ~50,000 proteins in the human body will result in the formation of a dynamic coating around the particle known as the protein "corona".[3] Each protein's affinity for the nanoparticle surface dictates its presence in the corona which varies in quantity and length of time associated. Figure 1.1, from Lynch's paper Protein-

nanoparticle Interactions, *Nano Today,* is an illustration designed to emphasize the dynamic adsorption and desorption of proteins which work to create a complex protein corona that can constantly change. Essentially, it is the make-up of this corona that dictates the biological identity of any nanomaterial, controlling its trafficking, kinetics and clearance in the body. Therefore, developing an understanding of how to control the proteins that make up the corona has been the goal of researchers using nanoparticles in biological environments.

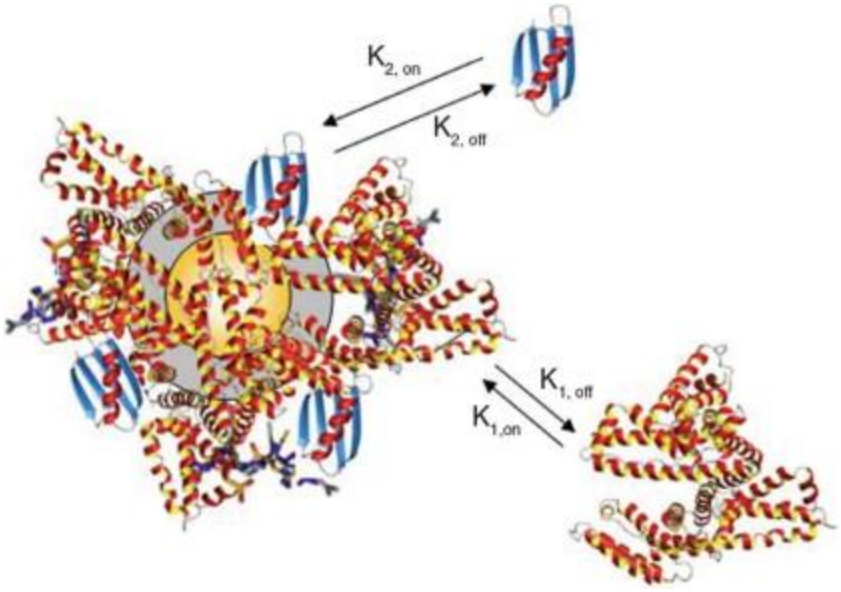

Figure 1.1. Protein corona.

Diagram representing the differences in exchange rates for the protein corona on a nanoparticle. The dynamic exchange of proteins on the surface and the surround media make the composition of the corona a complex function of the differences in exchange rates based on the proteins affinity for the surface. Figure from Lynch, Dawson Nano Today 2008, ref [3]

1.2. METHODS TO DETECT PROTEIN – NANOPARTICLE ASSOCIATIONS

Analytical approaches to uncover information about the protein corona include: determining binding affinities and ratios, detecting conformational changes for the proteins, separating and identifying bound proteins, and/or the evaluating binding kinetics.[13] Methodologies for these investigations include: UV-vis, fluorescence spectroscopy, dynamic light scattering (DLS), zeta potential (ξ), atomic force microscopy (AFM), circular dichroism (CD), fourier transform infrared spectroscopy (FTIR), X-ray crystallography (XRD), nuclear magnetic resonance (NMR), size exclusion chromatography (SEC), capillary electrophoresis (CE), isothermal titration calorimetry (ITC), quartz crystal microbalance (QCM), mass spectroscopy (MS), analytical ultracentriguation (AUC) and surface plasmon resonance (SPR).[3,7,13] It is very difficult to find a single technique that would be able to accurately detect all the potential information from the protein corona because of the variability of the protein sizes, concentrations, binding affinities, as well as the nature and kinetics of their specific association.[13]

Understanding the strengths and weaknesses of each analysis method and employing more than one is necessary to form a complete understanding of any nanoparticle – bioconjugation.[14] The Colvin group has by and large measured nanoparticle – protein bioconjugation using AUC analysis.[7,15-17] This sensitive analytical technique is particularly useful for detecting associations and quantifying the number of proteins bound for an individual protein sample on a nanoparticle. Figure 1.2 A&B show AUC

evaluations to determine association and the binding stoichiometries for proteins on a nanoparticle surface.[7] Changes in the sedimentation coefficient distributions for nanoparticle samples with and without proteins are used to detect association, and systematically concentration of protein need to saturate the surface.[7] Through these types of evaluation AUC has been shown to be a viable and sensitive analytical method to detect strongly bound proteins on a nanoparticle surface.[17] However, results showing no association can be misleading. High centrifugal forces employed could perturb weakly bound proteins.[18] Therefore, it is useful to couple this method with others that are better suited for analysis of weak associations.

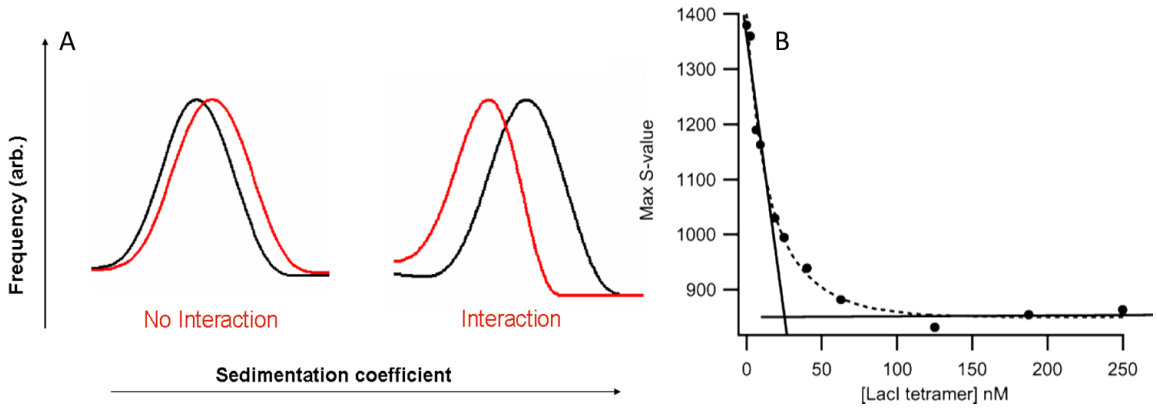

Figure 1.2. Nanoparticle – protein association, AUC.

(A) The AUC, sedimentation coefficient distributions for nanoparticle samples before incubation (black lines) with a protein solution and after (red lines) are used to determine protein association. Shifts in the peak sedimentation coefficient value are used to detect an association; with no association the peaks are unchanged and with an association the peaks are shifted to lower s-values. (B) Evaluation of the sample with varying concentrations of protein can be used to quantify the number of proteins per nanoparticle, figure adapted from ref [7].

Analytical approaches with less perturbation of the sample are necessary for detecting weak or dynamic protein associations.[14] Some successful approaches have been: ITC, UV-vis, SEC, and equilibrium dialysis.[3,4] Figure 3A shows the evaluation of N-isopropylacrylamide/N-tert-butylacrylamide (NIPAM/BAM) copolymer nanoparticles via ITC to detect their interaction with human serum albumin (HSA).[3] Discernible changes were detected using ITC analysis for the copolymer nanoparticles with HSA, however, many other proteins known to associate showed no measurable heat changes during their analysis.[3,4,14] The variations in results were attributed to the differences in types of binding that occurs, only enthalpic associations can be detected by ITC.

Another approach, UV-vis spectroscopy can be used to detect both enthalpic and entropic associations, but only for binding close to the surface for nanoparticles with consistent spectral shifts relative to their local environment.[10,13,19-21] Figure 3B presents the spectral changes for gold nanoparticles from 5 to 80 nm with common human blood proteins.[10] However, since the binding has to alter the core nanoparticle to induce a spectroscopic shift the thickness of a surface coating or protein layer can be an issue.[14,22,23]

By far one of the most versatile methodologies presented in literature is size exclusion chromatography, SEC. Protein association, strength, and kinetic information can be found based on changes in the resonance time for a protein passed through a porous column with and without nanoparticles. Larger materials, such as the nanoparticles, elute quickly from the size-exclusion matrix because they are too big to interact with the pores. In contrast, smaller materials, such as proteins, are able to enter the pores where the time they reside there is dependent on their molecular weight. Figure 3C displays

chromatograms which show that protein associations with the quickly eluting nanoparticles decrease the resonance time, so even weak or brief interactions can be detected.[3,4]

Lastly, borrowing a method used to evaluate protein associations with small molecules; equilibrium dialysis can be used to measure even weak associations when the size difference between nanoparticles and proteins are sufficiently different.[14] Within this thesis, we show that because of the large size difference, protein - nanoparticle associations can be determined for small lysozyme proteins with the much larger gold nanoparticles, based on their retention in a dialyzed sample.

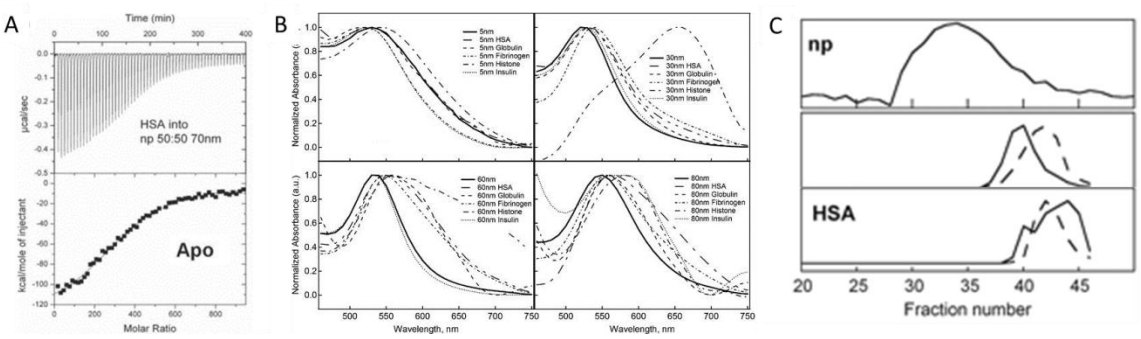

Figure 1.3. Evaluation of weak protein – nanoparticle associations.

(A) ITC for evaluation of HSA binding to copolymer nanoparticles, figure from ref [4]. (B) UV-vis shifts in the peak absorbance position from nanoparticle absorbance alone (solid black lines) and with different protein additions (dashed lines); figure from ref [10]. (C) SEC elution profiles for nanoparticles and proteins without nanoparticles (dashed lines) and with nanoparticles (solid line) for samples nanoparticles alone (top), protein with apparent association (middle) and HSA (bottom); figure from ref [4]

1.3. CONTROLLING NP-PROTEIN ASSOCIATIONS

Due to the variability inherent in analysis methods, it is difficult to deduce true trends in nanoparticle – protein associations; however, in general, particle size, shape and hydrophobicity seem to have the most influence on the protein species that adsorb.[24,25] Therefore, to gain control of the protein corona requires precise design in size, shape and surface coating of the particles. Size and shape of a nanomaterial starts with the synthesis of a uniform core particle. Wet chemical approaches have vastly improved this process in terms of particle consistency. Most importantly for work on bioconjugation is the surface coating material. A well designed surface strategy will promote or prevent protein association.[26] For biological studies nanoparticles should remain hydrophilic and well dispersed in solution; coatings such as: polymers, surfactants, passivating proteins, glycoproteins, and polysaccharides are tethered to a nanoparticle's surface to reduce the total adsorption of proteins.[24,27-29]

By far the most common surface modification material for enhanced control over the composition of the protein corona is the polymer; poly(ethylene glycol) (PEG).[30,31] PEG is a flexible, non-ionic, linear chain polymer composed of two carbons and an oxygen repeating monomers. It is soluble in a number of solutions and ionic strengths, making it highly attractive for use in biological applications. Furthermore, PEG shows little toxicity, is readily cleared from the body, does not elicit an immunogenic response and has been approved by the U.S. food and drug administration (FDA) for use in food, cosmetics and pharmaceuticals.[32,33] PEG coatings are not just used for nanoparticles they have also been applied to proteins, enzymes, hormones, liposomes, and drug products to

improve the pharmacokinetics and pharmacodynamics through increased resonance time in the blood stream (half-life).[29,33,34]

1.4. MECHANISM OF POLY(ETHYLENE GLYCOL)

The mechanism PEG coatings use to increase circulation times is widely believed to be a result of repelling proteins through steric hindrances. For a protein to association with a PEG layer there are many thermodynamic barriers it would have to overcome. Enthalpic barriers include the energy required to break hydrogen bonds formed between each monomer subunit and up to four water molecules.[24,30-32,35] Confinement of a protein pose possible entropic barriers, which include compression of extended PEG chains and causing a loss in the degrees of freedom necessary to allow proteins to associate, especially for large molecular weight PEG molecules.[24,30,31] There would be an entropic gain with protein association based on the displacement of water from the associated polymer. Overall, studies of protein association tendencies on PEG covered surfaces are inconsistent; ranging from no change in the protein resistances, moderate attractions, to complete repulsion.[30] These inconsistencies could, in large part, be due to the analysis methods used, as discussed above for studies involving proteins on nanoparticles.

In general, increasing the coverage of a PEG layer on a nanoparticle surface decreases the amount of proteins that adsorb (figure 4A).[6] A 2% w/w PEG component in PLA copolymer nanoparticles decreased the total plasma protein adsorption by 10% relative to the nanoparticle without PEG. Increasing the PEG concentration to 5% w/w, for the same PLA nanoparticles, suppressed 70% of the total plasma protein adsorption, showing

that even small changes in the surface composition of the PEG layer decrease the surface affinity of proteins.[24,36] With a complete layer formed from a high polymer surface coverage, theoretically the plasma protein adsorption could effectively be suppressed.[3,24,37]

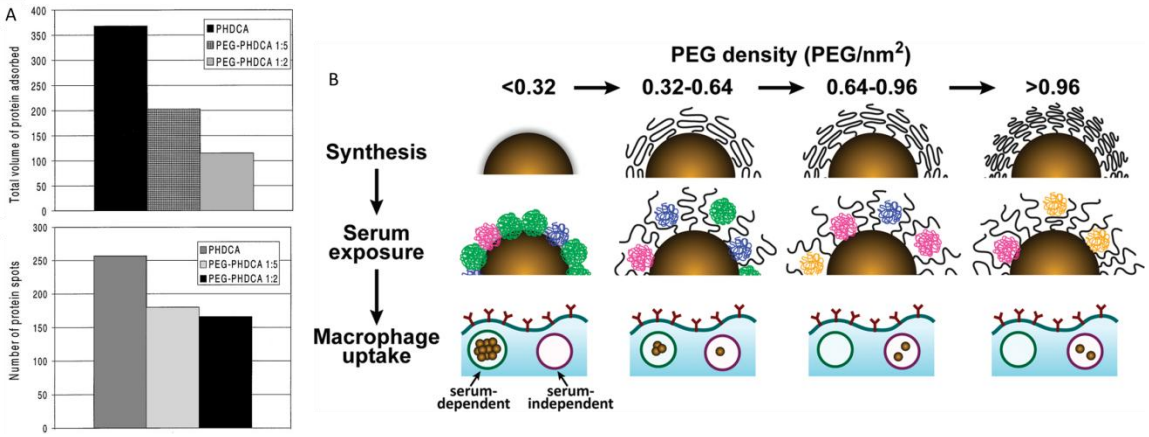

Figure 1.4. PEG coverage deceases protein association.

(A) Increased PEG concentration decreased the amount of protein that adsorbed and the sites available for protein adsorption, figure from ref [6]. (B) Illustration of increased PEG coating with resulting serum protein association and macrophage uptake, figure from ref [9].

Adequate PEG coverage needed for protein repulsion is dependent on the polymer grafting density and molecular weight for a given nanoparticle radius of curvature.[38] Figure 5 shows that PEG molecules tethered to any surface are able to assume either a mushroom or brush conformation, based on the amount of extension. When the distance between polymers is sufficiently greater than the Flory radius (R_f) of the polymer, there are more intramolecular associations and the molecule takes on a "mushroom"

conformation.[32] However, increasing the number of polymers in a given surface area eventually leads to decreased distances between molecules and more intermolecular associations. When the extension of the polymer is greater than the distance between molecules the conformation is a "brush".[39,40] For nanoparticles the PEG packing and conformation is influenced by the radius of curvature. The distance between polymer molecules necessary to call the conformation a brush, for a flat surface is $d < R_f$, while on a curved surface any $d < 2R_f$ is in a brush conformation.[2,11,32] Once a PEG layer has obtained a brush conformation the surface tends to be inert, showing little to no attractive forces, or protein association.[36,41] Therefore, controlling the conformation of the PEG layer is a specific strategy that can be used to design surfaces for preventing or promoting protein associations.

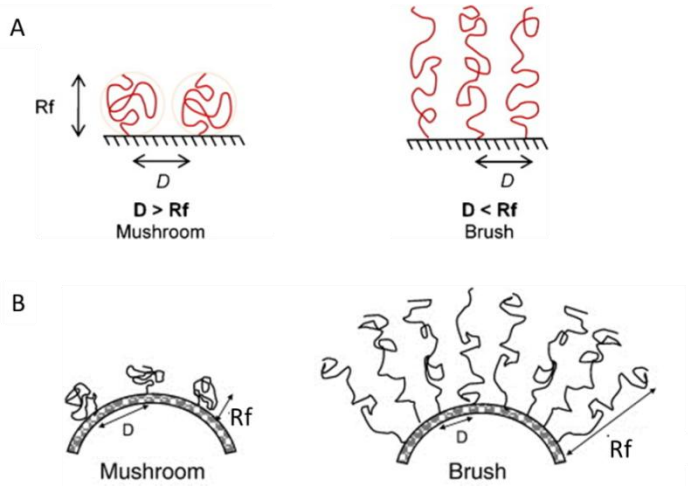

Figure 1.5. PEG conformation on a surface.

(A) Conformation of PEG on a flat surface is a brush when the distance between polymers is less than the Flory radius (R_f), figure from ref [2] For curved surfaces the conformation changes from mushroom to brush when the distance between polymers is less than twice the Flory radius (R_f) of PEG on a curved surface from ref [11].

1.5. ADVANTAGEOUS PROTEIN – NANOPARTICLE ASSOCIATIONS

Protein – nanoparticle interactions can be advantageous for applications such as targeting, enhancing enzyme activity, nucleating protein crystals and forming nanoparticle assemblies.[42-44] Thus far, we have discussed research aimed at understanding protein associations in order to eliminate them; however promoting controlled associations with advantageous proteins is used for biomolecular delivery of nanoparticles to site specific areas of the body.[43] Targeting proteins such as albumin, antibody, transferrin, cytokine and low-density lipoprotein can be tethered to the nanoparticle surface are used as active targets.[26] However, promoting strong associations between highly curved nanoparticle surfaces and protein molecules will often affect the protein's secondary structure and its function.[24,45]

Protein – nanoparticle associations impact the nanoparticle by directing its biological behavior and the nanoparticle in turn impacts the function and fate of the protein through conformational changes.[26] Adsorptions of proteins on nanoparticles have been shown to cause the protein to either denature or obtain a more stable structure. Ultimately, loss of conformation can result in the destruction of protein's function and formation of fibrils. Conversely, more stable structures can show enhanced activity and formation of crystals.[12,24,26,42,44-50]

The nanoparticle diameter, shape and surface hardness influence the resulting structural changes for a bound protein. Figure 1.6 shows that the protein associated with the small

nanoparticle was more likely to retain its native structure, while the large nanoparticle causes the protein to denature.[5,26] Since denaturation is the first step in the formation of protein fibers, it isn't surprising that nanoparticles have been found to induce fibrillation for β2m proteins.[12] Accumulation on the nanoparticle surface creates a closer proximity between the now denatured proteins which in turn promote rapid between exposed hydrophobic residues. These protein–protein interactions result in the formation of long fibers, seen in figure 1.6C. However, when the secondary structure of the protein is retained, the close proximity and locally high concentration can promote protein-protein associations that can induce protein crystal formation. Polystyrene and gold nanoparticles have been shown to have properties that nucleate protein crystallization, perhaps due to retention of the native protein structure upon binding.[49,50]

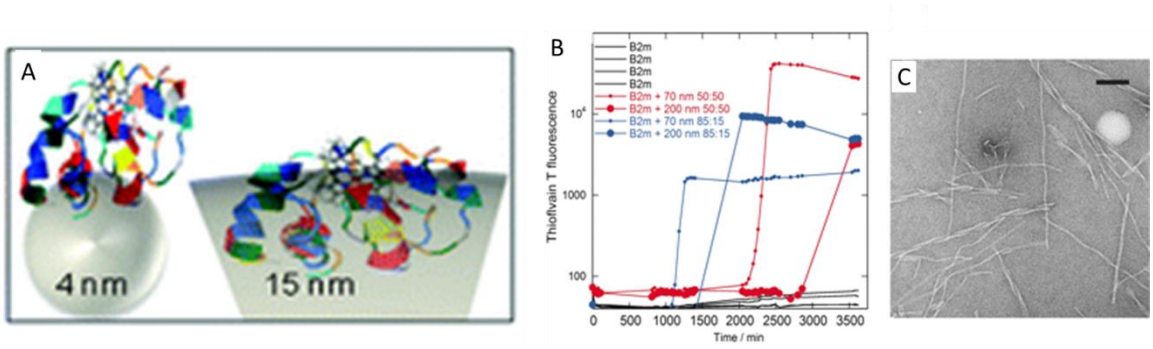

Figure 1.6. Nanoparticle – protein association affect protein conformation.

(A) Protein structure on a curved nanoparticle surface can be protected against loss of secondary structure, even in harsh environments or they may denature, figure from ref [5]. (B) Kinetics of β2m fibrillation in the presence of nanoparticles, show nanoparticle nucleate the formation of fibrils. (C) Negative stained TEM image of the fiber formed with 70 nm nanoparticles, figure from ref [12].

Controlled associations between nanomaterials and biomolecules, such as proteins, nucleic acids, and other macromolecules have been used to create inorganic and organic nanostructured and mesoscopic hybrid architectures for possible uses in biological research, electronics and sensing applications.[44,51] Most commonly, organizations of nanomaterial into adaptable two dimensional arrangements with long range control have been formed on films made from molecular arrays of crystalline bacterial surface layer (S-layer) proteins.[52,53] Studies of the properties nanomaterials exhibit in complex two dimensional arrangements have revealed many interesting cooperative effects for metallic, semiconductor and magnetic nanoparticles, however more complex three dimensional assemblies could have even more profound ensemble interactions.[44,52,54]

One approach to generating complex nanostructure mesoscopic assemblies utilizing the natural ability of DNA to self-assemble, based on the union of base pairs. DNA subunits are functionalized to create oligonucleotide modified nanoparticles which are driven to assemble into complex two dimensional and three dimensional structures.[1,44,55] Figure 1.7 shows a three dimensional arrangement of nanospheres coordinated through DNA segments as an example of the types of materials that have been produced by Chad Mirkin's research group at North Western University.[1,55] DNA crystallizes nanomaterial into structures with exquisite control, showing the capabilities that can be possible when using biological templating.[56,57] However, the functionalized oligonucleotides required for tailoring the design of these three dimensional assemblies are not produced in nature; and they require time and expense to create.

Strategies that use naturally occurring biomolecules for directed assembly would decrease the cost and increase the feasibility of creating large amounts of the nanostructured architectures.[55] Native proteins can be driven to self-assemble into three dimensional structures by providing an environment weak associations are favored. Protein crystals structures are large, porous and regularly spaced and in can be perturbed to crystallize into different shapes and symmetries. three different roles; hollow proteins with internalized nanomaterial, porous protein crystals structures as scaffolds infused with metals and composite crystals through directed nanoparticle – protein associated conjugates.[8,58,59] Understanding and controlling the surface properties of nanoparticles will lead to applications beyond the biological realm. The potential for material science engineering through nanoparticle biomolecule manipulation is exciting.

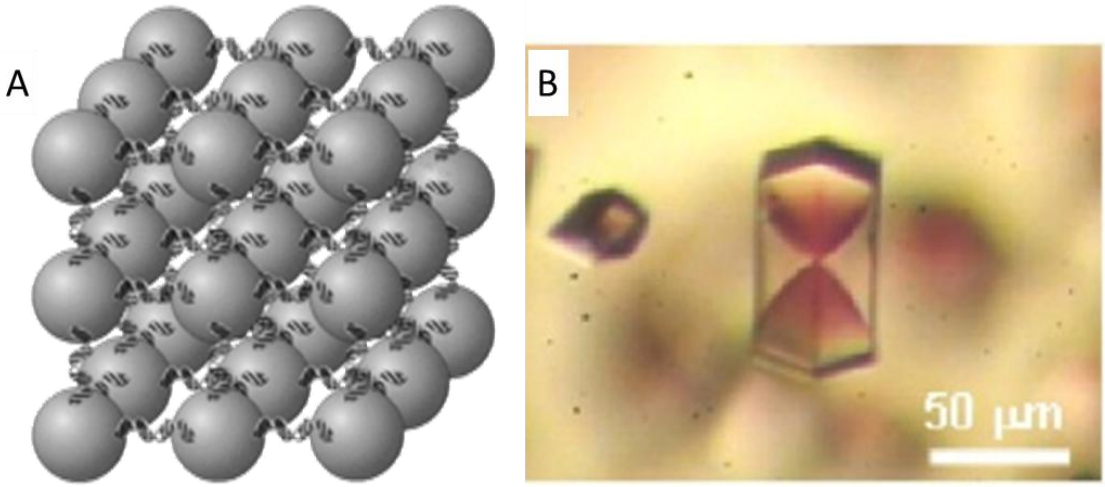

Figure 1.7. Three dimensional assemblies of nanoparticles.

(A) Nanoparticle assemblies from controlled association with (A) DNA, figure from ref [1] and (B) lysozyme , figure from ref [8].

1.6. REFERENCES

(1) Mirkin, C. A. *Inorganic Chemistry* **2000**, *39*, 2258.

(2) Wang, M.; Thanou, M. *Pharmacological Research* **2010**, *62*, 90.

(3) Lynch, I.; Dawson, K. A. *Nano Today* **2008**, *3*, 40.

(4) Cedervall, T.; Lynch, I.; Lindman, S.; BerggÃ¥rd, T.; Thulin, E.; Nilsson, H.; Dawson, K. A.; Linse, S. *Proceedings of the National Academy of Sciences* **2007**, *104*, 2050.

(5) Shrivastava, S.; Nuffer, J. H.; Siegel, R. W.; Dordick, J. S. *Nano Letters* **2012**, *12*, 1583.

(6) Peracchia, M. T.; Harnisch, S.; Pinto-Alphandary, H.; Gulik, A.; Dedieu, J. C.; Desmaële, D.; d'Angelo, J.; Müller, R. H.; Couvreur, P. *Biomaterials* **1999**, *20*, 1269.

(7) Calabretta, M.; Jamison, J. A.; Falkner, J. C.; Liu, Y.; Yuhas, B. D.; Matthews, K. S.; Colvin, V. L. *Nano Lett.* **2005**, *5*, 963.

(8) Takeda, Y.; Kondow, T.; Mafuné, F. *Chemical Physics Letters* **2011**, *504*, 175.

(9) Walkey, C. D.; Olsen, J. B.; Guo, H.; Emili, A.; Chan, W. C. W. *Journal of the American Chemical Society*, *134*, 2139.

(10) Lacerda, S. H. D. P.; Park, J. J.; Meuse, C.; Pristinski, D.; Becker, M. L.; Karim, A.; Douglas, J. F. *ACS Nano* **2009**, *4*, 365.

(11) Dufort, S.; Sancey, L.; Coll, J.-L. *Advanced Drug Delivery Reviews* **2012**, *64*, 179.

(12) Linse, S.; Cabaleiro-Lago, C.; Xue, W.-F.; Lynch, I.; Lindman, S.; Thulin, E.; Radford, S. E.; Dawson, K. A. *Proceedings of the National Academy of Sciences* **2007**, *104*, 8691.

(13) Li, L.; Mu, Q.; Zhang, B.; Yan, B. *Analyst* **2010**, *135*, 1519.

(14) Aggarwal, P.; Hall, J. B.; McLeland, C. B.; Dobrovolskaia, M. A.; McNeil, S. E. *Advanced Drug Delivery Reviews* **2009**, *61*, 428.

(15) Jamison, J. A.; Krueger, K. M.; Yavuz, C. T.; Mayo, J. T.; LeCrone, D.; Redden, J. J.; Colvin, V. L. *ACS Nano* **2008**, *2*, 311.

(16) Calabretta, M. K.; Matthews, K. S.; Colvin, V. L. *Bioconjugate Chemistry* **2006**, *17*, 1156.

(17) Jamison, J. A.; Krueger, K. M.; Mayo, J. T.; Yavuz, C. T.; Redden, J. J.; Colvin, V. L. *Nanotechnology* **2009**, *20*, 355702.

(18) Cedervall, T.; Lynch, I.; Lindman, S.; Berggård, T.; Thulin, E.; Nilsson, H.; Dawson, K. A.; Linse, S. *Proceedings of the National Academy of Sciences* **2007**, *104*, 2050.

(19) Dobrovolskaia, M. A.; Patri, A. K.; Zheng, J.; Clogston, J. D.; Ayub, N.; Aggarwal, P.; Neun, B. W.; Hall, J. B.; McNeil, S. E. *Nanomedicine: Nanotechnology, Biology and Medicine* **2009**, *5*, 106.

(20) Zhang, F.; Skoda, M. W. A.; Jacobs, R. M. J.; Zorn, S.; Martin, R. A.; Martin, C. M.; Clark, G. F.; Goerigk, G.; Schreiber, F. *The Journal of Physical Chemistry A* **2007**, *111*, 12229.

(21) Delfino, I.; Cannistraro, S. *Biophysical Chemistry* **2009**, *139*, 1.

(22) Tessier, P. M.; Jinkoji, J.; Cheng, Y.-C.; Prentice, J. L.; Lenhoff, A. M. *Journal of the American Chemical Society* **2008**, *130*, 3106.

(23) Edri, E.; Regev, O. *Analytical Chemistry* **2008**, *80*, 4049.

(24) Walkey, C. D.; Chan, W. C. W. *Chemical Society Reviews* **2012**, *41*, 2780.

(25) Lundqvist, M.; Stigler, J.; Elia, G.; Lynch, I.; Cedervall, T.; Dawson, K. A. *Proceedings of the National Academy of Sciences* **2008**, *105*, 14265.

(26) M.D. Marco, S. S., K.A. Razak *International Journal of Nanomedicine* **2010**, *5*, 37.

(27) McNeil, S. E. *J. Leukoc. Biol.* **2005**, *78*, 585.

(28) Koo, Y.-E. L.; Reddy, G. R.; Bhojani, M.; Schneider, R.; Philbert, M. A.; Rehemtulla, A.; Ross, B. D.; Kopelman, R. *Advanced Drug Delivery Reviews* **2006**, *58*, 1556.

(29) Moghimi, S. M.; Szebeni, J. *Progress in Lipid Research* **2003**, *42*, 463.

(30) Kingshott, P.; Griesser, H. J. *Current Opinion in Solid State and Materials Science* **1999**, *4*, 403.

(31) Hoffman, A. S. *Journal of Biomaterials Science, Polymer Edition* **1999**, *10*, 1011.

(32) Allen, C.; Santos, N. D.; Gallagher, R. C.; Chiu, G. N. C.; Shu, Y.; Li, W. M.; Johnstone, S. A.; Janoff, A. S.; Mayer, L. D.; Webb, M. S.; Bally, M. B. *Bioscience Reports* **2002**, *22*, 225.

(33) Harris, J. M.; Chess, R. B. *Nature Reviews Drug Discovery* **2003**, *2*, 214.

(34) Mehvar, R. *J Parm Pharmaceut Sci* **2000**, *3*, 125.

(35) Lee, J. H.; Lee, H. B.; Andrade, J. D. *Progress in Polymer Science* **1995**, *20*, 1043.

(36) Gref, R.; Luck, M.; Quellec, P.; Marchand, M.; Dellacherie, E.; Harnisch, S.; Blunk, T.; Muller, R. H. *Colloids and Surfaces B: Biointerfaces* **2000**, *18*, 301.

(37) Unsworth, L. D.; Sheardown, H.; Brash, J. L. *Langmuir* **2008**, *24*, 1924.

(38) Jeon, S. I.; Lee, J. H.; Andrade, J. D.; De Gennes, P. G. *Journal of Colloid and Interface Science* **1991**, *142*, 149.

(39) Gennes, P. G. d. *Macromolecules* **1980**, *13*, 1069.

(40) Kruger, K. M.; Al-Somali, A. M.; Mejia, M.; Colvin, V. L. *Nanotechnology* **2007**, *18*, 475709 (7pp).

(41) Heuberger, M.; Drobek, T.; Spencer, N. D. *Biophysical Journal* **2005**, *88*, 495.

(42) Wu, Z.; Zhang, B.; Yan, B. *International Journal of Molecular Sciences* **2009**, *10*, 4198.

(43) You, C.-C.; De, M.; Rotello, V. M. *Current Opinion in Chemical Biology* **2005**, *9*, 639.

(44) Niemeyer, C. M. *Angewandte Chemie International Edition* **2001**, *40*, 4128.

(45) Mandal, H. S.; Kraatz, H.-B. *Journal of the American Chemical Society* **2007**, *129*, 6356.

(46) Aubin-Tam, M.-E.; Hamad-Schifferli, K. *Langmuir* **2005**, *21*, 12080.

(47) Gagner, J. E.; Lopez, M. D.; Dordick, J. S.; Siegel, R. W. *Biomaterials, 32*, 7241.

(48) Hong, R.; Fischer, N. O.; Verma, A.; Goodman, C. M.; Emrick, T.; Rotello, V. M. *Journal of the American Chemical Society* **2004**, *126*, 739.

(49) Hodzhaoglu, F.; Kurniawan, F.; Mirsky, V.; Nanev, C. *Crystal Research and Technology* **2008**, *43*, 588.

(50) Kallio, J. M.; Hakulinen, N.; Kallio, J. P.; Niemi, M. H.; Kärkkäinen, S.; Rouvinen, J. *PLoS ONE* **2009**, *4*, e4198.

(51) Katz, E.; Willner, I. *Angewandte Chemie International Edition* **2004**, *43*, 6042.

(52) Mark, S. S.; Bergkvist, M.; Yang, X.; Teixeira, L. M.; Bhatnagar, P.; Angert, E. R.; Batt, C. A. *Langmuir* **2006**, *22*, 3763.

(53) Sára, M.; Sleytr, U. B. *Journal of Bacteriology* **2000**, *182*, 859.

(54) Astier, Y.; Bayley, H.; Howorka, S. *Current Opinion in Chemical Biology* **2005**, *9*, 576.

(55) Macfarlane, R. J.; Lee, B.; Jones, M. R.; Harris, N.; Schatz, G. C.; Mirkin, C. A. *Science* **2011**, *334*, 204.

(56) Park, S. Y.; Lytton-Jean, A. K. R.; Lee, B.; Weigand, S.; Schatz, G. C.; Mirkin, C. A. *Nature* **2008**, *451*, 553.

(57) Jones, M. R.; Macfarlane, R. J.; Lee, B.; Zhang, J.; Young, K. L.; Senesi, A. J.; Mirkin, C. A. *Nat Mater* **2010**, *9*, 913.

(58) Falkner, J. C.; Turner, M. E.; Bosworth, J. K.; Trentler, T. J.; Johnson, J. E.; Lin, T.; Colvin, V. L. *Journal of the American Chemical Society* **2005**, *127*, 5274.

(59) Kasyutich, O.; Sarua, A.; Schwarzacher, W. *Journal of Physics D: Applied Physics* **2008**, *41*, 134022.

Chapter 2

MATERIALS AND METHODS

This Chapter describes the synthesis and characterization methods used throughout this thesis. First, the detailed procedures for producing nanoscale spheres, rods and bipyramids of gold are presented; additionally, nanoscale iron oxide and cadmium selenide materials were produced. Characterization of these materials relied on a variety of tools including microscopies, vibrational spectroscopies, elemental analysis and x-ray diffraction. Finally, approaches to the analysis of the biological-nanoparticle interface are presented along with the methods employed for protein crystallization.

2.1. NANOPARTICLE SYNTHESIS / PEGYLATION / SAMPLE PREPARATION

2.1.1. Gold nanoparticles

Gold nanoparticles of 5, 10, 15 and 20 nm diameter were purchased from Ted Pella (0.01% gold chloride, <10% coefficient of variation for mean diameter). Additionally,

~10 to 15 nm diameter gold nanoparticles were also synthesized in the lab using Frens' method.[1] Briefly, a 1 mM $HAuCl_4 \cdot 3H_2O$ (Sigma Aldrich, 99.9+%) solution was heated until boiling. Then, a preheated 10% w/w sodium citrate (Fluka, >99.0% pure) solution was added (1mL for every 10 mL gold solution). Following the addition of the citrate the reaction mixture was allowed to boil for 15 minutes. During this time, the citrate reduces the gold ions in solution which leads to the formation of gold nanoparticles; Figure 2.1A outlines this process. As the particles nucleated and formed, the solution progressed through a range of colors from yellow to colorless then gray, purple and finally dark red, shown in the series of images in Figure 2.1B. After the 15 minutes of heating, the solution was cooled rapidly by running water over the outside of the flask. Highly crystalline, gold nanoparticles between 10 – 15nm are the result (Figure 2.1C). The particle size can be tuned by varying the ratio of gold ions to citrate molecules. [2,3]

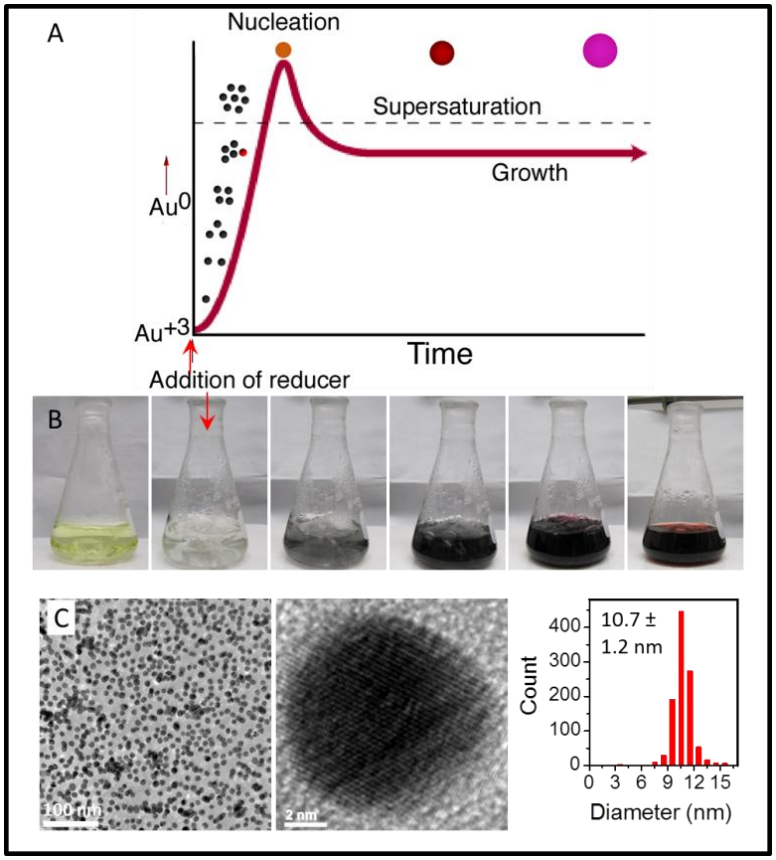

Figure 1.8. Gold nanoparticle synthesis.

(A) Gold nanoparticles are synthesized from a solution of Au+3 ions. (B) As particles form and develop the solution progresses through a series of colors depending on the size of the nanoparticles in solution. (C) TEM images show the typical sizes of the nanoparticle produced for this synthesis are between 10 – 15 nm, and are highly crystalline.[2,3]

2.1.2. PEGylation of gold nanoparticles

Thiol functionalized poly(ethylene)glycol (Creative BioChem, 95 ± 3%) of either 1K, 2K, 5K, 10K, 20K or 30K molecular weight was used to functionalize the gold

nanoparticles. Excess PEG-thiol (~3000 PEG/particle) was added to the gold nanoparticles in solution, and the resulting solution was stirred for at least 12 hours, to allow time for the polymer layer to form. After this treatment, it was necessary to purify the samples to remove unreacted PEG-thiol. Sample purification required both three spin filtration treatments, followed by an additional three rounds of centrifugation. First, the solution was exposed to a maximum filter cutoff of 100 molecular weight, which retained all of the nanoparticles but allowed the unbound PEG-thiol to pass through. Samples placed in the spin filter vials (Millipore) were centrifuged three times at 4150 RPM for 15 minutes (or until most of the solution was removed from the sample). The remaining ~150 μL pelleted sample was resuspended in Milli pore ultrapure water. Additionally, samples were further cleaned three times via sedimentation either on the benchtop Sorel Centrifuge (particle diameters > 10nm) or the Beckman Ultracentrifuge. The typical RPM employed (30,000 RPM (5 nm), 20,000 RPM (10 nm), 11,000 RPM (15, 20nm)) sedimented the nanoparticles into a pellet, and left a colorless supernatant containing any excess PEG-thiol and less dense impurities. The nanoparticles were then resuspended in Milli pore ultrapure water and the procedure was repeated. Following purification of the sample, the solution concentration was adjusted so as to ensure a constant optical density at the (λ = ~520 nm) peak absorbance position. Absorbance peaks for 10 nm gold nanoparticles were diluted to obtained an optical density of 1.0 ± 0.2 absorbance units (~9.5 nM), at 520 nm unless otherwise stated.[4]

2.1.3. Synthesis, PEGylation and purification of shaped gold nanoparticles (rods and bipyramids)

*All gold nanorod and bypriamid synthesises, PEGylations and purifications were carried out by Courtney Payne, in the Hafner Lab. I provided the PEG and helped amend the PEGylation and purification procedures.

Gold nanorods were synthesized in a seed-mediated synthesis as described by Sau and Murphy.[5] Gold bipyramids were synthesized as previously reported in a two-step synthesis; formation of a seed solution and a bipyramid growth solution.[6] PEGylation of gold nanorods and gold bipyramids was performed using the 20,000 MWt PEG-thiol. The PEGylation procedure was followed as reported previously.[7]

2.1.4. Quantum dots

*All quantum dot and iron oxide nanoparticle syntheses, PEGylations and purifications were carried out by Huiguang Zhu in the Colvin Lab.

The CdSe, which form the quantum dot cores, was formed in a now common synthetic procedure under ultra-pure N_2 flow.[8] The method for CdSe/CdZnS QDs synthesis was adapted from our previous work.[8] The reaction was run under ultra-pure N_2 flow. The purified CdSe core quantum dot solution suspended in chloroform was transferred into a three-neck flask and the solvent was pumped off by vacuum. ODA (Aldrich, Octadecylamine, 97%) and ODE are then added into the flask and heated to 150°C. 0.04 M zinc (Aldrich, Zn(OAc)2, 99.99%) solution was formed in 0.5 g TOPO, 2.0 mL TOP, and 8.0 mL of ODE heated to 200 °C. Similarly a 0.04 M cadmium solution was prepared. Zinc/cadmium were add in a molar ratio of 1:4, to form precursors and thiourea/ethanol solutions were injected into the flask via syringe, alternatively, and the

mixture was stirred for another 60min. The reaction was cooled to ~60°C and then the particles were precipitated using acetone and rinsed with ethanol. The core/shell quantum dot pellets can be redispersed into a variety of solvents including hexane, chloroform, and toluene.

Iron oxide nanocrystals were synthesized based on the method reported previously.[9] The nanocrystals were purified using methanol, acetone and hexane. First, 5ml of the as-prepared nanoparticles were washed using 25 mL of methanol and 25 mL of acetone to remove unreacted iron carboxylate, surfactant, and 1-octadecene. The purification process was repeated 3 times. The cleaned nanoparticles were then re-dispersed in 15 ml of hexane and separated from unreacted salt and other impurities by centrifugation at 4500 rpm for 30 min. The purified black iron oxide nanocrystals were easily dispersed in chloroform, THF, toluene or any other nonpolar solvent.

An amphiphilic copolymer poly(maleic anhydride-alt-1-octadecene) (PMAO) (Mn = 30K -50K)-PEG (Mn = 1K, 2K, 5K, 10K, 20K) (molar ratio PMAO:PEG=1:10) was formed on the surface of iron oxide and quantum dot particles through an anhydride coupling reaction by mixing PMAO and PEG in chloroform overnight.[10] This polymer was mixed with purified nanoparticles in chloroform, vacuum dried and re-dispersed in ethyl ether. A pH 10 borate buffer was added and the mixture was probe sonicated for 30s. The ether was evaporated off and a clear solution was formed. The polymer-capped nanoparticles were then centrifuged at 35,000 RPM for 4 hours, three times, to remove any excess polymer. The purified water-solubilized NPs were stored in 50 mM borate buffer (pH 10) in the dark.[11]

2.2. NANOPARTICLE CHARACTERIZATION

2.2.1. Transmission electron microscopy (TEM):

2.2.1.1. Sample preparation:

Preparing nanoparticles for successful TEM imaging requires control of sample concentration, drying time and the appropriate grid material. Samples need to contain enough particles to give some color to the solution, but not so many that it is deeply colored. With such solutions, 10 to 20 μL of sample are placed onto a copper grid, using a micropipette, and allowed to evaporate slowly. Drying time can be controlled by placing the grid on an appropriate substrate such as a piece of glass (slow) or a kimwipe (fast). For aqueous samples the grid should be placed on a hydrophobic surface so the sample will not spread and the droplet can dry uniformly over a long period of time. Conversely, organic solvents should be wicked away quickly so the grids would be placed on filter paper or another absorbent material.

TEM sample support grids are chosen based on the approximate size of the nanomaterials, the magnification anticipated for imaging and the applications (i.e. Gatan image filtering (GIF), electron diffraction, analytical scanning imaging device (ASID), scanning transmission electron microscopy (STEM)) you will be running.

Size, size distribution and shape information for nanoparticle sample are commonly determined from TEM images. Some key things to remember while taking images that will be processed on the sizing software are: higher contrast is better than higher

magnification; large clumps of materials are not suitable as edges of nanoparticles cannot be detected; and any particles on the edges of the image will not be counted so try to get as many particles in the middle of an image as possible. Large particles should be imaged at the lowest magnification where individual particles can still be resolved (10K - 80KX). Because magnification affects both the contrast and resolution, inversely to each other, a high magnification increases the resolution while decreasing the contrast. It is much easier for sizing software to detect the edges of particles when they are at a maximum contrast; therefore, the ideal magnifications for sizing are between 10K and 80K, for gold nanoparticles between 5 and 20 nm 20K magnifications are best, Figure 2.2A shows a typical microgram of 10 nm gold nanoparticles at 20K that would be suitable for size analysis. For these magnifications the grids can have large mesh and thicker formvar coating, such as a 300 mesh copper grid with a formvar type A or B support.

One problem with the 300 mesh grids is that they have large openings between copper mesh which will contribute to sample drift and vibration at higher magnifications. Therefore, when imaging at higher magnification a higher count mesh (400 mesh) should be used. Sizing for small particles (<5nm) can be affect by the thickness of the grid coating, especially those made of low contrast materials like iron oxide or semiconductor materials. For these samples a holey carbon support on 400 mesh grid, should be used. The holey carbon support provides areas where there is no substrate, just particles, which makes it easier to obtain high contrast images at higher magnifications. However,

because the support materials are thick and have an unusual shape they interfere with the image and should not be used at low magnifications (<30KX).

The ideal grid for working at low or high magnification and when attempting ASID, GIF, or energy dispersive spectroscopy (EDS) methods is the ultrathin carbon type A, 400 mesh copper grids. For these grids the mesh is small which minimizes drift and vibration and the carbon support is uniform and thin which allows for the best resolution – a vital optimization for these applications.

2.2.1.2. Instruments:

At Rice there are currently four shared equipment authority (SEA) TEMs:

- a JEOL 1230 high contrast TEM (HC-TEM) run at 120 kV,
- two JEM 2010 TEMs run at 100kV (CryoTEM, TEM)
- a JEM 2100F with a field-emission gun and operated at 200kV (JEM2100F TEM).

The HC TEM is the first TEM that most users are trained on and it is fine for normal imaging operations. It does low magnification, high contrast imaging so it is the best option for large particles or any sample that has been thinly sliced, like biological samples in resin. The HC-TEM has some advanced capabilities such as a double tilt sample holder which is used to run tomography. The CryoTEM can be used to image vitreous ice samples. For routine use the two JEM2010 instruments are identical. They both have 5 position holders allowing for imaging of multiple samples without having to pump down the sample chamber (which is time consuming) and they work well at the

magnification range suitable for sizing and characterizing nanoparticles. The JEM 2100F TEM has a lot of additional capabilities. The field emission gun is a more coherent source of electrons, which allows this instrument to be run at up to 1.5 million magnification. This is necessary in order to image the lattice spacing of crystalline samples (Figure 2.2C). Furthermore, it can be used in scanning mode (analytical scanning imaging device, ASID) which allows the TEM to be used as a scanning transmission electron microscope (STEM). Figure 2.2 E is an ASID image of iron oxide nanoparticles with uranium adsorbed to their surface. The ASID is also equipped with a detector which identifies the energy of X-rays backscattered from the sample for composition based analysis called energy dispersive spectroscopy (EDS). With such information, it is possible to determine the elemental composition of the materials and even map there locations on a sample. Figure 2.2D is an EDS spectrum for sample shown in Figure 2.2E, where peaks can be seen for iron, uranium and copper (contribution from the grid). Additionally, there is a gatan image filtering (GIF) camera that is capable of taking electron energy loss spectrums (EELS) which, like energy dispersive spectroscopy (EDS), determines the composition of the sample, and it can filter an image to show the distribution of the different elements in the viewing area, see Figure 2.2D for GIF image and 2.2F for EELS spectrum.

2.2.1.3. Image processing:

Processing the images on Imagepro software is done to determine the shape, size and size distribution information for the inorganic core nanoparticle. Embedded software programs, termed macros, have been set up in this software to aid in this process. For

reporting the dimensional data, is it important to count many particles. Typically at least 1000 particles are needed to obtain both the diameter and the standard deviation of the diameter for nanoparticle samples; if samples are odd-shapes even more particles will need to be analyzed.

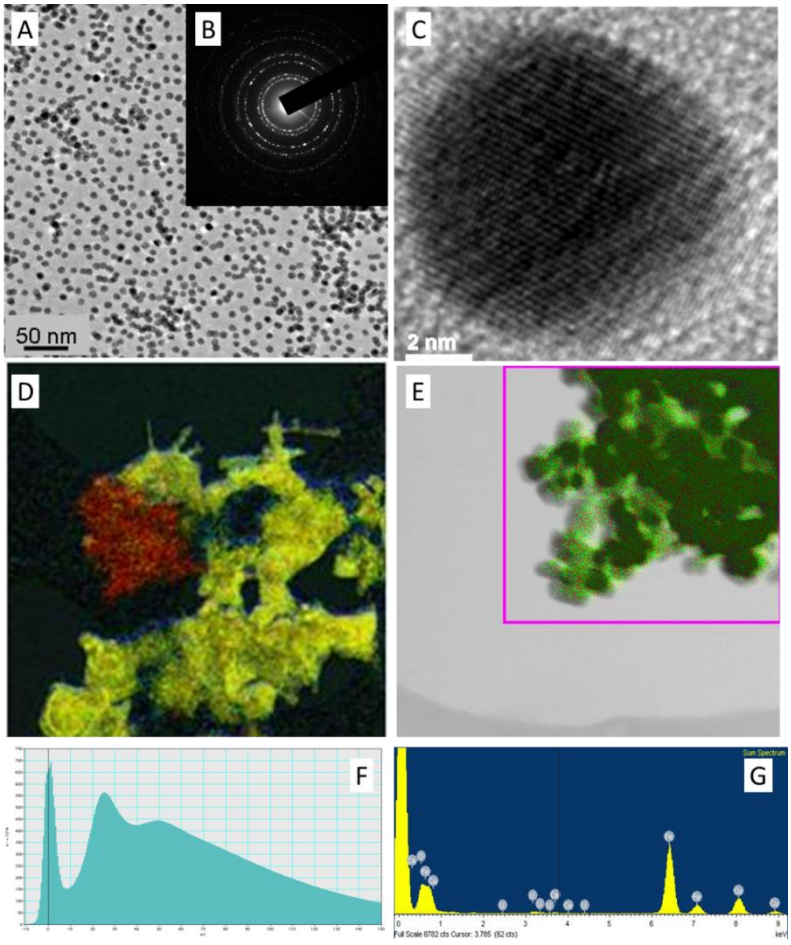

Figure 1.9. TEM Analysis.

TEM micrographs of gold nanoparticles (A) at sizing magnification (40KX) with (B) electron diffraction pattern, and (C) at high magnification (800KX) where lattice planes can be visualized. (D) GIF image filter of zinc and TiO_2 nanoparticles extracted from sunscreen. (E) EDS map on an ASID image of uranium adsorbed to iron oxide nanoparticles. (F) EELS spectrum from gold nanoparticles. (G) EDS spectrum from the sample in (E).

2.2.2. Dynamic light scattering (DLS):

A Malvern Zen6300 Zetasizer NanoS equipped with a 633 nm laser was used to determine the hydrodynamic diameter of particles. The Brownian motion of materials in solution creates a specific autocorrelation in light scattering data; this autocorrelation function is what is used to back out the diameter of nanoparticles. It is a method best suited for samples with diameters between 20 and 1000 nm that are non-aggregated in solution. Using DLS, the sample can be evaluated within its native solution and the measured diameter includes both the dimensions of core material as well as any associated surface ligands. Typical data collections are taken three times, and the user must input the refractive index and absorbance (at 633nm) for the materials. For gold nanoparticles these values are 1.35 and 0.1, respectively. The zetasizer software will automatically optimize the measurement for the number and length of each scan. The number of scans the software chooses can be a good indication of the quality of the sample, typical runs requires 10 – 18 scans and inappropriate samples – those with a very high or low level of scattering - require much more.

The major factors which dictate the success or failure of a DLS measurement are: sample contaminants, sample concentration, ionic strength, and induced motion. Contaminants such as dust, aggregates, or unremoved coating materials affect DLS measurements; these can be addressed through a simple purification including a syringe filtration right before measurement. The material concentration should not, in principle, affect the

reported measurement, but when samples are too concentrated or too dilute then it is not practical to get quality scattering data. As it is hard to know *a priori* what the best concentration might be for a sample. The best approach to determine an optimum concentration is to run the sample at several concentrations and monitor the reported size and polydispersity index and count rate; once the samples are within an appropriate concentration range the size and polydispersity index should no longer change, but the count rate will (at concentrations too high or too low the count rate may not change with concentration because the detector is saturated or the signal is too weak to detect).

The last issue for DLS is the minimization of any induced movement in the sample itself. Thermal variations, particle sedimentation, or mixing will all introduce substantial errors into the scattering analysis and the results will not be usable. It is vital to first equilibrate the sample to the temperature of the instrument; additionally, do not overfill curvettes higher than 10 mm (1mL in the 1 cm X 1cm cuvette). Finally, if samples are dissolving, aggregating or sedimenting then the data will not be reproducible. The count rate signal is the best indication that a sample is changing, if the signal is anything besides a semi-straight line that looks like noise there is fluctuation within the sample.

There are three outputs from the DLS which can be used to extract the hydrodynamic diameter: signal intensity, volume corrected and number corrected scattering autocorrelation curves. Intensity measurements are directly calculated from the Stokes-Einstein equation and are not influenced by the corrections for viscosity, refractive index or absorbance. So this data is less sensitive to user parameters that may be estimated for nanoparticles (e.g. refractive index). However, larger materials scatter light far more

effectively than smaller materials and so a reliance on intensity data can skew the size distributions. The DLS software also provides volume and number correction factors that attempt to correct for this effect. Number corrected data tends to overestimate the population of the smallest materials and usually shows no report of other size populations present in the sample. Volume corrected data generally provide an accurate representation of all the size species present in a sample. The diameter data throughout this thesis was thus derived from the most abundant peak in the volume corrected data; this data was found to be the best match to predicted hydrodynamic diameters derived from the TEM of nanoparticle cores and estimates of the molecular dimensions of surface coating materials.

Figure 2.3 shows two typical applications for DLS data: determining core particle diameter (d), as compared to the values determined from TEM and determining hydrodynamic diameter (H_D) which is d plus the organic coating.

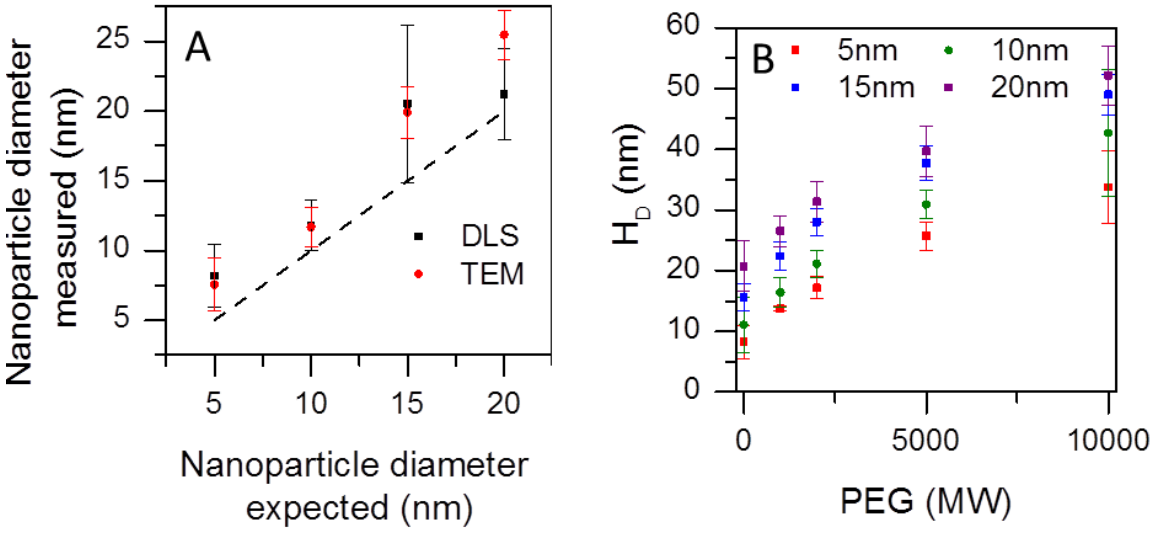

Figure 1.10. DLS Analysis.

Core nanoparticle diameters and distribution (A) for 5, 10, 15 and 20 nm gold nanoparticles show similar values from TEM and DLS. The black dashed line is 1:1 as a guide to the eye. (B) DLS data for the evaluation based on the change in the hydrodynamic diameter (H_D) for increased PEG molecular weights coated on for four core diameter gold nanoparticle samples.

2.2.3. UV/Vis absorbance:

A Varian (Agilent) Cary 5000 UV/Vis Spectrometer was used to obtain optical absorbance data. Cuvettes are used to hold liquid samples; the volume and material of cuvettes are dependent on the analysis being performed. Within this thesis the optical absorbance data was obtained from 250 nm – 800 nm (unless otherwise stated) and samples are run in either 0.5 mL small volume quartz cuvettes (protein stock solutions) or poly methyl methacrylate (PMMA, optically clear to 300 nm) disposable 4.5 or 2.5 mL

cuvettes. All samples are run with a baseline correction scan on an identical cuvette filled with solvent (a blank) initially on both beams and then with a blank sample in the rear beam position during analysis. Absorbance characteristics relevant for the gold and quantum dots materials used in this work include the identification of peaks whose height, position, and width can be used to infer information about nanoparticle samples based on size (Figure 2.4A), concentration (Figure 2.4B), shape, and/or purity. The extinction coefficient (ϵ, M^{-1} cm^{-1}) used to determine the concentration of gold nanoparticles changes based on the size of the particles. It can be calculated for any spherical gold nanoparticle sample using Equation 2.1 based on the natural log (ln) of the core particle diameter (d, nm) determined using TEM analysis.[4]

Equation 1.1. Extinction coefficient gold nanoparticles

$$\mathbf{ln(\epsilon) = 3.2111\,(ln(d)) + 10.80505}$$

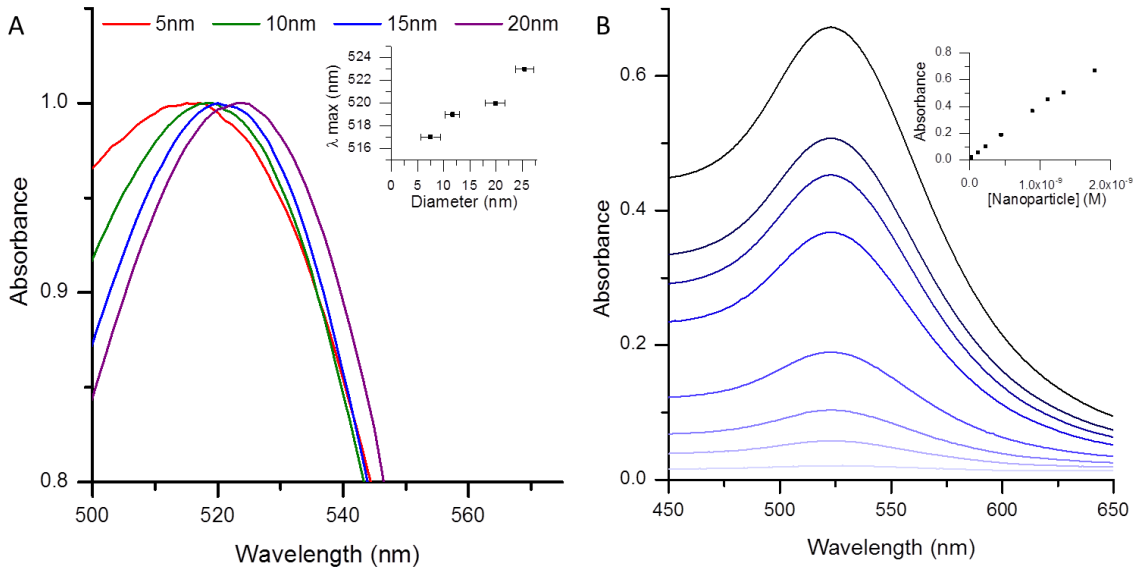

Figure 1.11. UV-Vis Analysis.

Absorbance information can be used to evaluate gold nanoparticles for a number of characteristics, such as: (A) size and (B) concentration.

2.2.4. Analytical ultracentrifugation (AUC):

A Beckman XL-A Analytical Ultracentrifuge equipped with a UV/Vis detector and an An60 four position rotor was used to run velocity sedimentation analyses on 420 μL liquid samples housed in 12mm, dual window, epon centerpieces. Centrifuge speeds and scan rates are chosen so the sample absorbance boundaries remain vertical and migrate uniformly for at least 40 scans. Sedimentation coefficient distributions for each sample were obtained using SEDFIT ls(g*) analysis, which is design to monitor large, discreetly sedimenting particles without interactions or back diffusion. The peak s-values are a direct measurement of particle size and density and therefore are useful for evaluation of particle size, surface functionalization or bioconjugation.[12-15]

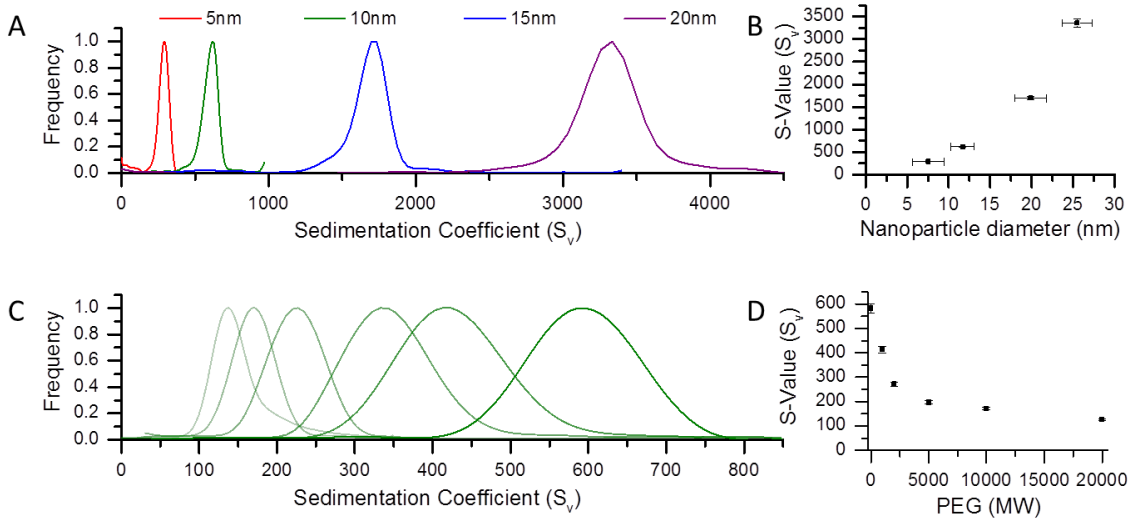

Figure 1.12. AUC Analysis.

Analytical ultracentrifugation used to determine the sedimentation coefficient distribution of nanoparticles based on their size and density. (A) Nanoparticles from 5 to 20 nm are evaluated and (B) plot of s-value vs. diameter is a cubed fit. (C) Increasing the molecular weight of the polymer coating materials decrease the particle density and (B) decreases the sedimentation coefficients.

2.2.5. Total organic carbon analysis (TOC):

Organic carbon concentrations were determined using Shimadzu TOC-L run on either a non-purgeable organic carbon concentration analysis (NPOC) or total organic, inorganic and nitrogen (TOC/TN) concentrations analysis. The non-purgeable organic carbons in solution were used to quantify carbon containing polymers and Figure 2.6 shows this information can be used to evaluate the efficacy of a cleaning procedure or determine surface functionalization on nanoparticles. Alternatively, the nitrogen concentration can be used to quantify proteins in solution making it useful to evaluate bioconjugation or protein crystallization yields.

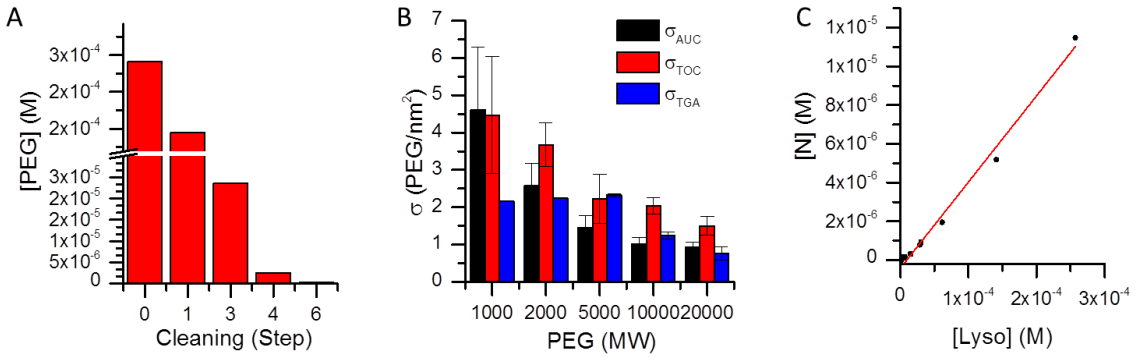

Figure 1.13. TOC Analysis.

Total organic carbon analysis is used to determine carbon and nitrogen concentration of solutions. This information can be used to (A) evaluate cleaning procedures, (B) monitor surface functionalization, or (C) detect protein concentration.

2.2.6. Thermogravimetric analysis (TGA):

TA Instrument's Q-600 Simultaneous TGA/DSC is run on approximately 1 mg of gold or PEGylated gold nanoparticle samples (~9.0 nM) which requires 10 mL of sample to be concentrated to <100 µL, which is then dried on the TGA to obtain a powder. Each concentrated sample was first dried at 100 °C for 60 min to remove excess water and then baked at 140 °C for 60 min to remove the bound water. Analyses were performed under a 100 mL/min flow of air and using a stepwise isotherm method where the temperature was ramped from 150 °C to 1200 °C. Briefly, the stepwise isotherm method was designed to hold at temperatures where the rate of weight loss was greater than 1 wt% per min. However, when the rate of weight loss decreased below 1 wt% per min the temperature returned to a steady ramp of 5 °C per min. The mass of sample loss from 150 °C to 500 °C is attributed to the organic component.[16]

Figure 2.7A shows that a pure PEG powder loses most of its mass (>99%)between 150 °C and 500 °C with a maximum derivative peak at 229 °C (FWHM, 65 °C).[16] Thus, when similar mass changes are seen for polymer-coated nanoparticles it is possible to identify and ultimately quantify the amount of coating material. For example, Figure 2.7B shows the TGA data collected for for 10 nm gold coated with increasing molecular weight of PEG.

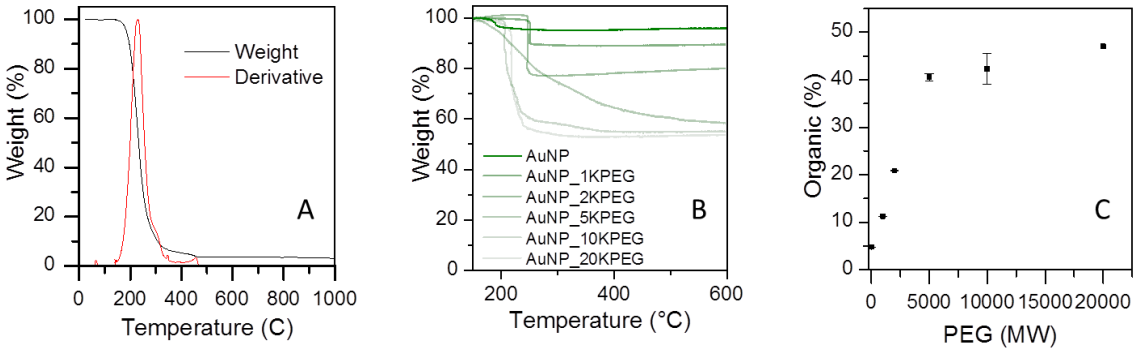

Figure 1.14. TGA Analysis.

TGA is used to determine the carbonaceous content of a solid sample through changes in weight during thermal ramping. This information can be used to evaluate (A) purity of organic materials, or (B) determine organic contribution from polymer surface functionalization on inorganic nanoparticles, (C) percent organic trends with PEG molecular weight.

2.2.7. Flocculation assay:

Flocculation assays are used to determine the minimum concentration of a precipitant that induces aggregation of nanoparticles. A colorimetric method was developed to detect the flocculation of gold nanoparticles to determine the stabilization effect of the polymer coverage, it was adapted from several similar methods.[17,18] Briefly, the optical

absorbance of samples housed in 96-well plates were collected using a SpectroMax brand UV/Vis multiwell plate reader at λ=520 nm for unaggregated particles and λ=595 nm for aggregated, Figure 2.8A. The precipitant concentration was varied systematically from 0 to 2.5 M (for salts) and the ratio of the aggregated to unaggregated absorbance peaks were used to determine the aggregation factor, which was a measure of the extent of aggregation. Figure 2.8B shows the results of a flocculation assay used to evaluate the effective polymer coatings on gold nanoparticles. The citrate stabilized gold nanoparticles have an aggregation factor >1 in relatively low ionic strength solutions, whereas, the addition of polymer coating materials adds stability to the nanoparticle sample and increased the amount of salt needed to induce aggregation. The minimum concentration of precipitant needed to induce aggregation is called the critical coagulation concentration (CCC), it is taken to be the concentration of salt where the aggregation factor raises by 15%. The CCC increased with more organic coating material (PEG) in solution, which show that polymers provide stability to the particles against the charged ions in the salt solution.

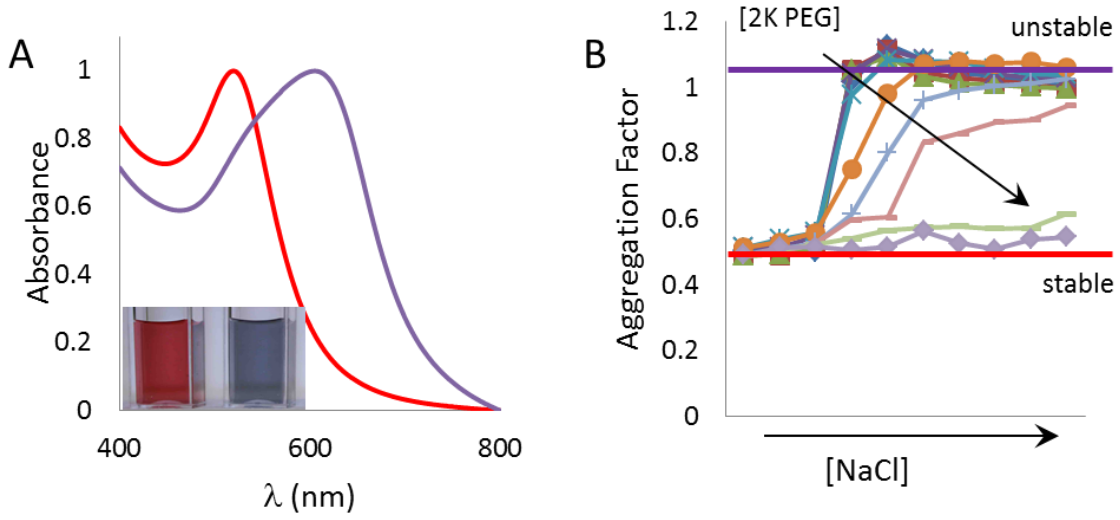

Figure 1.15. Flocculation Analysis.

(A) Flocculation assays use the shift in the plasmon resonances for gold nanoparticles due to aggregation to detect stability. The peak absorbance at 595 nm divided by the absorbance at 520 nm is used to calculate the aggregation factor, which is a clear indication if a sample is aggregated. (B) Flocculation data for a gold nanoparticle sample with increasing 2K PEG concentration what that with increased PEG concentration the sample becomes more resistant against aggregation in high salt concentration solutions.

2.2.8. Equilibrium dialysis:

Float-A-Lyzer® G2 1 mL screw top 100 MWCO dialysis cellulose ester membranes (Spectra/Por®) were filled with 100 µg/mL lysozyme solution and 4 nM polymer – nanoparticle conjugate material. Membranes were placed in 450 mL of 0.1 M sodium acetate (Fluka, 99.7%) buffer pH 4.6 and allowed to dialyze for 6 days. Protein and polymer – nanoparticle conjugate concentrations were determined for the sample

spectroscopically before dialysis and after to determine percent protein retained in the sample.

2.3. PROTEIN CRYSTAL PREPARATION

All protein crystallization experiments were run by me, however training and support and set up of the high throughput crystallization robot were provided by Kasia Walkiewicz from Dr. Shamoo's Lab.

2.3.1. Crystallization Buffers:

The crystallization procedure for lysozyme has been developed through evaluation of a range of protein concentrations, pHs, ionic strengths and additives; similar to conditions used by Falkner et al.[19] The standard procedure reported here has been chosen because it consistently yields crystals and not protein aggregates. Crystallization reagents consist of a solution of 0.1 M sodium acetate buffer at pH 4.6 and 1 M NaCl (Fisher, 99.7%, crystalline biological, certified) (unless otherwise stated). The buffer was prepared by dissolving 8.2 mg sodium acetate (Fisher, Certified ACS, 99.7%) per mL of water and adjusting the pH using 12.1 M HCl (EMD chemical, ACS grade). All solutions were vacuum filtered through a 0.2 μm filter to remove any possible contaminants then stored in tightly sealed glass media bottles for storage. Solutions were considered stable and usable while they remain optically clear and their pH is within ± 0.1 of the initial preparation.

2.3.2. Protein Stock Solutions:

Lysozyme (Aldrich, >98%) stock solutions were prepared in 0.1 M pH 4.6 acetate buffer, where ~50 mg protein/mL was added, and the solution was mixed until transparent, then gently centrifuged at 3.3K RPM for 10 minutes to remove any impurities or undissolved protein. The actual protein concentration was determined photometrically using the optical absorbance at 280 nm of a 100X diluted solution. The final concentration was calculated using Beer's Law with an extinction coefficient of 2.64 mL mg^{-1} cm^{-1}.[19,20]

Protein stock solutions: Pure protein samples of ferritin (pure), human serum albumin (HSA) (>97%), (Sigma Aldrich) lipase B, xylanase, and glucose isomerase (Crystallization standards, pure, Hampton Research). Stocks were suspended in filtered solutions, and centrifuged gently at 3.3K RPM for ten minutes to remove any undissolved materials. Protein concentration was determined spectroscopically at 280 nm using extinction coefficients provided by the manufacturer where available or a generic 1 mg/mL per absorbance unit, when no extinction coefficient could be found. As purchased ferritin stock solutions are 50 mg/mL and were diluted to 30 mg/mL using MilliQ DI. Dried lyophilized powders of HSA were measured out to be 10 mg/mL into 0.01 M phosphate buffer pH 7.0. Lipase B stock solution was prepared by weighing out enough materials to produce a 35 mg/mL solution in MilliQ DI. The stock solution for xylanase started at 30 mg/mL and was diluted to a final concentration of 18 mg/mL using MilliQ DI. Glucose isomerase suspended microcrystals were dialyzed in 10 mM HEPES (Aldrich, >99.5%)buffer pH 7.0 with 1mM $MgCl_2$ (Aldrich, Certified ACS) overnight,

and then diluted to a final concentration of 10 mg/mL using the same solution of HEPES and MgCl.

2.3.3. Protein Crystallization Methods

2.3.3.1. Hanging drop method:

Hanging drop crystals were formed via a vapor diffusion method as shown in Figure 2.9A. Small volumes of crystal reagent solution and protein were suspended from silicone coated glass cover slips covering each reservoir in pre-greased 24-well plates (Hampton Research). Reservoir solutions are prepared with the crystallization reagent. Within each sample droplet there is 1 μL of reservoir solution, 2 μL of the lysozyme stock solution and 1 μL of nanoparticle additive solution or DI. The cover slip was then inverted over the well and pressed into the vacuum grease to create a seal. The well plates were placed in a temperature controlled environment (10 ºC ± 1ºC) and allowed to crystallize.

2.3.3.2. Sitting drop method:

A vapor diffusion crystallization method was also used to form crystals in small volume solutions for a sitting drop crystallization method. As shown in Figure 2.9B, the solution sits on a platform in the middle of the each well in a 24-well sitting drop plate (Hampton Research). Reservoir solutions were prepared with the crystallization reagent. Each crystallization drop contained 2 μL of reservoir solution, 4 μL lysozyme stock solution and 2 μL of nanoparticle sample or DI water. The well plates were then sealed with tape

and placed in a temperature controlled environment (10 ºC ± 1ºC) and allowed to crystallize.

2.3.3.3. High Throughput Crystallization Method

*High throughput experiments run on the Gryphon Robot were programed and executed with the help of Kasia Walkiewicz, in the Shamoo Lab.

A high throughput robot (ARI Gryphon) was used to prepare sitting drop well plates with 96 crystallization conditions for quick screening of proteins in an array of potential crystallization conditions to determine which set of conditions promote crystal formation. Protein stock solutions without and with nanoparticles were automatically dispensed into small volume, 3-position, sitting drop, 96-well plates prepared with one of two set of conditions: Index Screen (Hampton Research) or PEG SuiteI (QIAGEN). The robot was programmed to deliver 0.3 μL reagent (taken from the screen solution) and 0.3 μL of the protein sample into each divot. After the samples were dispensed the well plates were sealed with optically clear tape and placed in a temperature controlled environment (10 ºC ± 1ºC). Each condition was evaluated based on the number of conditions that produce crystals, precrystallization materials (i.e. sheets, blobs or microcrystals) and/or aggregation.

2.3.3.4. Batch method:

For batch method crystallization the buffer, salt, protein and any additives (nanoparticles) were mixed together in larger volume solutions between 100 μL and 100 mL, depending on the container. This method was most appropriate for analysis of the crystallization process because the larger solution volumes produced more crystals. Containers were

selected that could be sealed tightly and hold the desired amount of solution; most commonly 100 - 200 μL batches were prepared in 96 well plates, 1 - 3 mL batches were prepared in either 1.5 mL centrifuge tubes or 4.5 mL cuvettes (shown in Figure 2.9C) and 10 mL batches were prepared in 15 mL centrifuge tubes. Larger samples were made in cell culture flasks or media bottles. Crystallization reagents included a 0.1 M acetate buffer, pH 4.6, and 1 M NaCl solutions similar to those used for the hanging and sitting drop methods. The only differences for the batch method crystallization are (1) that proteins and nanoparticles are combined together initially and (2) lower protein concentrations are used (2 – 8 mg/mL as compared to 25 mg/mL).

Typically, nanoparticle concentrations of 3.8 nM were used in batch methods, unless otherwise stated. The order materials were added into the solutions was important to keep nanoparticles and proteins from aggregating; first the buffer and water were combined, then the protein solution was added, followed by the nanoparticle solution and finally the salt solution. Solutions were mixed thoroughly until refractive index lines from the salt were no longer visible and the mixture appeared uniform to the naked eye. Samples were then sealed and placed in a temperature controlled environment (10 ºC ± 1ºC) for at least 12 hours. Most of the crystals settle to the bottom of the container during this time, but some cling to the sample walls. Gentle centrifugation was used to dislodge these wall-attached crystals.

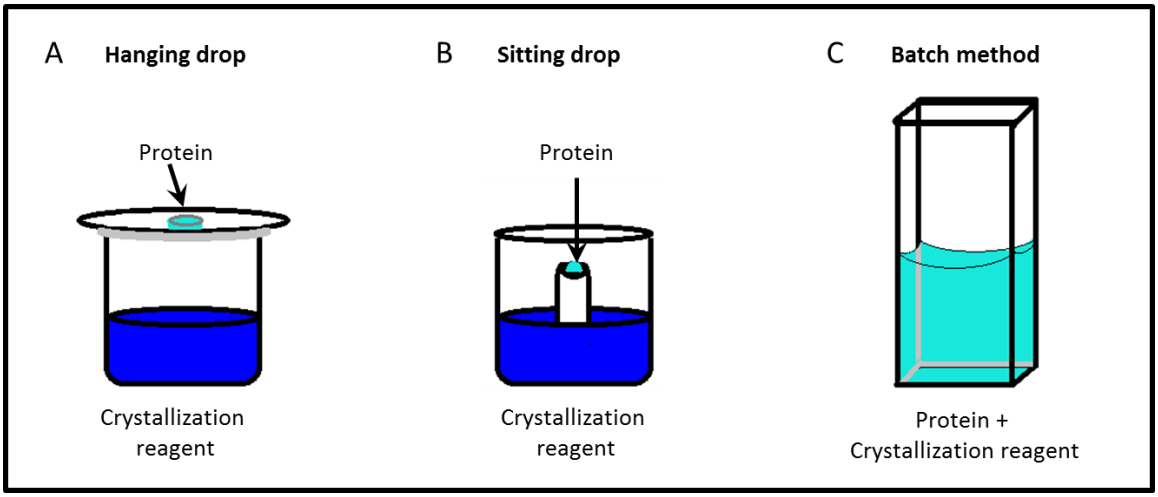

Figure 1.16. Crystallization Methods.

The three methods of crystallization are hanging drop, sitting drop and batch method. (A) Hanging drop the protein is suspended in a liquid droplet above the crystallization reagent reservoir on a cover slip and the well is seal with silicone grease. (B) Sitting drop the protein solution is sitting on a pedestal in the middle of the reservoir and sealed shut with tape. (C) Batch method mixes the protein and crystallization reagent in one solution and is sealed with tape.

Crystals formed via the three methods: hanging drop, sitting drop and batch method, usually differed in concentration, size and rate of formation. Figure 2.10 shows optical microscope images for all three methods; hanging drop (A), sitting drop (B) and batch method (C). Hanging drop crystals were typically larger and less abundant. Sitting drop method typically formed crystals quicker than hanging drop and produced slightly more crystals that were about the same size. The batch method produced the most crystals, smaller in size and typically faster than either of the other techniques.

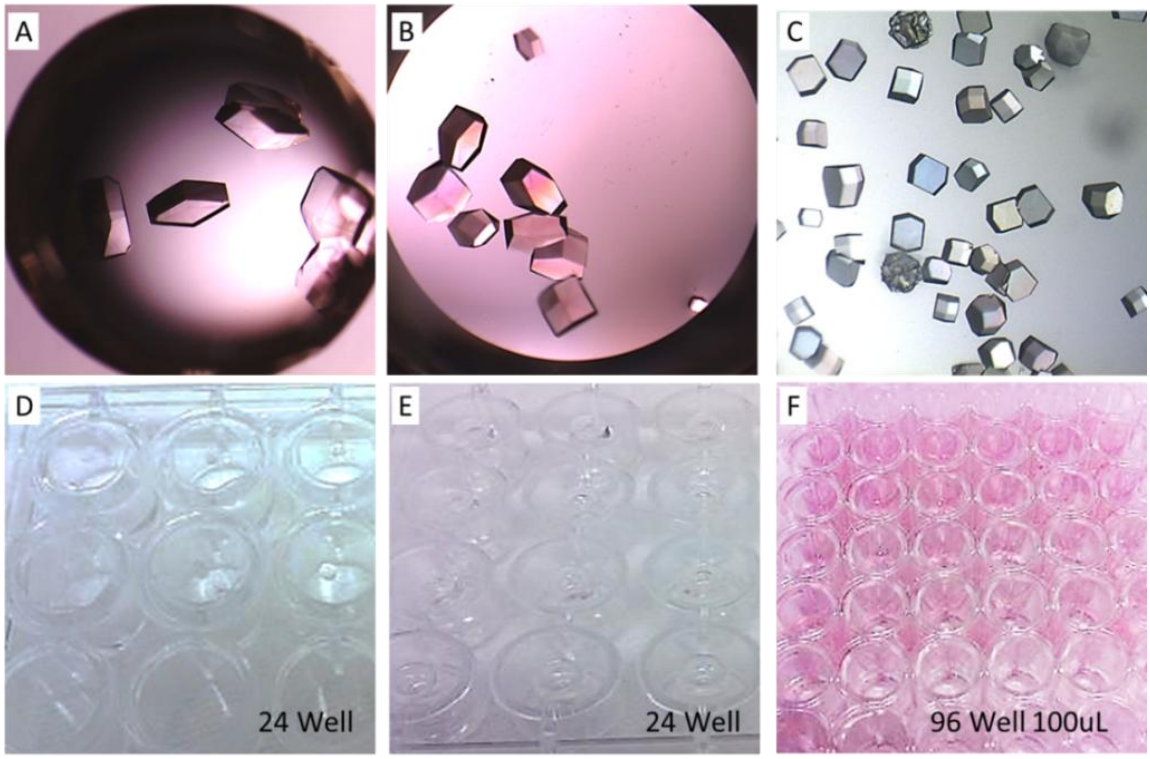

Figure 1.17. Protein Crystals.

(Top row) Typical crystals formed via each method: (A) hanging drop, (B) sitting drop and (C) batch method. (Bottom row) Experimental setup for each method: (D) hanging drop, (E) sitting drop and (F) batch method.

2.3.4. Purification of crystals:

Purification allowed the crystals to be separated from residual protein and nanoparticles in solution. Gentle centrifugation using slow speeds, up to 10K RPM for 60 seconds provided a collection of crystals at the sample bottom; faster speeds can crack or damage the crystals. The crystal pellet was rinsed with fresh crystallization reagent; use of other solvents could dissolve or destroy the crystals. Purification was performed three times to ensure free protein was removed and crystallization was stopped.

2.3.5. Crosslinking of crystals:

To provide more stable crystals for x-ray diffraction and imaging, the crystals were cross-linked using 2-3% gluteraldehyde (Sigma – Aldrich, grade I) in fresh crystallization reagent overnight. Crosslinked crystals could be cleaned repeatedly using Millipore DI water to remove crosslinking materials, buffer and salt from solution.

2.3.6. Embedding crystals in resins:

To examine sections of the crystals via TEM and SEM, the clean and crosslinked samples were prepared in a resin and cut on a microtome. Three types of resins and molds were evaluated for embedding protein crystals. Resins tested consisted of a photo-crosslinked, a thermally crosslinked (Ted Pella), and a highly cross linked acrylate and methacrylate based embedding media (Electron Microscopy Sciences). These three were selected because they cure in less than 2 days and were reported to be inert to the gold nanoparticles. The photo-crosslinked resin did not cure uniformly under UV light; after four days the external surfaces were hard but the interior was malleable and not suitable for clean sectioning. The thermally crosslinked resin did cure uniformly. However, the heat either dissolved or otherwise disrupted the crystals. Only the acrylate and methacrylate based embedding resin fully cured into a hard material without destroying the embedded protein crystal.

The mold shapes were chosen to optimize the cured sample homogeneity and fit within the microtome sample holder. In general, flat molds ~0.1 cm high and less than 1 cm wide, cure the fastest and fit the best in the microtome sample holder, but the crystals are

all isolated at the bottom of the mold and more difficult to access for cutting. A small cone shaped mold took a little longer to cure, but the crystals collected in the tip making it easier to both load and section on the microtome.

2.3.7. Microtome:

A Lewicka Ultramicrotome with a glass blade was used to sections crystals. The resins containing nanoparticle-protein samples were mounted on the microtome and excess resin was trimmed away from the crystal leaving a 1 mm X 1 mm square area for sectioning. A reservoir boat was affixed to the end of the blade with nail polish and filled with water. Sections were cut at speeds not greater than 10 mm / sec and at thickness < 200 nm (typically between 50 – 100 nm). A ribbon of sample was produced after multiple cuts and this was transferred to TEM 300 mesh copper grids by submerging the grids in the water and scooping the sample off the surface.

2.4. CRYSTAL CHARACTERIZATION

2.4.1. Kinetics of crystal formation:

The method used to determine the kinetics of lysozyme crystal formation was modified from a method reported by Bessho *et. al.*. This approach monitored the change in protein concentration via optical absorbance during crystallization in real time (from 1 to 5 days) using a Cary 5000 UV/Vis.[21] Batch method crystallization solutions were prepared in 4.5 mL cuvettes which were housed in a 6x6 peltier temperature controlled autosample holder (Varian). Scanning kinetics software was used to obtain absorbance scans from

220 nm to 800 nm during the course of the experiment, the frequency of collection was set to increase with time: every 15 minutes for the first 6 hours, then every 30 minutes out to 12 hours, followed by once an hour out to two days and once every 2 hours for the remainder of the evaluation.

Figure 2.11A shows the absorbance spectra collected from 250 to 800 nm, on a protein and nanoparticle sample. Protein concentrations are typically monitored at 280 nm, however at the concentrations used for crystallization absorbance the signal at 280 nm saturates the detector and does not have a linear concentration dependence (Figure 2.11B), therefore the absorbance at 301 nm was monitored to determine protein concentration, and the absorbance peak at 523 nm was monitored for nanoparticle concentration. Real time detection of the change in concentration over time provided a measure of the crystallization processes including the induction, nucleation, growth and equilibration phases; Figure 2.11C shows these regions in green, blue, purple and red, respectively.

Initially, the solution has no change in optical absorption and this is generally referred to as the induction phase. At the nucleation time (T_{nuc}), the concentration of protein in solution begins to decrease and what follows is a steady decline indicative of the growth phase. For our evaluation T_{nuc} is taken to be the intersection of the where the linear fits for the induction phase and the growth. Figure 2.11D shows the change in the optical absorbance for lysozyme at 5, 10 and 20 °C, which results in T_{nuc} values of 150, 1700, 3970 minutes, respectively.

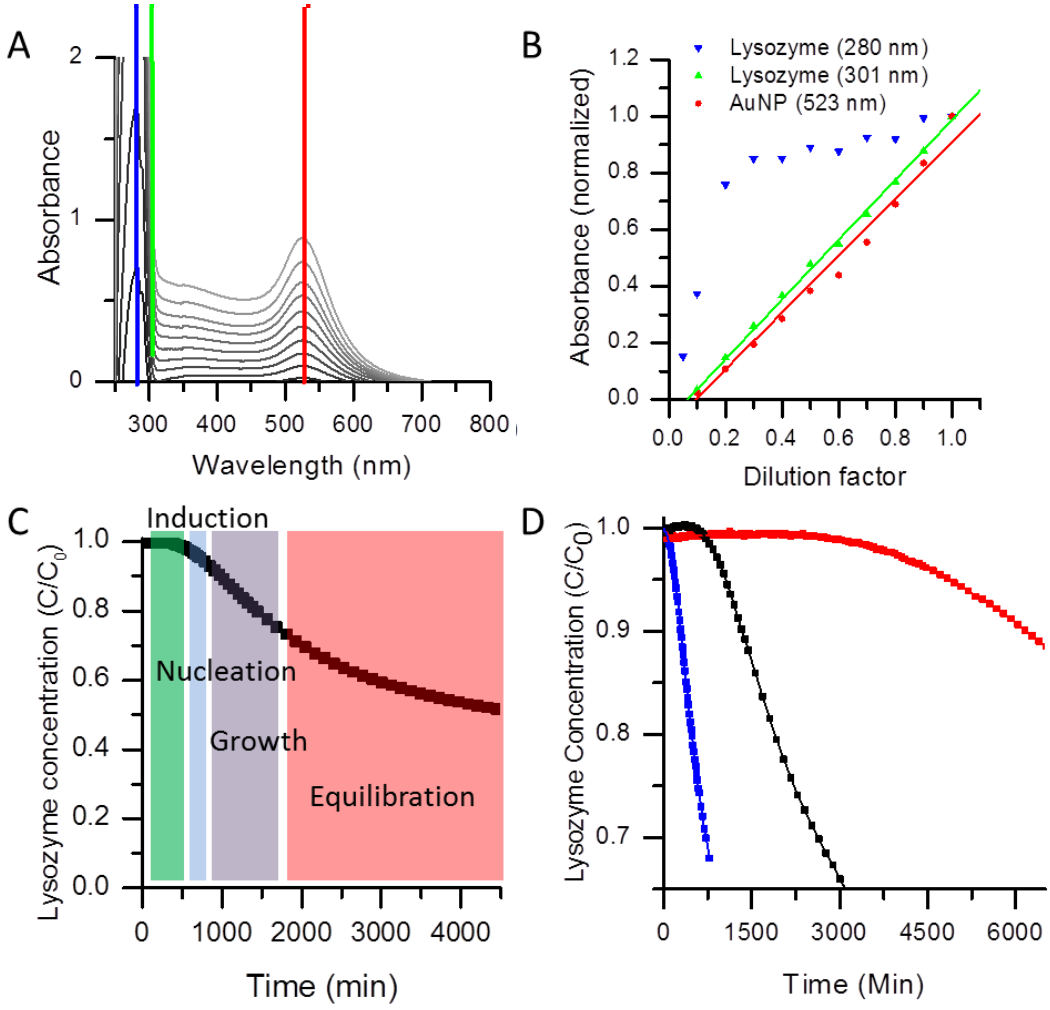

Figure 1.18. Kinetics of Crystal Nucleation Method.

(A) Absorbance peaks at 280 nm (blue), 301 nm (green) and 523 nm (red) decrease as the sample is diluted. (B) Linear absorbance change with concentration show that the protein concentration can be determined from the absorbance at 301 nm (green line) and the nanoparticle concentration can be monitored with a peak at 523 nm (red line). (C) The plot of protein concentration over time is used to determine the four phases of crystallization are: Induction (green), nucleation (blue), growth (purple) and equilibration (red). (D) Lysozyme crystallization monitored at three different temperatures 5, 10 and 20 °C.

2.4.2. Phase maps:

Phase maps are designed to monitor the solubility of a protein under a wide variety of conditions so as to optimize the conditions that form crystals as opposed to precipitates.[22,23] 200 μL batch method crystallization samples were prepared in 96-well plates. For the phase map in Figure 2.12, the lysozyme concentration was varied from 5 – 60 mg/mL and ionic strength was varied from 0.5 – 4.0M, while keeping constant the buffer strength (0.1 M), temperature (10°C), pH (4.6) and the nanoparticle concentration, 0 for Figure 2.12A, and 3.8 nM for Figure 2.12B. Each well represents a unique condition which is classified at 1 hour after mixing as a (1) clear solution – blue square (2) precipitate / aggregated protein solutions – red square. After 12 hours the samples are analyzed again for (3) crystal formation – black diamond. Figure 2.12 shows two typical phase maps for lysozyme without (A) and with nanoparticles (B).

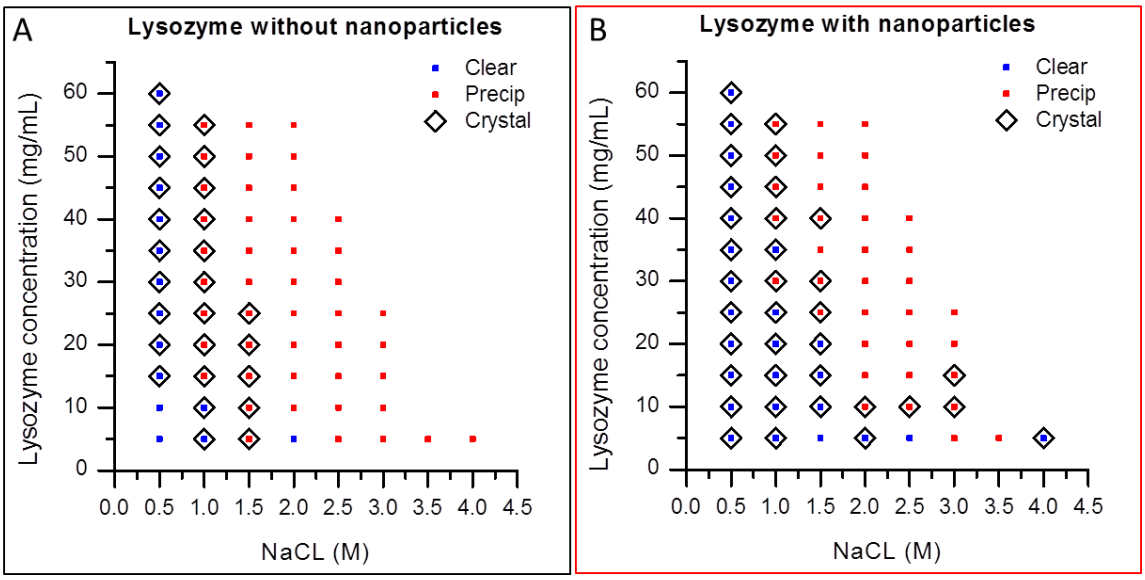

Figure 1.19. Protein Phase Diagrams.

Two phase maps for the crystallization of lysozyme (A) without and (B) with nanoparticles.

2.4.3. Microscopy/Imaging:

For hanging drop, sitting drop and small volume batch method crystals, images were obtained of the samples still in their original solution. However, larger volumes of the batch method produced crystals had to be removed from solution and evaporated onto glass microscopy slides for imaging. All images were obtained on an Olympus SZX16 microscope fitted with a Q-Imaging Go-3 camera. The images were capture and sized using QCapture Pro software.

2.4.4. Electron microscopy:

As-prepared, nanoparticle-protein crystals cannot withstand the high vacuum environments or intense electron beam irradiation. Crystal samples had to be prepared for imaging via crosslinking, followed by sputter coating of a thin layer of platinum or gold for SEM and microtome sectioning (See section 2.3.10. above) for TEM analysis.

2.4.5. Scanning electron microscopy (SEM),

***** All SEM samples were sputter coated and imaged by Zuzanna Lewicka from the Colvin Lab. I mounted each sample on the aluminum stub, was present for some of the imaging sessions and analyzed all the images.

Cleaned, crosslinked crystals were evaporated onto aluminum SEM stubs (Ted Pella) and allowed to dry. The samples were then coated with a thin layer (< 20 nm) of either platinum or gold, using a CRC-150 high voltage sputter coater. Images were obtained using a FEI Quanta 400 ESEM operated at 20kV. Better retention of the crystals during imaging were seen in the samples that were adhered to the SEM stub with double sided carbon tape.

2.4.6. Transmission electron microscopy (TEM):

Clean, crosslinked crystals were prepared for TEM imaging either by growing very small crystals, smashing or cutting larger crystals. Images of thick crystal samples on the TEM were obtaining using high angle angular dark field (HAADF) images in the scanning transmission electron microscopy (STEM) mode.

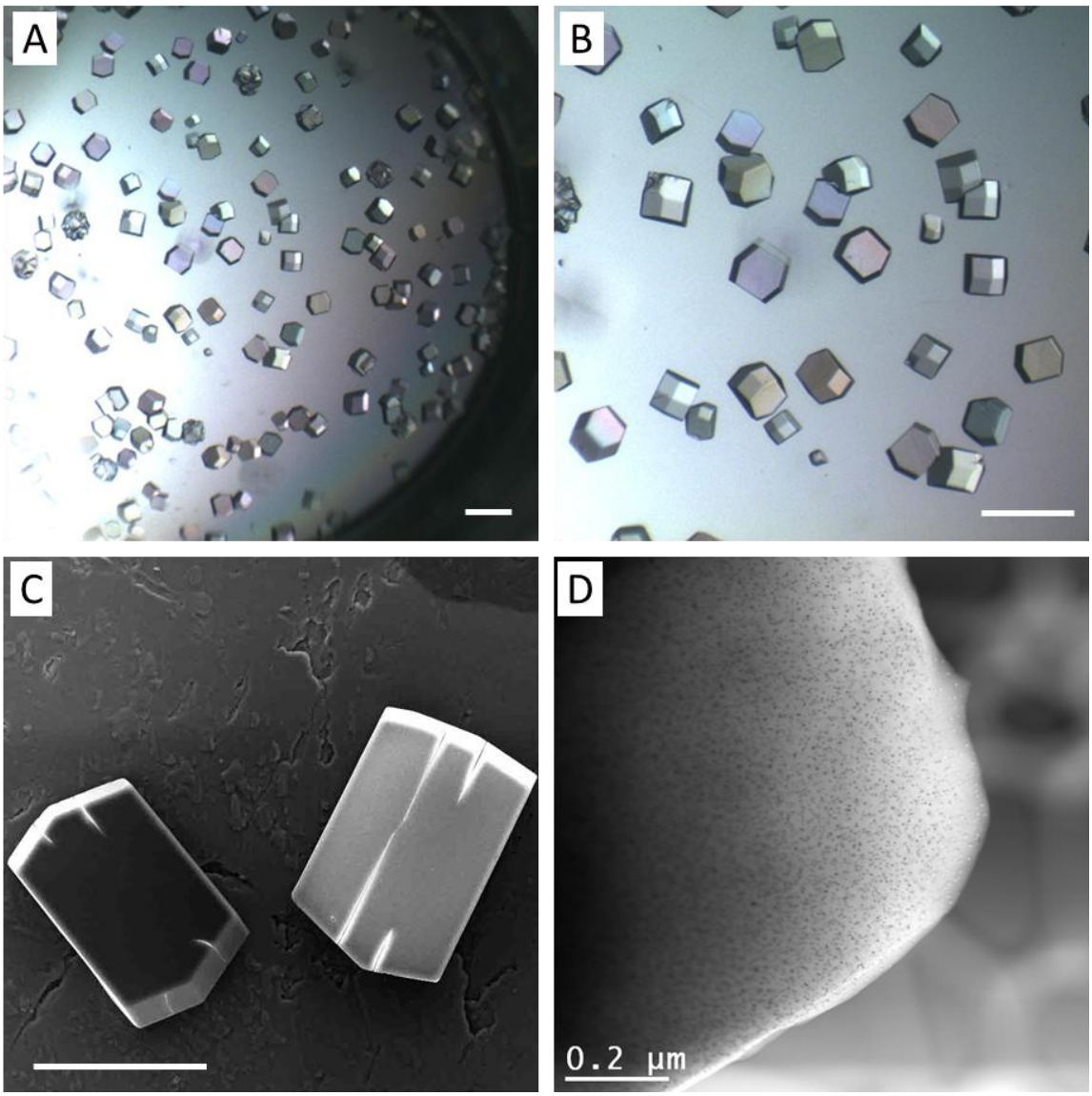

Figure 1.20. Imaging Lysozyme Crystals.

Images obtained using (A) optical microscope 2X, (B) 4X, (C) SEM 200X, and (D) TEM 60KX. All scale bars = 200 µm, except D = 200 nm.

2.4.7. Single Crystal Diffraction

*All single crystal diffraction data was collected and processed by Kasia Walkiewicz from the Shamoo Lab. All sample preparation and mounting of the crystals was done by me.

Uncrosslinked crystals were analyzed on a Rigaku cryo-beam X-ray diffractometer at 50kV and 100mA. Single crystals were mounted on a loop and then dipped in a cryo-protectant glycerol solution; 30% glycerol solution and crystallization reagent (0.1 M Acetate buffer pH 4.6 and 1 M NaCl). The crystal was then mounted in the beam line, as shown in Figure 2.14A and placed 120 cm from the detector. Cu kα radiation (λ=1.5406) radiation was used for collection of diffraction data at every degree from 0 – 90º. Typical data is shown in Figure 2.14C.

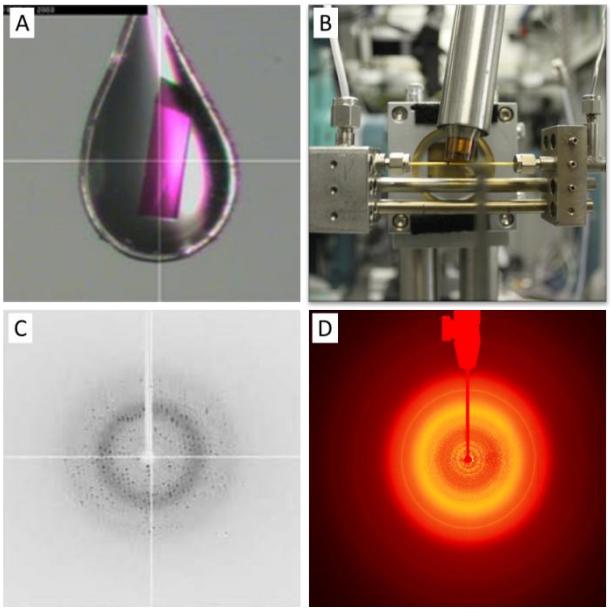

Figure 1.21. Diffration

(A) Crystal set up for single crystal or (B) powder diffraction. Typical data, (C) for a single crystal pattern is a series of dots, and (D) for powder XRD the patterns are sets of rings.

2.4.8. Powder XRD

*All in-house powder XRD collections were run by Carolina Avendano or Arjun Prakash from the Colvin Lab. They also provided help analyzing the peak positions and sample data.

Clean, crosslinked and dried crystals were run on either a Rigaku D-Max Ultima-II powder XRD or on the 1-BM beam line at the Advanced Phonton Source at Argonne National Laboratories. Data was collected on the Rigaku instrument at 40 keV and 40 mA using a zero background sample holder and a Cu kα radiation (λ=1.5406). Scans were collected for 7.5 hours over a theta range of 1 - 90º. Jade 8.5 software was used to match expected gold peaks and find the d-spacing for lysozyme crystal peaks. APS powder diffraction patterns are collected on ground crystal samples mounted in 0.7 mm Kapton capillaries with filters (shown in Figure 2.14B), using the 1-BM line run at 20keV with 60 second exposures the data was collected from 0.6 – 35º. Typical powder diffraction data is a series of rings as shown in Figure 2.14D.

2.4.9. UV/Vis:

Absorbance data for solid protein crystals were collected for an ensemble or a single crystal.

2.4.9.1. Solid ensemble:

Ensemble data was collected on a set of clean, crosslinked crystals dried onto a glass microscope slide, which was affixed to the Varian Cary 5000 using an appropriate

aperture which blocks excess beam and holds the sample in place for measurement; care must be taken to apply enough sample to obtain absorbance and not too much to completely block the beam. The same size aperture and a clean glass slide were also placed in the reference beam line.

2.4.9.2. Single crystal polarization dependent absorbance,

* All single crystals polarization dependent absorbance data and pictures were acquired by Lindsey Anderson in the Hafner Lab. I prepared all samples and participated in finding an appropriate crystal to analyze.

Single crystal absorbance spectrum was collected with an epi-illumination dark field microscope (Zeiss Axiovert 200M) equipped with a rotatable polarizer placed in the scattered beam path. Spectra were obtained with an imaging spectrograph (SpectraPro 150, Princeton Instruments). For composite crystals containing gold nanorods, spheres or bipyramids the spectral properties were measured as a function of polarization angle for different areas on the crystal through a 10 micron slit. For each wavelength monitored, the detector dark counts were subtracted from the signal then the signal from the crystal was normalized to the background.

2.4.10. Magnetization – SQUID

* All SQUID data was acquired and processed by Chris Jones or Carolina Avendano from the Colvin Lab.

Composite crystals containing magnetic nanoparticles were measured using a Superconducting Quantum Interference Device (SQUID) (Quantum design). Clean, crosslinked crystals were dried out of solution and housed in a plastic tube. Analysis was run to collect hysteresis loops at 300K and 5K as well as the ZF/FC curves for samples

with and without nanoparticles present. These properties were compared to the unbound nanoparticles free of protein crystals.

2.5. REFERENCES

(1) Frens, G. *nature physical science* **1973**, *241*, 20.

(2) Kumar, S.; Aaron, J.; Sokolov, K. *Nat. Protocols* **2008**, *3*, 314.

(3) Lisensky, G. *http://mrsec.wisc.edu/Edetc/nanolab/gold/index.html* **2011**.

(4) Liu, X.; Atwater, M.; Wang, J.; Huo, Q. *Colloids and Surfaces B: Biointerfaces* **2007**, *58*, 3.

(5) Sau, T. K.; Murphy, C. J. *Langmuir* **2004**, *20*, 6414.

(6) Lee, S.; Mayer, K. M.; Hafner, J. H. *Anal. Chem.* **2009**, *81*, 4450.

(7) Liao, H. W.; Hafner, J. H. *Chem. Mat.* **2005**, *17*, 4636.

(8) Zhu, H.; Prakash, A.; Benoit, D. N.; Jones, C. J.; Colvin, V. L. *Nanotechnology* **2010**, *21*, 255604.

(9) Yu, W. W.; Falkner, J. C.; Yavuz, C. T.; Colvin, V. L. *Chemical Communications* **2004**, 2306.

(10) Yu, W. W.; Chang, E.; Falkner, J. C.; Zhang, J.; Al-Somali, A. M.; Sayes, C. M.; Johns, J.; Drezek, R.; Colvin, V. L. *Journal of the American Chemical Society* **2007**, *129*, 2871.

(11) Lewinski, N. A.; Zhu, H.; Jo, H.-J.; Pham, D.; Kamath, R. R.; Ouyang, C. R.; Vulpe, C. D.; Colvin, V. L.; Drezek, R. A. *Environmental Science & Technology* **2010**, *44*, 1841.

(12) Calabretta, M.; Jamison, J. A.; Falkner, J. C.; Liu, Y.; Yuhas, B. D.; Matthews, K. S.; Colvin, V. L. *Nano Lett.* **2005**, *5*, 963.

(13) Calabretta, M. K.; Matthews, K. S.; Colvin, V. L. *Bioconjugate Chemistry* **2006**, *17*, 1156.

(14) Jamison, J. A.; Krueger, K. M.; Mayo, J. T.; Yavuz, C. T.; Redden, J. J.; Colvin, V. L. *Nanotechnology* **2009**, *20*, 355702.

(15) Jamison, J. A.; Krueger, K. M.; Yavuz, C. T.; Mayo, J. T.; LeCrone, D.; Redden, J. J.; Colvin, V. L. *ACS Nano* **2008**, *2*, 311.

(16) Xie, J.; Xu, C.; Kohler, N.; Hou, Y.; Sun, S. *Advanced Materials* **2007**, *19*, 3163.

(17) Shipway, A. N.; Lahav, M.; Gabai, R.; Willner, I. *Langmuir* **2000**, *16*, 8789.

(18) Liu, Y.; Shipton, M. K.; Ryan, J.; Kaufman, E. D.; Franzen, S.; Feldheim, D. L. *Analytical Chemistry* **2007**, *79*, 2221.

(19) Falkner, J. C.; Al-Somali, A. M.; Jamison, J. A.; Zhang, J.; Adrianse, S. L.; Simpson, R. L.; Calabretta, M. K.; Radding, W.; Phillips, G. N.; Colvin, V. L. *Chemistry of Materials* **2005**, *17*, 2679.

(20) Sophianopoulos, A. J.; Rhodes, C. K.; Holcomb, D. N.; Van Holde, K. E. *Journal of Biological Chemistry* **1962**, *237*, 1107.

(21) Bessho, Y.; Ataka, M.; Asai, M.; Katsura, T. *Biophysical Journal* **1994**, *66*, 310.

(22) Anderson, M. J.; Hansen, C. L.; Quake, S. R. *Proceedings of the National Academy of Sciences* **2006**, *103*, 16746.

(23) Ries-Kautt, M. M.; Ducruix, A. F. *Journal of Biological Chemistry* **1989**, *264*, 745.

Chapter 3

MEASURING POLYMER GRAFTING DENSITY ON NANOPARTICLES: ANALYTICAL ULTRACENTRIFUGATION AND TOTAL ORGANIC CARBON ANALYSIS

Proteins interact with the surfaces of inorganic nanoparticles. For nanoparticles stabilized in biological media, these interfaces are defined by the polymeric coatings attached to nanoparticles. These coatings ensure steric stabilization, and thereby prevent nanoparticle aggregation. These coatings also mediate protein-nanoparticle interactions, and to understand and control these interactions requires detailed information about the polymer structure. Of particular importance in this work is the concentration of polymers

*Work performed within this chapter was performed by myself with some addition help from interns in the Colvin lab: Raymond Verm (DLS evaluation), Michael Lilierose (grafting density effects: sample preparation and stability evaluation), and Naushaba Ali (TOC evaluation).

at the interface, a parameter commonly referred to as the grafting density. Quantitative analysis of this parameter while nanoparticles are dispersed in solution is a significant measurement challenge. In this Chapter we introduce methods to apply both analytical ultracentrifugation as well as total carbon analysis to the problem. We compare the results from both approaches for a wide range of gold nanoparticle diameters as well as tethered polymer chain lengths, and validate these data using a solid state measure of total carbon content. We also illustrate how the information can be used to monitor the grafting of polymers onto particle surfaces, as well as discern trends in the equilibrium grafting density with particle diameter and polymer chain length.

3.1. INTRODUCTION

The number of bound polymers per surface area (grafting density) is a critical feature to control when designing nanoparticles for biological or environmental applications; this parameter directly affects the hydrodynamic diameter and colloidal stability of nanoparticles – factors crucial in biological and environmental applications.[1-11] Liu *et al*, for example, found 10 nm gold particles partially coated with polymer aggregated in a dilute salt solution. However, when the surfaces were fully covered, corresponding to grafting density of 50 chains/particle, the sample was stable in a 1 M NaCl, solution.[1] Others have noted the relationship of nanoparticle grafting density to biological behavior. Biodistribution studies of poly(ethylene glycol) (PEG) coated nanocapsules found a strong correlation between circulation time and grafting density. Fully coated materials, for example, had longer blood circulation times and reduced clearance by the liver,

spleen and kidneys as compared to materials which had 20% less surface-bound polymer.[2] This same factor influences a nanoparticle's transport through environmental matrices such as sand and water. When uncoated iron oxide nanoparticles were passed through a sand column only 30 cm long, 99% of the material was retained. In contrast, a partial coating of poly(acrylic) acid resulted in only 82% column attachment and an even more complete coating led to less than 50% column retention.[3]

These examples illustrate that qualitative measurements permit the distinction between higher grafting densities and lower grafting densities; however, more quantitative methods to define the actual number of polymers at a nanoparticle interface are not generally available. Theoretical estimates for the equilibirum or full coverage saturation grafting density can be found by assuming a particular size for polymers at a nanoparticle surface, and then deducing the theoretical grafting density at saturation using the available surface area of the core particle.[3,8,12]

Experimentally, approaches to this problem have relied either on the measurement of total carbon content in a solid nanoparticle-polymer sample (e.g. thermogravimetric analysis TGA) or on spectroscopic methods to indirectly assess coverages TGA is currently the gold standard but it requires large amounts of dried sample (> 1 mg).[6,8,13-16] Recently, a quartz crystal microbalance (QCM) was adapted for TGA of micrograms of powder and this may expand the application of TGA.[16] Spectroscopic methods rely on quantification of signals from the surface bound polymers to deduce coverages. For example, X-ray photoelectron spectroscopy (XPS) and nuclear magnetic resonance spectroscopy (NMR) can provide semi-quantitative assessment of grafting densities near

full coverage of polymers.[10,17-19] Alternatively, a labeling method can be used to displace fluorescent molecules at a nanoparticle surface and detect net quantum yield. These methods are difficult to generalize broadly both because they depend on the position and nature of the surface polymer features, and at least in the latter case are limited to only those particles that do not quench fluorescence. [8,20,21]

Here we address the challenge of nanoparticle surface characterization in solution by applying two techniques, analytical ultracentrifugation (AUC) and total organic carbon analysis (TOC), separately, to the measurement of the grafting density of gold nanoparticle-poly(ethylene) glycol conjugates. For these materials the surface polymers are added to the sample in a 'grafting-to' approach that makes estimates of surface coverage difficult particularly for low coverages of polymers. This problem prompted us to apply both AUC and TOC to the analysis of small volumes of nanoparticle solutions with the aim of extracting quantitative measures of the number of polymers bound to a particle.

We applied each method to a range of polymer chain lengths (1,000 to 20,000 molecular weights), polymer concentrations (8.5 nM – 8.5 μM) and a series of gold nanoparticles diameters (8 to 27 nm). First, the grafting density measured from both AUC and TOC over this wide range of conditions were within 30% of each other. Moreover, these results matched well to the values found from thermo-gravimetric analysis of dried milligram quantities of the same samples. Polymer concentrations as low as ten PEG per particle produced discernible changes in the surface coverage and both methods accurately detected changes in grafting density of less than ten percent. Conventional

thermogravimetric analysis is not sensitive enough to measure such small changes in polymer concentrations.

We used these tools to investigate several solution phase phenomena of both partially and completely coated nanoparticles. First, the aggregation behavior of gold nanoparticle-polymer conjugates in high ionic strength solutions was correlated quantitatively to the grafting density at the surface. As the polymer concentration in a sample increases, imparts steric stability which prevents the gold nanoparticles from aggregating. Interestingly, the nanoparticles can be stabilized in a monovalent salt solution with half the polymer concentrations needed for saturation using a high molecular weight polymer, but require an excess of 80% with a low molecular weight polymer coating. Second, we examined the trends in the saturation coverage as a function of chain length and particle size. Polymer grafting density decreased substantially as chain lengths increased for all nanoparticles sizes. In addition, the grafting density of low molecular weight PEG increases with increasing particle diameter.

3.2. GRAFTING DENSITY CALCULATIONS:

Scheme 3.1 Calculation flow diagram.

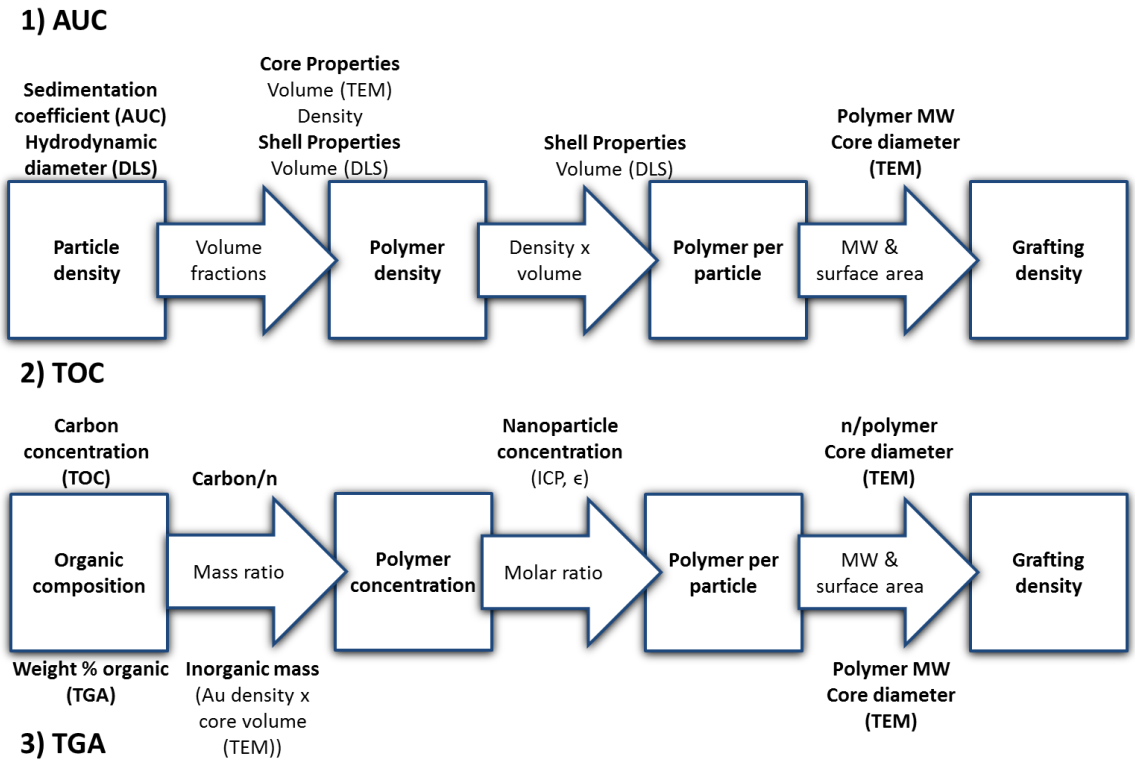

3.2.1. TGA grafting density

The grafting density (σ) from TGA was calculated using equation 1. First the relative mass of the polymer ($wt\%_{shell}$) is normalized to the mass of the inorganic nanoparticle ($wt\%_{core}$); taken from the experimental residual percent mass at 500 °C. The polymer mass is determined based on this percentage assuming the density of gold in a nanoparticle is the same as that of bulk gold (ρ_{core} = 19.6 g/cm^3). To convert this to the mass of a single particle, the volume is calculated assuming a spherical particle and the average radius found via TEM analysis (see Chapter 2.2.1). The number of polymers per

particle, N_{poly}, is determined by multiplying by Avogadro's number (NA) and dividing by the polymer molecular weight (MWt). The grafting density (σ) is found by dividing the polymer concentration per particle by the available surface area ($4\pi r^2$, r from TEM).

Equation 3.1. TGA grafting density

$$\sigma_{TGA} = \frac{\frac{wt\%_{shell}}{wt\%_{core}} \rho_{core} \frac{4}{3} \pi r_{core}^3 N_A}{MW 4\pi r_{core}^2}$$

3.2.2. TOC grafting density

Grafting density (σ) from TOC is calculated using equation 2. The nonpurgeable organic carbon concentrations ([C]), reported as ppm in a TOC analysis, should first be converted to molarity (moles/liter) by dividing by carbon's molar mass (12 g/mole). Then the molarity of carbon is used to determine polymer concentration from applying the ratio of carbons per monomer unit (2 for PEG) and the number of monomers (n) in each polymer sample (e.g. the molecular weight or MWt) divided by the weight of one monomer (44 g/mole for PEG). To determine the ratio of PEG molecules per particle, first the molar concentration of nanoparticles in solution ([NP]) must be determined; it can be determined based the optical absorbance of the gold nanoparticle solution.[22] Then the molarity of PEG is divided by the molarity of the nanoparticles, [PEG]/[NP]. The molar ratio of PEG molecules per particle once divided by the surface area of a particle (using the radius found using TEM) results in grafting density (σ).

Equation 3.2. TOC grafting density

$$\sigma_{TOC} = \frac{[C]n}{2[NP]4\pi r_{core}^2}$$

3.2.3. AUC grafting density

This approach takes a different approach to measuring the surface coatings of particles. It relies on the change in density induced by the association of lower density particles with the very dense gold cores. In effect, particles become less dense as more polymer is bound to them. This is quantified through measures of the sedimentation coefficient (s), a value related to particle density by equations 3 and 4. Other parameters that are important to the definition of the sedimentation coefficient include the solvent viscosity (η) and its density (ρ_s) as well as the particle's hydrodynamic diameter (d_h). While the first two parameters are easily obtained from the solvent itself (nanoparticle concentrations are too low to impact these values), the last parameter is challenging to measure particularly for undersaturated coatings.

Equation 3.3. Sedimenation coefficient (AUC)

$$s = \frac{d_h^2(\rho_p - \rho_s)}{18\eta}$$

Equation 3.4. Particle density (AUC)

$$\rho_p = \frac{18\eta s}{d_h^2} + \rho_s$$

The volume of the shell (V_{shell}) is the polymer thickness times the surface area ($4\pi\ r_{core}^{\ 2}$); where the thickness of the polymer layer is determined from the difference between the hydrodynamic radius (r_h, from DLS) and the radius of the core (r_{core}, TEM). The total density of the nanoparticle is the volume fraction of the core ($V_{core,}$ TEM) multiplied by the density of the core and the volume fraction of the shell multiplied by the density of the shell (equation 5). Given the density of the nanoparticle (equation 2) and the density of the core; which can be determine theoretically or by AUC evaluation of an uncoated particle, equation 5 is rearranged to solve for the density of the polymer shell (equation 6). From there the mass of polymer equals the volume of the shell times the calculated shell density. The mass is related to the number of polymers per particle using Avogadro's number (N_A) and the known molecular weight (MWt). Finally, the number of polymer molecules is normalized by the available surface area of the core nanoparticle ($4\pi\ r_{core}^{\ 2}$) resulting in the grafting density.

Equation 3.5. Density nanoparticle based on volume fraction (AUC)

$$\rho_p = \frac{V_{shell}}{V_p}\rho_{shell} + \frac{V_{core}}{V_p}\rho_{core}$$

Equation 3.6. Density polymer shell

$$\rho_{shell} = \frac{V_p\rho_p - V_{core}\rho_{core}}{V_{shell}}$$

Equation 3.7. Mass polymer shell

$$m_{shell} = \rho_{shell}V_{shell}$$

Equation 3.8 AUC grafting density

$$\sigma_{AUC} = \frac{m_{shell}}{MW \cdot N_A 4\pi r^2_{core}}$$

3.3. RESULTS AND DISCUSSION

3.3.1. Explanation of methods

This work compares the application of analytical ultracentrifugation (AUC) and total organic carbon analysis (TOC) to nanoparticle solutions for measurement of the surface coverage of bound polymers. We first introduce analytical ultracentrifugation which has conventionally been a tool for physical biochemists.[23,24] Over the last ten years, however, it has found increasing use in nanotechnology for the evaluation of size and size distribution of various nanocrystals; the bioconjugation of gold nanoparticles; and the surface structure and surfactant coating materials on carbon nanotubes.[25-32] AUC finds a sedimentation coefficient for every nanoparticle-polymer sample; this parameter depends sensitively on the overall nanoparticle-polymer density. If the hydrodynamic diameter of the overall nanoparticle-polymer can be accurately measured, this density can be used to determine the surface coverage of polymers.

Figure 3.1 illustrates how the sedimentation coefficients (e.g. s-value) vary for nanoparticle-polymer conjugates at saturation coverage. Data was collected as a function of core nanoparticle size (7.5 to 25.5 nm, panels A-D) as well as polymer chain length (1K to 20K MWt, panels E-F). TEM micrographs in Figure 3.1 show 7.5, 11.7, 19.9 and

25.5 nm diameter gold particles. AUC velocity sedimentation experiments run on each of these samples have increasing sedimentation coefficients (288 ± 7, 617 ± 15, 1697 ± 35 and 3359 ± 87 S_v) with increasing core diameter (Figure 3.1E). This trend is captured quantitatively in Figure 3.1F which illustrates the almost linear dependence on core diameter. Figure 3.1G shows that the addition of a polymer coating to the gold nanoparticles results in a decrease in their sedimentation coefficient; longer polymers have more of an effect on sedimentation. Figure 3.1H shows this relationship graphically as the molecular weight of the surface-bound polymer changes from 1K to 20K.

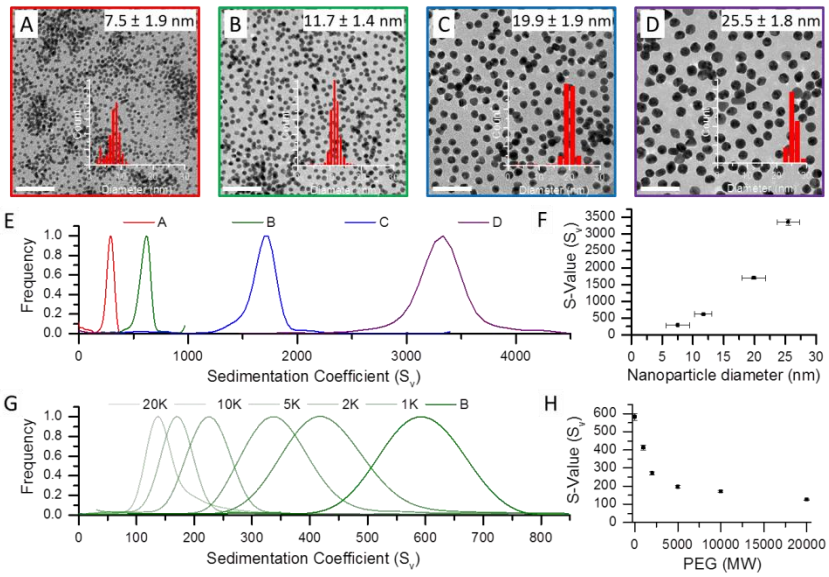

Figure 3.1 Analytical ultracentrifugation

Analytical ultracentrifugation (AUC) characterization of nanoparticles based on size and density. Transmission electron micrographs taken on four batches of gold nanoparticles reveal core diameters of (A) 7.5 ± 1.9 nm, (B) 11.7 ± 1.4 nm, (C) 19.9 ± 1.9 nm, and (D) 25.5 ± 1.8 nm (scale bars = 100 nm). Sedimentation coefficient distributions measured via AUC show an increase as a function of the diameter (E&F). Samples of B coated with PEG with increasing molecular weights, from 1K to 20K, show a decrease in the sedimentation coefficient distributions due to a decrease in the overall particle density (G and H).

The sensitivity of the sedimentation coefficient to the core size and the surface polymer chain length derives from its relationship to both hydrodynamic diameter and overall conjugate density (see equation 1.3 above). By measuring the hydrodynamic diameter (H_D) from DLS, and with known solution parameters such as solvent density and viscosity, it is straightforward to calculate the nanoparticle-polymer conjugate density. This data is reported in Table 3.1; nanoparticle-polymer conjugates have lower density than bulk gold due to the presence of the organic coatings. If the volume of the polymer shell is calculated from the hydrodynamic data, it is then possible to calculate the net mass of the polymer layer and thereby arrive at the number of surface associated polymers.

Table 3.1. Characteration of polymer coated nanoparticles based on density using AUC and DLS.

	S-value (S_V)	Hd (nm)	Density (g/cm^3)	Mass-polymer/NP (g)	Grafting Density (PEG/nm^2)
AuNP	586.3	9.9			
AuNP_1KPEG	418.1	13.9	4.9	1.37E-18	3.2
AuNP_2KPEG	337.4	17.5	3.0	1.67E-18	1.9
AuNP_5KPEG	225.4	25.3	1.6	2.39E-18	1.1
AuNP_10KPEG	170.2	34.6	1.3	3.51E-18	0.8
AuNP_20KPEG	138.5	79.9	1.0	9.41E-18	1.1

As an example, consider the 2K and 20K MWt PEG coated samples for 9.1 nm gold particles, which has a sedimentation coefficients of 586 ± 46 S_v. The 2K MWt PEG coated sample shown in figure 3.2A has a core diameter of 9.1 nm and a polymer thickness of 4.2 ± 0.4 nm (85.9% of the total volume). Using the overall particle density of 3.0 ± 0.3 gm/cm^3, this corresponds to a polymer mass of 1.7 E^{-18} ± 0.2 E^{-18} gm, and a grafting density of 1.9 ± 0.2 PEG/nm^2. In contrast the larger PEG MWt coating had a thickness of 35.5 ± 0.5 nm (99.9% of the total volume). The overall density of this particles 1.0 ± 0.0 gm/cm^3, this corresponds to a polymer mass of 9.4 E^{-18} ± 0.8 E^{-18} gm and a grafting density of 1.1± 0.0 PEG/nm^2.

The other approach used here to measure grafting density relies on changes in the sample composition as measured by total organic carbon, TOC, analysis. This method is in principle very similar to thermogravimetric analysis which measures the carbon in a solid powder from its combustion products; however, TOC measures in the solution phase and on small liquid samples, a single injection can use as little as 50 microliters. In solution, catalysts are used to promote organic carbon decomposition into CO_2 which is quantified to determine the total carbon in solution. Alternately, pretreating a sample with acid and purging with an inert gas the inorganic carbon is removed and the remaining carbon detected is the non-purgeable organic carbon (NPOC), this is used to measure the polymer carbon concentrations. Figure 3.2B shows that at equilibrium saturation (e.g. full coverage) the carbon concentrations increases with polymer chain length.

Converting the measured carbon concentrations from ppm carbon into the nanoparticle-polymer grafting densities is relatively straightforward. It requires an accurate measure of

nanoparticle concentration, derived here from absorbance data (see materials and methods section 2.2.3). The grafting density is then the ratio of available surface area (per volume) to the number of PEG molecules derived from the carbon concentration and the molecular weight of the PEG. As an illustration, a 9.0 nM solution of 2K MWt PEG-gold (9.1 nm d) had a carbon concentration of 9.4 ± 0.3 ppm and a corresponding grafting density of 2.5 ± 0.0 PEG/nm^2. The most significant source of systematic error is the underlying assumption that all measured carbon is derived from surface associated polymers. Careful sample purification ensures that this concern is minimal (See Chapter 2.1.2; purification).

Table 3.2. Characteration of polymer coated nanoparticles based on carbon content.

	TOC			TGA		
	ppm C	Mass-polymer/NP (g)	Grafting Density (PEG/nm^2)	% w/w C	Mass-polymer/NP (g)	Grafting Density (PEG/nm^2)
10 nm and 1K PEG	5.7	1.06E-18	5.0	11.2	6.7E-18	2.2
10 nm and 2K PEG	8.5	1.58E-18	2.5	20.9	1.4E-17	2.2
10 nm and 5K PEG	14.3	2.63E-18	3.7	40.5	3.6E-17	2.3
10 nm and 10K PEG	20.0	3.68E-18	1.7	42.3	3.9E-17	1.3
10 nm and 20K PEG	28.3	5.22E-18	1.2	47.0	4.7E-17	0.8

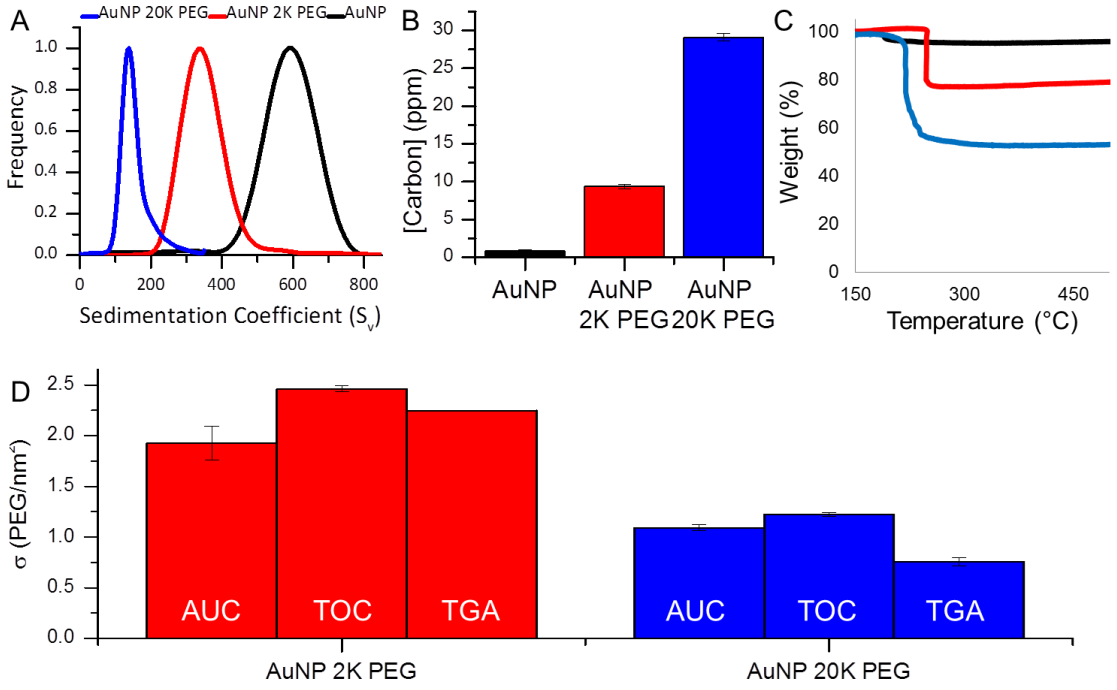

Figure 3.2 Effects of PEG coatings

Analysis of poly(ethylene) glycol coatings of 2K (red) and 20K (blue) on ~10nm inorganic gold nanoparticles. (A) AUC evaluations showed decreased sedimentation coefficient distributions with increased polymer molecular weight. The organic polymer adds carbon to the sample which raises the carbon concentration found using (B) total organic carbon analysis, and (C) increases the mass loss below 500°C determined via thermogravimetric analysis. (D) Each of these measurements can be used to quantify the polymer grafting densities. (Some error bars are not larger than the line).

3.3.2. Validation of methods

Finally, to validate both methods, we applied thermogravimetric analysis to powders derived from the nanoparticle solutions. This tool measures total carbon and is thus similar to the total organic carbon analysis, but it requires large amounts of solid material as opposed to liquid solutions. Figure 3.2C shows that the percent mass loss between 150

and 500 °C increases with surface functionalization and again with increased molecular weight of PEG. TGA is used extensively in nanotechnology for the evaluation of surface coatings on inorganic nanomaterials; data can provide information about whether a coating is present, as well as the grafting density and sample purity.[6,13,15,16,33,34] TGA analysis houses samples on precision balances in a furnace then the weight is collected as a function of temperature. For our samples the temperature was ramped from 150 to 1200 °C and all of the mass loss between 150 and 500 °C is attributed to the polymer. The weight percent of the polymer, from TGA and the core diameter of the particle, from TEM are used to determine the polymer grafting densities from TGA data, shown in calculation flow diagram 3. For the 2 K PEG coated gold, 20.8 ± 0.0% of the sample weight is polymer and has a resulting grafting density of 2.3 ± 0.0 PEG/nm^2. The largest systematic error for TGA is that oxidation of the inorganic materials can occur and result in an underestimation of the organic fraction of the materials.

Table 3.3 Nanoparticle and surface coverage and grafting density

	TOC		AUC		TGA	
	σ	Poly/NP	σ	Poly/NP	σ	Poly/NP
AuNP_1KPEG	5.0	638	3.2	827	2.2	508
AuNP_2KPEG	2.5	474	1.9	501	2.2	532
AuNP_5KPEG	3.7	317	1.1	288	2.3	548
AuNP_10KPEG	1.7	222	0.8	211	1.3	295
AuNP_20KPEG	1.2	157	1.1	283	0.8	179

This standard tool, TGA, provided a measure of polymer surface coverage that was in reasonable agreement, within 30 %, of the values found from both AUC and TOC (Figure 3.2D). (see table 1). The 2K nanoparticle-polymer conjugate had surface coverages of 2.2 PEG/nm^2 by TGA, which was in between the 2.5 and 1.9 PEG/nm^2 found from TOC

and AUC respectively. The longest polymer studied, 20,000 MWt, had grafting densities of 0.8 PEG/nm^2 as measured by TGA which was below the values found from TOC and AUC (1.2 and 1.1 PEG/nm^2 respectively). Interestingly, TGA provided carbon content consistently lower than the solution TOC methods. As noted above, by measuring carbon in solution (TOC) any impurities lead to a systematic error that increases the determined grafting densities; in contrast, during the analysis on TGA the flow of air can lead to oxidation of the inorganic core particles which would result in overestimating the inorganic content and underestimating the carbon content; yielding smaller grafting densities.

Also notable is the consistent agreement between the AUC and the TOC. The differences were most pronounced for the shorter polymer chains; the 2K sample for example, was found to have a grafting density of 1.9 from AUC as opposed to 2.5 from TOC. The grafting densities for the larger 20 K PEG, are within 0.2 PEG/nm^2 (1.0 to 1.2 PEG/nm^2). Aliquots from the same samples were run on both AUC and TOC to compare techniques over a wide range of polymer molecular weights and incomplete surface coverages (Figure 3.3). Five polymers coatings from 1K to 20K MWt on ~10 nm gold nanoparticles have grafting density values that deviate less than 38% between methods. In addition, samples with incomplete 2K PEG coating were prepared using PEG concentrations from 8.5 nM to 8.5 μM have coverage measurements by AUC and TOC with values that lie within 17% of each other. For all samples evaluate by both techniques there is an average difference of 20%.

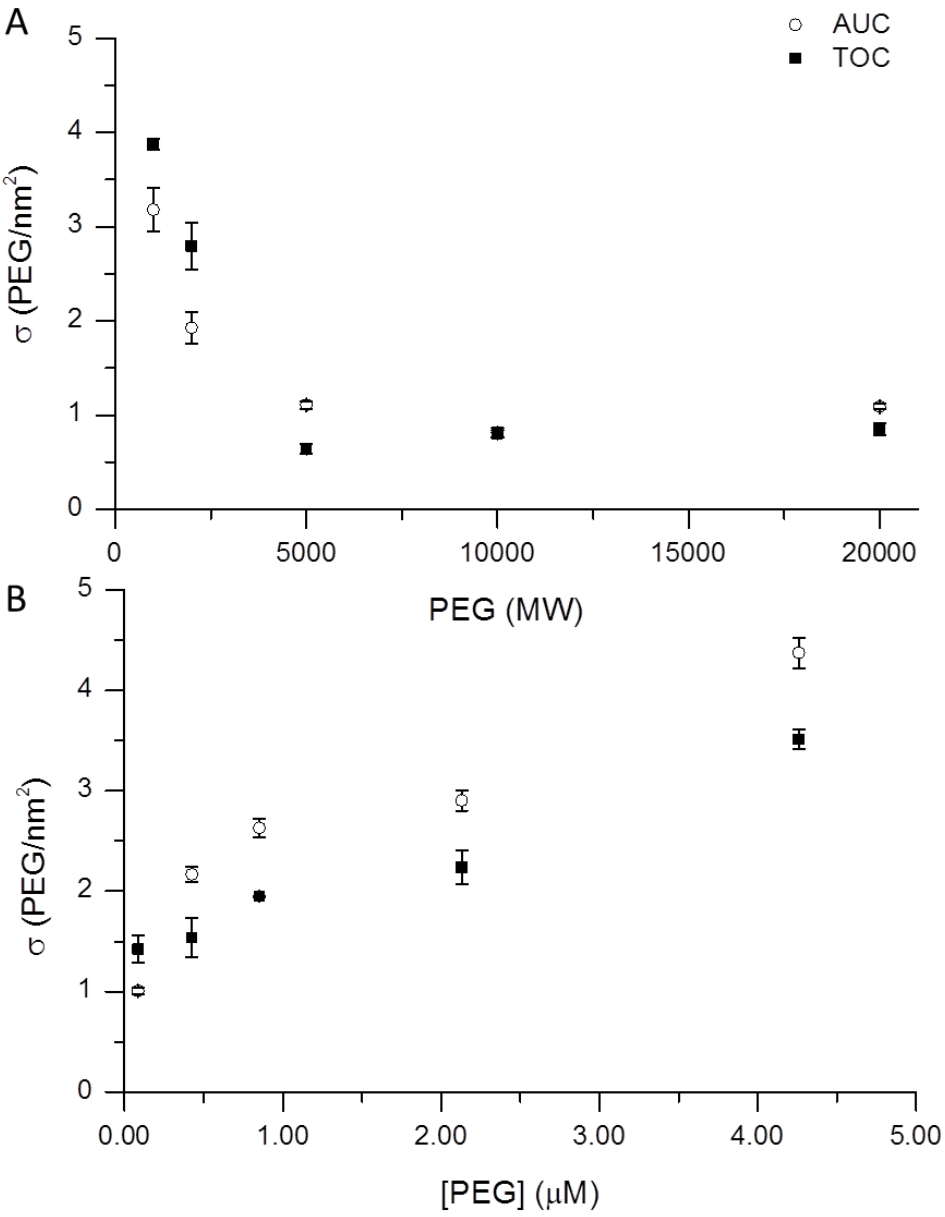

Figure 3.3. Grafting densities

All open squares are grafting densities values obtained using AUC and closed squares are values obtained from TOC data. Error bars represent measurements in triplicate for a single batch. Measurements of grafting density agree across surface coating of five different PEG molecular weights and increasing polymer concentrations within a 40% deviation for any given sample, with and average agreement of 20%.

3.3.3. Applications of the measurement of surface polymer coverage

These measurements make it possible to study how the surface associated polymer concentration varies with the amount of added solution polymer. Current quantitative analytical methods to determine grafting density are not sensitive enough to evaluate the polymer surface coverage on nanoparticles below saturation. Figure 3.4 shows the systematic increase and eventual plateau in grafting densities as a function of initial polymer concentration from 8.5 nM to 8.5 μM for 2K and 20K PEG-SH coated gold nanoparticles. Either method showed sensitivity in determining the grafting density with changes in polymer concentration less than 10%. Surface saturation concentrations for 2K and 20K PEG were determined to be around 4 μM and 3 μM PEG for the samples, respectively. These saturation concentrations are at coverages of 500 and 370 PEG/particle, respectively.

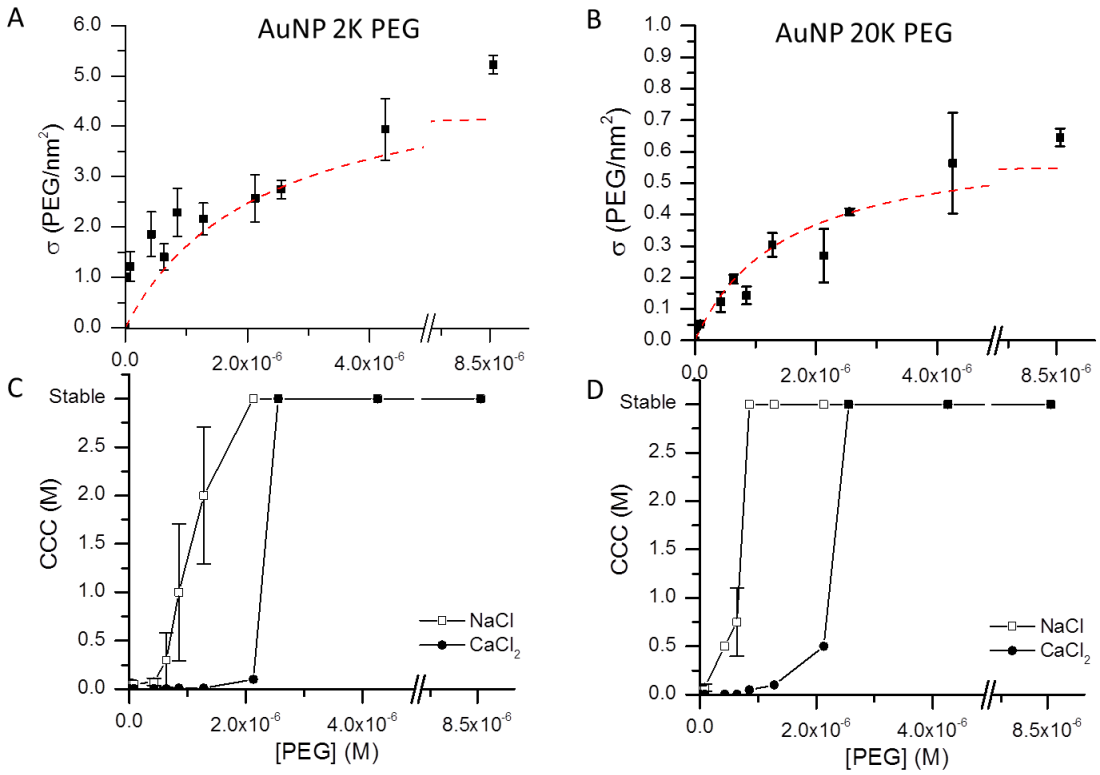

Figure 3.4. Change in Grafting Density

The change in grafting density upon the addition of (A) 2 K or (B) 20 K PEG to a solution of ~10 nm gold nanoparticles (red dotted lines are added to guide the eye). The critical coagulation concentrations (CCC) of the (A) 2K and (B) 20K coated particles were determined with sodium chloride and calcium chloride.

Figure 3.4 also presents colloidal stability data for particles as measured through their aggregation in the presence of various salts. The minimum NaCl or $CaCl_2$ concentration that result in the aggregation of the particles is known as the critical coagulation concentration (CCC). This test has been applied frequently as an indirect measure of the effective surface coating of particles by associating stability in a salt solution with the

full, equilibrium saturation of a particle.[1] We evaluated critically this assumption using independent measures of the surface coverage.

Apparent in Figure 3.4 is that particles can be rendered stable in solution even while their polymer surface coverage is not fully at equilibrium. For example, CCC evaluations in NaCl find a stable sample at polymer concentrations of 2.1 and 0.85 μM PEG (300 and 100 PEG/particle) for the 2 K PEG and 20 K PEG samples, respectively. This should be the concentration where the polymer effectively blocks the surface charge inherent on as synthesised gold nanoparticles. However, measurements by zeta potential found that slightly lower polymer concentrations of 1.3 μM (150 PEG/particle) 2K PEG and only 0.6 μM (75 PEG/particle) 20K PEG neutralize the surface charge. By contrast, neither surface coating material has a resistance to aggregation in the divalent, $CaCl_2$, solutions at low PEG concentrations and it is not until 2.6 μM PEG (300 PEG/ particle) concentration do the particles become stable in the divalent solution. Interestingly, this concentration (2.6 μM) is close to the polymer concentrations needed to reach surface saturation for both PEG chain lengths (4 μM and 3 μM). These results suggest that the evaluation of the completeness of a surface coating is not accurately assessed through the stability in monovalent salt solutions or by the loss of effective surface charge. The most effective tests for surface saturation are measurements of polymer grafting density or alternatively, through flocculation in a divalent salt solution.

Measurements in the grafting densities also reveal interesting trends in polymer packing around nanoparticles. Most notably is the fact that polymer conformation can be very different depending on the polymer chain length. Saturated grafting densities

measurements for five polymers, from 1K to 20K, on seven particle diameters, from 8 to 27 nm**.** Figure 5A shows, that as expected, grafting densities determined by AUC decrease as polymer molecular weight increase for all diameters of nanoparticles tested. This means that the shorter molecular weight PEG molecules occupy less surface area and can pack more efficiently than the larger molecular weight polymers. Furthermore, the shortest polymer chain length has an increased packing efficiency with increased nanoparticle diameter. As the nanoparticle diameter increases from 8 nm to 27 nm there is a corresponding increase in grafting density from 2.5 to 14.9 PEG/nm^2 for 1K PEG.

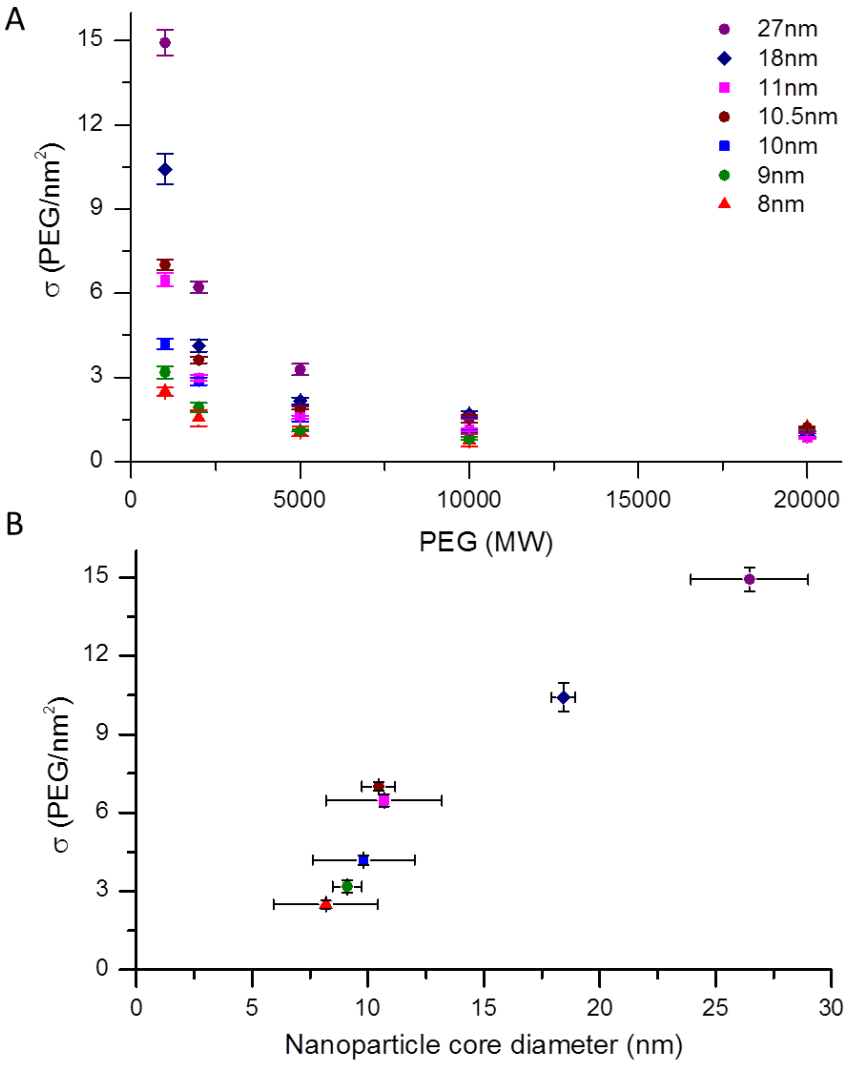

Figure 3.5. AUC analysis of PEG coverages

AUC analysis of PEG coverages on various nanoparticle sizes. Particles from 8 nm to 27 nm, were evaluated with 1K, 2K, 5K, 10K and 20K PEG coverages showing that the polymer grafting densities decrease as polymer molecular weight increases for all sizes. In addition there is an increase in packing efficiency for the 1K low molecular weight PEG molecules as the particle diameter increases. X error bars depict the measured size distribution. (Most error bars are not larger than their corresponding data points)

3.3.4. Comparison of analytical methods

This work presents two options for solution-based assays that can easily and reproducibly measure the polymer coverages of nanoparticle-polymer conjugates directly in aqueous solutions. Both AUC and TOC are performed in the native solutions and use less than 1 mL (< 60 μg) of sample for a triplicate evaluation and thus have a distinct advantage as compared to the sample intensive TGA methodology (See table 3.4 below). AUC has the advantage that it can be applied to variety of surface functionalized materials even in non-aqueous solvents. It is also insensitive to the presence of carbon-containing impurities. While in this work DLS was required as an independent measure of hydrodynamic diameter, we note that using 2D velocity sedimentation analysis it may be possible to get both the sedimentation coefficient and hydrodynamic diameter in one scan.[35] However, the instrumentation is more specialized and data analysis can be difficult. TOC, on the other hand, is a simple bench top instrument with easy sample preparation and data analysis, and thus more likely to be adopted in routine laboratory use. Another possible benefit of the TOC is that it can be fitted with a total nitrogen module for simultaneous quantification of carbon and nitrogen which would be valuable for analysis of surface coating materials with amine functionalization groups. However, TOC can be prone to overestimating the surface coverages if solutions are not carefully purified.

Table 3.4. Comparison of techniques.

Technique	Sample size	Reusable	Prior knowledge of the polymer	Prior knowledge of the nanoparticle
AUC	0.4 mL	Yes	PEG MW	None
TOC	0.2 mL	No	PEG MW	Concentration, diameter
TGA	8.6 mL	No	PEG MW	Density, diameter

3.4. CONCLUSION

In summary, we have determined that analytical ultracentrifugation and total organic carbon analysis are effective methods for obtaining the polymer grafting densities of nanoparticle-polymer conjugates directly in solution. Both techniques were used to evaluate a range of gold nanoparticle diameters coated with various molecular weights of thiol functionalized poly(ethylene glycol). Dilute (~10 nM) samples of less than 1 mL were analyzed for polymer surface coverage; not only did each method independently agree, but their reported values were consistent with those derived from thermogravimetric analysis of the carbon content of recovered powders. AUC is best suited for samples with dense and uniform core nanoparticles, and may be applied to nanoparticles in any kind of solvent. It does require a specialized instrument capable of relatively intensive data analysis for extracting sedimentation coefficients. Measures of total organic carbon use a benchtop and simple instrument and are clearly superior for aqueous suspensions that have been carefully purified. These approaches to measuring the polymer surface coverage of nanoparticle-polymer conjugates offers many advantages to researchers. These include quality control methods to ensure batch to

batch consistency, as well as quantitative assessments of the role of surface coverage on engineered material's stability and transport in biological or environmental matrices.

3.5. REFERENCES

(1) Liu, Y.; Shipton, M. K.; Ryan, J.; Kaufman, E. D.; Franzen, S.; Feldheim, D. L. *Analytical Chemistry* **2007**, *79*, 2221.

(2) Mosqueira, V. C. F.; Legrand, P.; Morgat, J.-L.; Vert, M.; Mysiakine, E.; Gref, R.; Devissaguet, J.-P.; Barratt, G. *Pharmaceutical Research* **2001**, *18*, 1411.

(3) Jiemvarangkul, P.; Zhang, W.-x.; Lien, H.-L. *Chemical Engineering Journal* **2011**, *170*, 482.

(4) Darlington, T. K.; Neigh, A. M.; Spencer, M. T.; Guyen, O. T. N.; Oldenburg, S. J. *Environmental Toxicology and Chemistry* **2009**, *28*, 1191.

(5) Feng, W.; Brash, J. L.; Zhu, S. *Biomaterials* **2006**, *27*, 847.

(6) Corbierre, M. K.; Cameron, N. S.; Sutton, M.; Laaziri, K.; Lennox, R. B. *Langmuir* **2005**, *21*, 6063.

(7) Gessner, A., Paulke, B.R., Muller, R.H., Goppert, T.M. *Die Pharmazie* **2006**, *61*, 293.

(8) Jokerst, J. V.; Lobovkina, T.; Zare, R. N.; Gambhir, S. S. *Nanomedicine* **2011**, *6*, 715.

(9) Aggarwal, P.; Hall, J. B.; McLeland, C. B.; Dobrovolskaia, M. A.; McNeil, S. E. *Advanced Drug Delivery Reviews* **2009**, *61*, 428.

(10) Kingshott, P.; Thissen, H.; Griesser, H. J. *Biomaterials* **2002**, *23*, 2043.

(11) Takae, S.; Akiyama, Y.; Otsuka, H.; Nakamura, T.; Nagasaki, Y.; Kataoka, K. *Biomacromolecules* **2005**, *6*, 818.

(12) Choi, C. H. J.; Zuckerman, J. E.; Webster, P.; Davis, M. E. *Proceedings of the National Academy of Sciences* **2011**, *108*, 6656.

(13) Maccarini, M.; Briganti, G.; Rucareanu, S.; Lui, X.-D.; Sinibaldi, R.; Sztucki, M.; Lennox, R. B. *The Journal of Physical Chemistry C* **2010**, *114*, 6937.

(14) Zhu, X.; Su, N.; Li, H.; Liu, X.; Li, Y. *Materials Letters* **2011**, *65*, 2816.

(15) Corbierre, M. K.; Cameron, N. S.; Lennox, R. B. *Langmuir* **2004**, *20*, 2867.

(16) Mansfield, E.; Kar, A.; Quinn, T. P.; Hooker, S. A. *Analytical Chemistry* **2010**, *82*, 9977.

(17) Sofia, S. J.; Premnath, V.; Merrill, E. W. *Macromolecules* **1998**, *31*, 5059.

(18) Garcia-Fuentes, M.; Torres, D.; Martín-Pastor, M.; Alonso, M. J. *Langmuir* **2004**, *20*, 8839.

(19) Liu, Q.; de Wijn, J. R.; de Groot, K.; van Blitterswijk, C. A. *Biomaterials* **1998**, *19*, 1067.

(20) Castelino, K.; Kannan, B.; Majumdar, A. *Langmuir* **2005**, *21*, 1956.

(21) Demers, L. M.; Mirkin, C. A.; Mucic, R. C.; Reynolds, R. A.; Letsinger, R. L.; Elghanian, R.; Viswanadham, G. *Analytical Chemistry* **2000**, *72*, 5535.

(22) Liu, X.; Atwater, M.; Wang, J.; Huo, Q. *Colloids and Surfaces B: Biointerfaces* **2007**, *58*, 3.

(23) Laue, T. M.; Stafford III, W. F. *Annual Review of Biophysics and Biomolecular Structure* **1999**, *28*, 75.

(24) Lebowitz, J.; Lewis, M. S.; Schuck, P. *Protein Science* **2002**, *11*, 2067.

(25) Calabretta, M. K.; Matthews, K. S.; Colvin, V. L. *Bioconjugate Chemistry* **2006**, *17*, 1156.

(26) Jamison, J. A.; Krueger, K. M.; Mayo, J. T.; Yavuz, C. T.; Redden, J. J.; Colvin, V. L. *Nanotechnology* **2009**, *20*, 355702.

(27) Jamison, J. A.; Krueger, K. M.; Yavuz, C. T.; Mayo, J. T.; LeCrone, D.; Redden, J. J.; Colvin, V. L. *ACS Nano* **2008**, *2*, 311.

(28) Falabella, J. B.; Cho, T. J.; Ripple, D. C.; Hackley, V. A.; Tarlov, M. J. *Langmuir* **2010**, *26*, 12740.

(29) Cölfen, H.; Tirosh, S.; Zaban, A. *Langmuir* **2003**, *19*, 10654.

(30) Calabretta, M.; Jamison, J. A.; Falkner, J. C.; Liu, Y.; Yuhas, B. D.; Matthews, K. S.; Colvin, V. L. *Nano Letters* **2005**, *5*, 963.

(31) Arnold, M. S.; Suntivich, J.; Stupp, S. I.; Hersam, M. C. *ACS Nano* **2008**, *2*, 2291.

(32) Backes, C.; Karabudak , E.; Schmidt, C. D.; Hauke, F.; Hirsch, A.; Wohlleben, W. *Chemistry – A European Journal* **2010**, *16*, 13176.

(33) Mukherjee, P.; Bhattacharya, R.; Bone, N.; Lee, Y.; Patra, C.; Wang, S.; Lu, L.; Secreto, C.; Banerjee, P.; Yaszemski, M.; Kay, N.; Mukhopadhyay, D. *Journal of Nanobiotechnology* **2007**, *5*, 4.

(34) Pang, L. S. K.; Saxby, J. D.; Chatfield, S. P. *The Journal of Physical Chemistry* **1993**, *97*, 6941.

(35) Carney, R. P.; Kim, J. Y.; Qian, H.; Jin, R.; Mehenni, H.; Stellacci, F.; Bakr, O. M. *Nat Commun* **2011**, *2*, 335.

Chapter 4

NANOPARTICLE-POLYMER CONJUGATES AS NUCLEANTS FOR PROTEIN CRYSTALLIZATION

Nanoparticles possess many properties which suggest they could be appropriate nucleation sites for protein crystals. They can be appropriately stabilized to interact either strongly or weakly with individual proteins, and could thus act as heterogeneous nucleants for crystallization. To evaluate this hypothesis, polymer–nanoparticle conjugates (thiol functionalized poly(ethylene glycol) (HS-PEG) on gold) were used in protein crystallization studies. The PEG coatings provided steric stability to the nanoparticles and allowed them to remain individually dispersed even in the high ionic

*Work performed within this chapter has been done in collaboration with members from Dr. Shamoo's lab. All training and support for crystallization methods were provided by Kasia Walkiewicz, and Dr. Milya G. Davlieva. They also ran and process the single crystal diffraction data and programed and ran the high throughput robot. In addition I had a lot of help from interns in the Colvin lab: Ajoke Williams (development of crystallization kinetics methods), Gustavo Resendiz (crystallization of proteins other than lysozyme), Raymond Verm (method development work for kinetics and dialysis equilibrium studies), Michael Lilierose (nanoparticle stability and dialysis studies), and Naushaba Ali (nanoparticle characterization and equilibrium dialysis studies).

strength of the crystallization growth medium. The polymer coatings also served to mediate the strength of interaction between the nanoparticles and the proteins. Shorter chain poly(ethylene) glycol effectively blocked all protein interactions. Longer chain polymers, with molecular weights larger than 5,000, were able to weakly associate with proteins. Crystal formation in the presence of these nanoparticle-polymer conjugates was notably faster for a diverse set of proteins, such as ferritin, human serum albumin, lipase B, xylanase, glucose isomerase and lysozyme. In all cases the nanoparticle nucleants decreased the time to nucleation, expanded the range of appropriate crystallization conditions, and increased the success rate for producing crystals and pre-crystalline materials in high through-put crystallization.

4.1. INTRODUCTION

The identification of protein structure remains central to the study of both biology and medicine. When biomedical researchers have the full tertiary structure of a protein it is possible to design molecular drugs for precise interactions with active sites within the protein, this is called structure based design. Additionally, our exanded understanding of genetics brought about by the human genome project has made it clear that a full understanding of systems biology requires better and faster methods to characterize even greater numbers of proteins and their modifications – now a task for the Human Proteome Project.[1,2]

A significant barrier faced in these areas is the rapid and reliable analysis of protein structure – a process that requires protein crystallization followed by x-ray

crystallography. While thousands of proteins have been analyzed in this fashion, there are many thousands more that lack successful crystallization protocols.[3,4] Researchers have traditionally used trial and error to develop conditions that lead to a protein's crystallization, but this approach is slow, only modestly successful and dependent on large quantities of pure protein.[1] Recently, high-throughput and automated screening methods have vastly expanded the speed and consequently the number of crystallization conditions that can be evaluated. However, the success rate for these high-throughput methods, termed the 'hit rate', remains low and for many systems can require months of development.[1-6] In many cases protein and protein-ligand complexes of great importance remain unsolved even after years of decades of effort.

As a result of these challenges, there has been a longstanding interest in the development of nucleating agents for protein crystallization. Protein crystals usually form in solutions that are just barely supersaturated;[2] in this way, crystals develop slowly and with more perfection providing substrates better suited for x-ray crystallography.[2,7,8] However, entropic barriers to crystallization under such conditions are substantial. Proteins are large dynamic molecules and they often possess many possible conformations that determine protein-protein associations. As a result, the time to nucleation of protein crystals – referred to commonly as the induction time – can be in excess of one month. By incorporating a nucleation agent, generally referred to by the protein crystallization community as a nucleants, the hope is to drastically reduce the induction time to nucleation.

While many interesting materials have been found to induce nucleation for some proteins, the goal of a ‘‘universal nucleant’’ for protein crystallization remains elusive.[2,9] Early protein crystallographers relied on solid substrates such as horse hair and seaweed to induce nucleation or proteins; more recently porous substrates and bioglass have become a focal point.[2,9,10] In all of these cases the nucleants are macroscopic materials and therefore not easy to introduce into current high-throughput crystallization instrumentation as they have to individually placed in each well for evaluation.

While solid materials, nanoparticles can be stabilized in aqueous suspensions and incorporated directly into the protein stock solution. Two previous studies have evaluated gold nanoparticles and polystyrene nanospheres in crystallization strategies for multiple proteins. However, these nanoparticles quickly aggregated due to the screening of their surface charges, and it is likely that the proteins nucleated on the surfaces of larger aggregates of nanoparticles.[9,10] An outstanding question is whether nanoparticles that are colloidally stable in crystal growth media, effectively acting as isolated materials, could induce protein crystal nucleation.[5]

Here we show that sterically stabilized polymer – nanoparticle conjugates (AuNP_PEG) are stable in crystal growth media and that they promote the nucleation of many different proteins. This effect is very sensitive to the polymer surface structure which is defined by its surface coverage and molecular weight. Shorter polymer chains (2,000 molecular weight) extend around a nanoparticle and have very high surface coverages (e.g. 1.9 PEG chains/nm^2) while longer polymer chains (20,000 molecular weight) will mushroom and have lower net surface coverage (e.g. 1.1 PEG chains/nm^2). As discussed in Chapter 3,

it is the longer polymer chains that have the most protein association, and as shown in this Chapter the biggest impact on protein nucleation. For example, 10 nm gold nanoparticles coated with longer polymers decreased the time to nucleation for lysozyme by a factor of seven, increased the hit rates for crystal formation in high-throughput screens, and allowed for protein crystallization below supersolubility conditions with 10 million proteins per particle.

In this Chapter we present the impact of polymer-nanoparticle conjugate incorporation into the protein stock solutions used in existing high-throughput screening techniques. Two concentrations of gold nanoparticle-polymer conjugates, 1 and 10 nM, were added to protein stock solutions for ferritin, human serum albumin, lipase B, xylanase, glucose isomerase and lysozyme. The effects were characterized and evaluated based on results from two sets of 96 screening conditions for a total of 192 unique preparations. With nanoparticles the number of conditions that produce crystals increased on average for all proteins by a factor of five (1 nM) and a factor of seven (10 nM). Moreover, nanoparticle additions reduced the occurrence of unfavorable protein aggregation in many cases. Finally, adding nanoparticle nucleants to the lysozyme protein crystallization screens resulted in crystal formation in 26 conditions that without the nanoparticles had no crystals.

4.2. MATERIALS AND METHODS

4.2.1. Nanoparticle preparation, characterization and purification

(see Chapter 2.1.1.-2.1.2.)

4.2.2. Protein stock solutions:

Pure protein samples of lysozyme, ferritin, human serum albumin (HSA), (Sigma Aldrich) lipase B, xylanase, and glucose isomerase (Hampton Research) were prepared in buffered solutions where the protein concentration, buffer material, ionic strength and pH were determined from literature or from recommendations from the vendor. Concentrations were determined spectroscopically at 280 nm. Solution concentration were as follows: Lysozyme (50mg/mL), ferritin (30 mg/mL), HSA (10mg/mL), lipase B (35 mg/mL), xylanase (18 mg/mL), glucose isomerase (10 mg/mL). For more information about the protein stock solution preparations see Chapter 2.3.2)

4.2.3. Crystallization:

Hanging drop, batch method and high-throughput crystallization methods were used as previously described (Chapter 2.3.3 Protein crystallization methods).

4.2.4. Kinetics of crystal formation:

The method to determine the kinetics of crystal formation was adapted from previous literature on lysozyme crystallization.[11] Briefly, the protein and AuNP concentrations were monitored in real time during crystallization (from 1 – 5 days) to determine time to

nucleation (T_{nuc}), and concentration of materials in solution and in the crystal. For more information about this process, please see Chapter 2, section 2.4.1, kinetics of crystal formation.

4.2.5. Phase maps:

Phase maps are used to determine the solubility region of a protein around a crystallizing condition to optimize the crystal formation. (See chapter 2.4.2)

4.3. RESULTS AND DISCUSSION

4.3.1. Forming sterically stabilized polymer-nanoparticle conjugates

Polymer – nanoparticle nucleants were prepared by conjugating poly(ethylene glycol) to gold colloid. The red colored solution in Figure 4.1, displays the characteristic 523 nm peak optical absorbance spectrum expected from the 12 nm gold nanoparticles shown in the transmission electron microscopy image. As produced gold nanoparticles are coated with a layer of negatively charged citrate molecules which keep particles isolated in solution due to repulsive forces. However, these particles will quickly aggregate when ions are present in solution. Counter positive ions are attracted to the negative surface and in turn will attract more negative ions until there is a complete destabilization of the charge barrier that kept the particles isolated and they will begin to aggregate. The increase in particle size due to aggregation causes the peak optical absorbance of the sample to shift towards longer wavelengths, causing the once red solution to shift to a purple color which provides visual indication that the particles are unstable.[12,13] To make

sure this doesn't happen for the nanoparticle nucleants of interest in this Chapter, surface modification strategies are used to impart steric stability (as opposed to charge stability) to nanoparticles.[14,15]

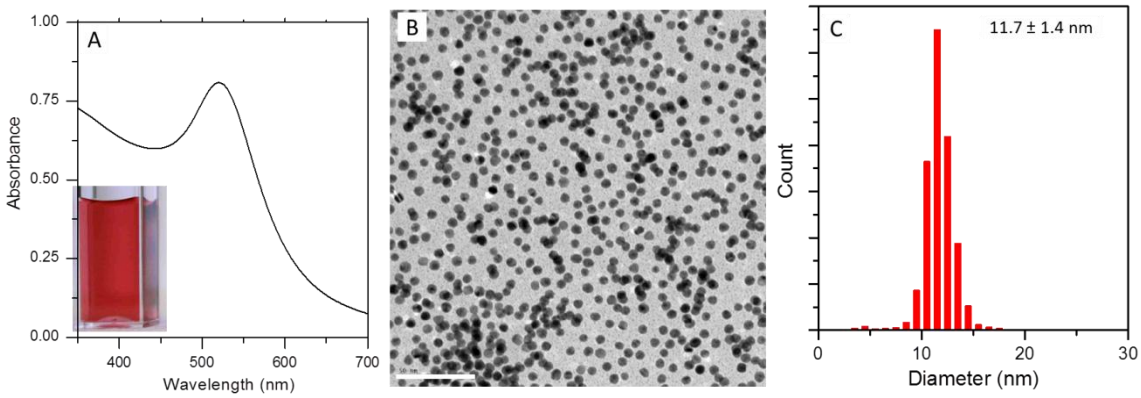

Figure 4.1. Gold nanoparticles.

(A) Gold nanoparticle solutions are characteristically red due to a strong optical absorbance peak in the visible region of the spectrum of light, centered at 520 nm. (B) Transmission electron microscopy image for the near spherical gold nanoparticles. (C) Histogram showing the size and distribution of 11.7 ± 1.4 nm.

Figure 4.2A shows the polymer grafting scheme used in this work. Thiol functionalized poly(ethylene glycol) (HS-PEG) exposed to gold nanoparticles in water binds to the surface via the strong gold-sulfur bond. The polymer layer depicted on the nanoparticle surface in Figure 4.2 is represented as an extended brush conformation; however based on surface coverage and molecular the polymer could assume either an extended brush (high coverage, low MWt) or a partially coiled mushroom (low coverage, high MWt) conformation. The polymer coating prevents aggregation through steric effects. Figure 4.2B&C show that PEG coated nanoparticles are more resistant to aggregation in high

ionic strength salt solutions. At the conditions used for lysozyme crystallization, 1 M NaCl, the uncoated particles are aggregated, while the PEG stabilized sample remains disperse in solution.

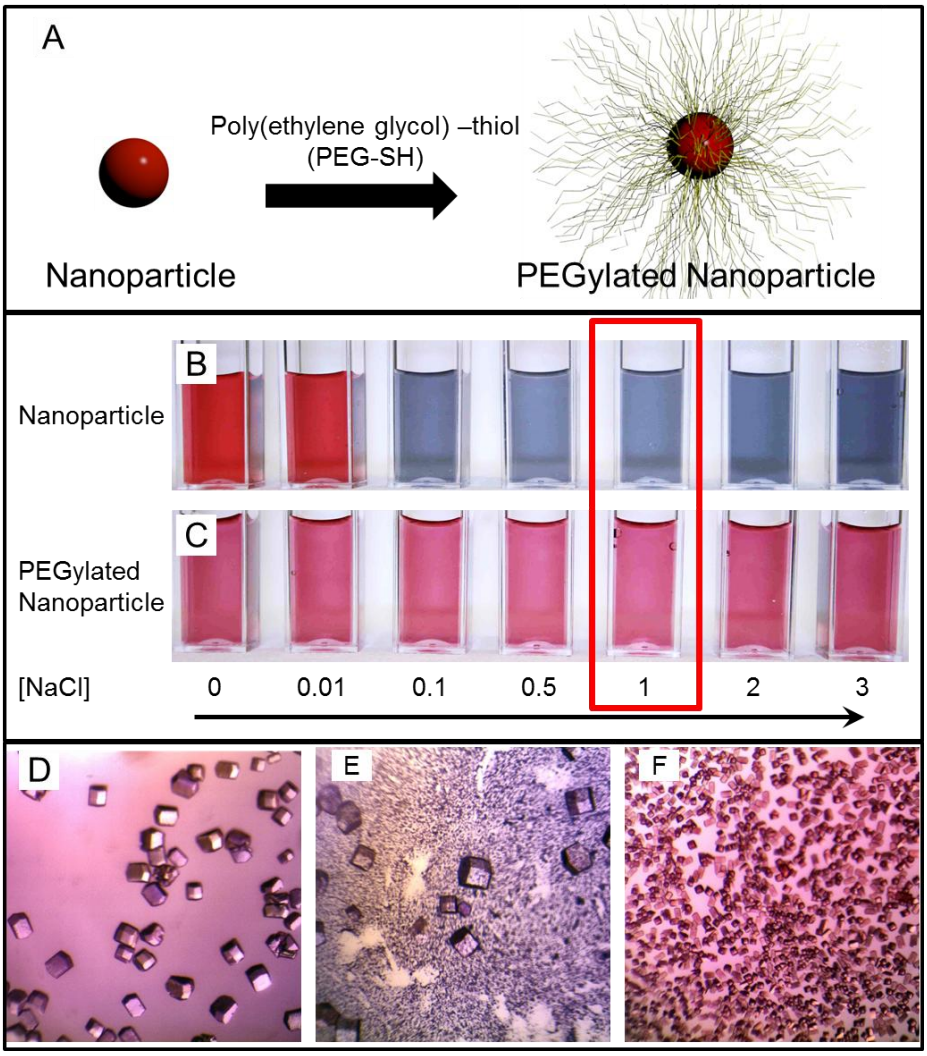

Figure 4.2. Sterrically stabilized nanoparticles in lysozyme crystallization.

(A) Gold nanoparticles coated with thiol functionalized poly(ethylene glycol) create polymer – nanoparticle conjugate nucleants. PEG layers provide steric stabilization. (B) Uncoated nanoparticles aggregate at low concentrations of salt in solution, while (C) PEG coated nanoparticle are disperse in solution even at salt concentrations of 3M (red box represents crystallization conditions 1M). Crystals produced for (D) a control protein sample, (E) with charge stablized particles, and (F) with PEGylated nanoparticles.

4.3.2. Nanoparticle-polymer conjugates act as nucleating agents for lysozyme crystallization

Microscope images of the crystals that form for samples without nanoparticles, with uncoated, and with PEG coated gold nanoparticles (Figure 4.2D-F) illustrate the similarity in the size and number of crystals formed with aggregated nanoparticles and in the control sample. The purple residue covering the bottom of the reservoir in image 2E are nanoparticle aggregates that sedimented out of solution due to their large size. Other groups have reported that gold and silica nanoparticles in crystal growth media lead to changes in the nucleation of protein crystallization.[9,10] However, the effects may be attributed to the aggregates formed from these nanomaterials, similar to other macroscopic materials with rough, irregular surfaces such as horse hair, bioglass, dust and seaweed which are known to have nucleation effects.[16]

The sterically stabilized nanoparticles (Figure 4.2, right) have very different effects on protein crystallization. By engineering the polymer – nanoparticle conjugates to remain disperse throughout the crystallization solution, nucleation effects can take place in a homogeneous fashion throughout the medium. As a result of many more nucleation sites, more net crystals are formed and since the available protein gets used equally by all sites, the final crystal sizes are smaller. These features are clear indications that the sterically stabilized gold nanoparticles are able to nucleate the crystallization of lysozyme.

We explored whether the nucleation effects in Figure 4.2 depended on the polymer surface coating; Figure 4.3 shows that not all sterically stabilized nanoparticles induced

crystal formation. Only longer polymer coatings (>5K) can produce higher quantities of smaller crystals in a shorter amount of time. Polymer – nanoparticle conjugates prepared with a range of PEG molecular weights from 1K to 30K were evaluated; in each case, solutions were red once added to the crystal growth media indicating a preservation of the steric stabilization of the PEG coatings. The shorter poly(ethylene) glycol, of 1,000 and 2,000 molecular weight, formed nanoparticle conjugates with little effect on the crystallization process. The resulting lysozyme crystals were similar in size, count and time to nucleation (T_{nuc}) as the control protein crystals (Table 4.1). Larger molecular weight polymers (more than 5,000 molecular weight) lead to a consistent set of nucleation effects: smaller and more numerous crystals, and faster nucleation. Clearly, once the polymer chain lengths are long enough the nanoparticle-polymer conjugates are able to induce nucleation of the proteins.

Table 4.1. PEG MWt dependent lysozyme crystallizaiton nucleation effects.

	Crystal size μm	**Crystal count** number	**T_{nuc}** hours
Control	142.2	17	3.4
AuNP_1K PEG	139.3	16	2.1
AuNP_2K PEG	128.9	22	1.0
AuNP_5K PEG	109.7	29	0.6
AuNP_10K PEG	97.8	59	0.2
AuNP_20K PEG	69.2	220	0.1
AuNP_30K PEG	*	1284	0.1

* AuNP_30K PEG crystals were too small to detect distinct edges.

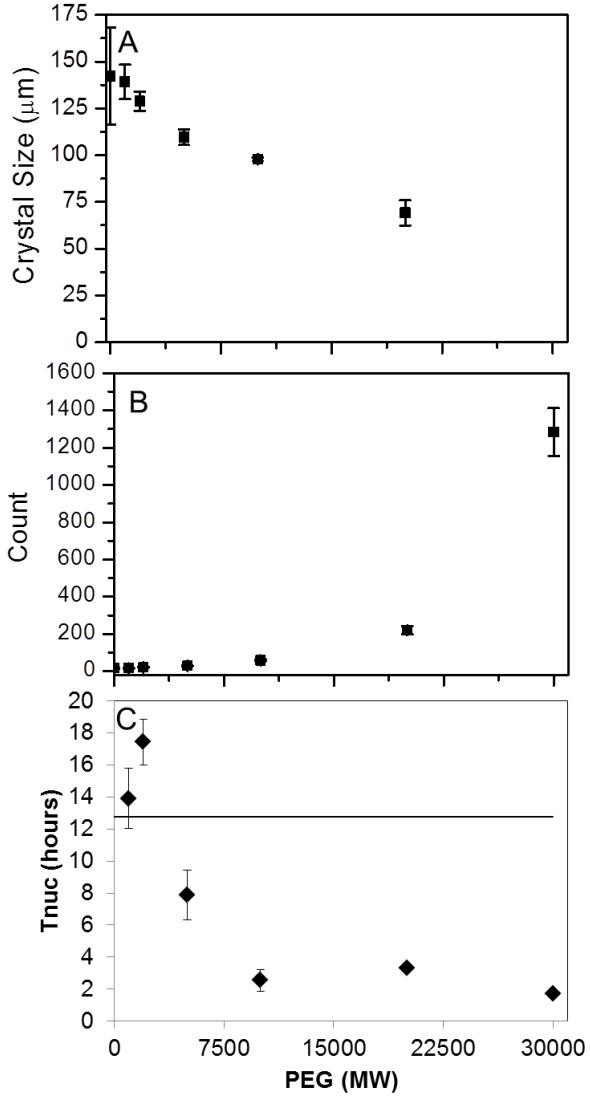

Figure 4.3. PEG molecular weight dependence on lysozyme nuclation.

Molecular weight of the polymer surface coating affects the nucleation properties of the polymer – nanoparticle conjugates. Larger molecular weight PEG (A) decreases the crystal size, (B) increase the number of crystals produced and (C) decreases the time to nucleation.

4.3.3. Ruling out the influence of free polymer on nanonucleant effects

The interpretation of the data in Figure 4.3 is complicated by the possibility that free polymer, rather than surface associated polymer, is affecting protein crystallization. Poly(ethylene) glycol is also a known additive for protein crystallization which is thought to increase nucleation events through excluded volume effects.[17,18] It is typically used in concentrations (e.g. 0.5-10 w/w%) significantly higher than the nanomolar concentration of nanoparticle-polymer conjugates. Still, in nanoparticle suspensions there may be some level of unbound polymer in equilibrium with the surface associated material as well as excess left behind from the surface conjugation reaction.

To evaluate the influence of any free polymer, we compared the nucleation properties of sterically stabilized samples with varying levels of purification. Three rounds of spin-filtration (100 MWCO) are usually sufficient to remove any unbound impurities from nanoparticle suspensions: for some samples an additional three rounds of centrifugation followed by redispersal was employed. The concentration of free PEG in solution was estimated based on the concentration of PEG within the supernatant determined via total carbon analyzer (see Chapter 3). Figure 4.4A shows the free PEG concentration of 20,000 molecular weight PEG at various times during the purification process. The original nanoparticle solution was prepared to contain 280 μmolar 20K PEG (0.6 w/w%); after spin filtration, the concentration of PEG not bound to a surface was ~28 μmolar (0.06 w/w%). Centrifugation further cleaned the sample and provided a 290 nmolar

(0.0001 w/w%) concentration of free PEG. In this way, samples with sub-millimolar levels of free PEG could be produced and compared in their crystallization behavior.

We found that the time to nucleation was not substantially impacted by the purification processes even though the amount of free polymer in the suspensions was varied by orders of magnitude. For example, samples purified via spin filtration had average nucleation times of 3.6 ± 0.5 hours while more highly pure materials had similar nucleation times, 3.3 ± 0.3 hours. While the removal of free PEG from solution didn't alter the time to nucleation it did change the morphology of the crystals. The images in Figure 4.4B show the crystals formed in the presence of micromolar free PEG were elongated with a higher aspect ratio while those formed in the more purified sample were cuboidal. The size scale of the crystals remained similar; each had an average width between 60 and 70 μm.

We also investigated the impact of very small PEG concentrations alone on the nucleation of protein crystals; the existing literature generally only covered highly concentrated PEG suspensions.[18,19] Lysozyme crystals were formed without nanoparticles but with 6000 molecular weight PEG at concentrations from 0 to 25 μmolar. Figure 4.4C shows the resulting protein crystals and shows that crystal elongation occurs with increasing polymer. However, the crystal count and net volume remain the same, in these solutions.

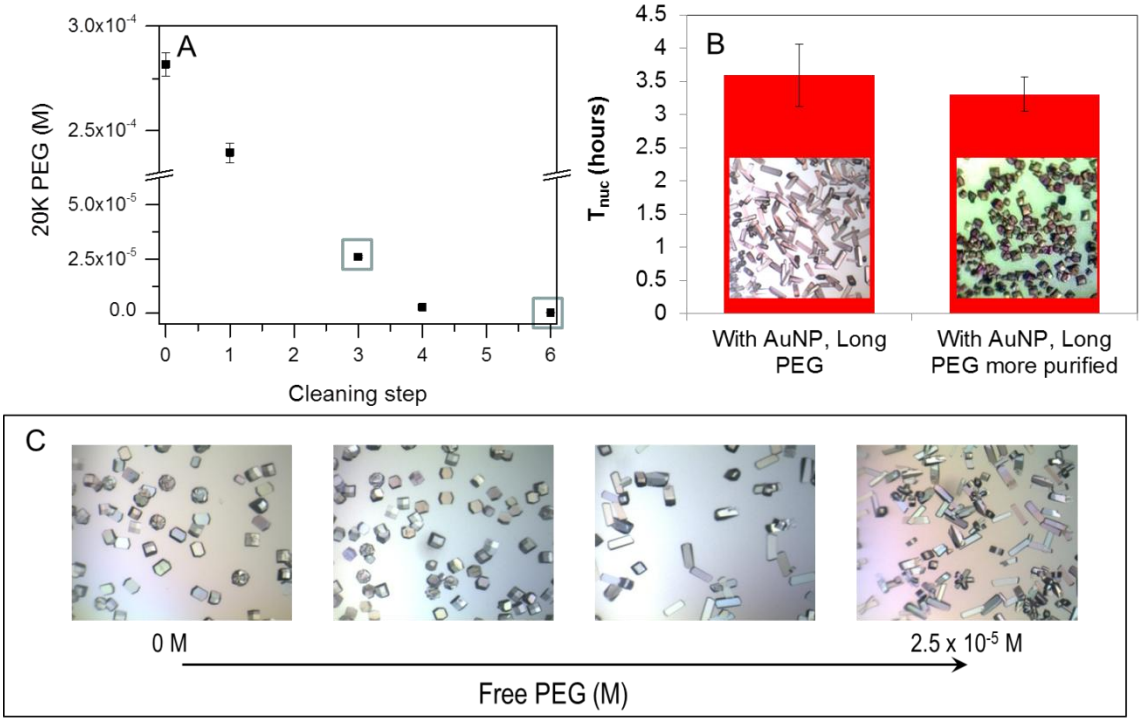

Figure 4.4. Free PEG on protein crystallization.

(A) The concentration of free 20KPEG in solution during cleaning steps 1 – 6; steps 1-3 were spin filtered samples using 100 MWCO filters at 4150 RPM for 15 minutes, steps 4-6 were centrifugation at 11,500 RPM for 99 minutes. (B) Time to nucleation and images of lysozyme crystals with AuNP_20KPEG after purifications steps 1-3 (AuNP, Long PEG) and after 1-6 (AuNP, Long PEG more purified). (C) Lysozyme crystallized in the presence of increasing concentrations of free PEG from 0 to 2.5x10 $^{-5}$M.

4.3.4. The surface polymer chain length affects the polymer conformation: from brush to mushroom

The one variable that is central to the design of nanoparticle-polymer nucleants is the polymer chain length; very short polymers clearly do not show any ability to affect lysozyme crystallization process. However, when surface bound polymers are larger than

5000 MWt they show increasingly greater effects on the crystallization process. In order to understand this trend, we examined how the polymers at the nanoparticle interfaces changes in their surface coverage in Chapter 3. Clearly, as chains became longer they were less densely populating the interfaces. We hypothesized that this was because the larger polymers adopted mushroom conformations and needed more space per chain at the interface. To verify this we examined quantitatively the hydrodynamic diameter of the various nanoparticle-polymer conjugates as a function of their molecular weight.

Figure 4.5A shows that as the molecular weight of the PEG increases from 1K to 30K, so does the overall length of the polymer on a nanoparticle surface determined from the difference in hydrodynamic diameter (HD), and the core diameter (d). However, this increase is not linear and appears to level off for longer polymer chains. To place these results in context, we bracketed the experimental data between the maximum extension of poly(ethylene) glycol (green line) and the fully coiled polymer diameter for free polymer in solution (red line). The former is defined as the length of a single monomer (0.35 nm) multiplied by the number of monomers per polymer (n).[20,21] This is an unrealistic conformation as the polymer will exhibit secondary structure that could make it much more compact. The coil dimension (Coil) was calculated using Equation 4.2.[22]

Equation 4.1. Hydrodynamic diameter unbound polymer coil

$$\mathbf{Coil} = \mathbf{2}\left\{\frac{\mathbf{3M_W\eta}}{\mathbf{10N_A\pi}}\right\}^{\frac{\mathbf{1}}{\mathbf{3}}}$$

Where, M_W is the molecular weight, η is the intrinsic viscosity, and N_A is Avogadro's number. The intrinsic viscosity is calculated using $\eta = \mathbf{K} * M_W{}^{\alpha}$; where **K** and α are

constants for a given polymer based on the solvent and temperature. For PEG in water at room temperature **K** = 0.0224 mL $mol^{-0.73}$ / $g^{1.73}$ and $\alpha = 0.73$.[23] We would expect that at an interface the polymers would be larger than this free coil diameter which requires ample interactions between all parts of a polymer chain.

As is apparent in Figure 4.4, for all chain lengths the poly(ethylene) glycol length at the surface is in between the extreme extended limit and the free polymer coil. The samples are most similar to the extended configuration when they are shorter as shown in panel B. Here the experimental polymer thickness is expressed as a percent of the extended length. For the 5 nm gold nanoparticle-polymer conjugates the percent extensions were: 59 ± 2% (1K); 54 ± 6% (2K); 47 ± 4% (5K); 48 ± 8% (10K); 32 ± 10% (20K); and 19 ± 0% (30K). The same trend occurs for gold nanoparticles of 10, 15 and 20 nm diameter, except that for the larger particles the shorter PEG can be even more extended.

Similar data has been seen for polymers attached to flat interfaces, as well as for other kinds of polymers attached to nanoparticles.[21,24,25] Briefly, the shortest polymers will densely pack at interfaces to maximize their interchain interactions resulting in a "brush" conformation (Figure 4.4B inset). As polymer chain length increases, intrachain interactions become more important and some coiling occurs resulting in a "mushroom" conformation for tethered (Figure 4.4B inset). Typically, the brush regime is distinguished by "an significant extension", and Krueger *et. al.* classified polystyrene coatings on nanoparticles with extensions between 30 - 50% as "brushes".[22,26] For these polyethylene coatings it is clear that brush behavior is found for extensions between 50 and 70% corresponding to polymer chain lengths below 5,000 molecular weight.

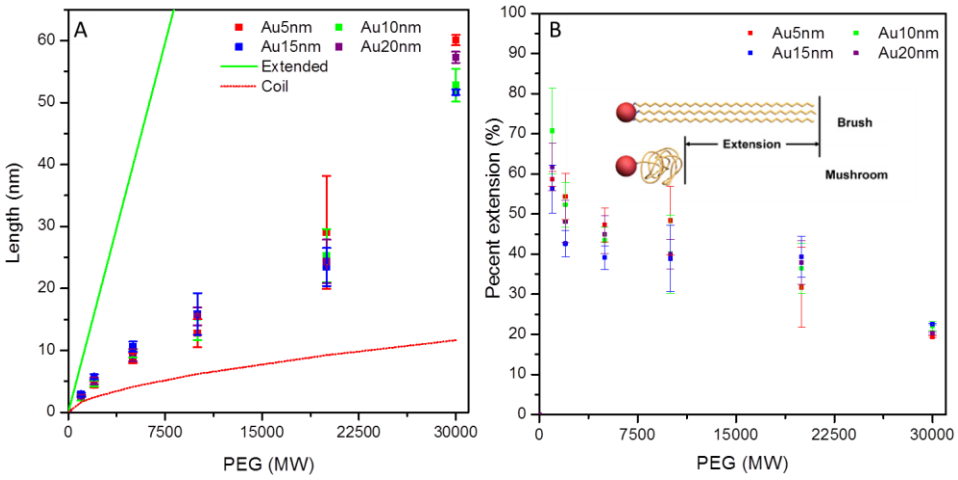

Figure 4.5 Evaluation of PEG based on length and extension

Evaluation of the polymer coating based on (A) length and (B) percent extension (B). The length versus molecular weight for unbound polymer fully extended (green) or in a random coil (red) is compared to the thickness of the polymer bound to a 5 nm (red squares), 10 nm (green squares), 15 nm (blue squares) or 20 nm (purple squares). Binding to a surface causes the polymer to extend and the percent extension defines the conformation as either brush (extended) or mushroom (less extended).

4.3.5. Protein association with nanoparticle-polymer conjugates: chain length dependence

One feature of how nanoparticle-polymer conjugates act in protein crystallization is the pronounced chain length dependence. As seen in Figure 4.3, shorter chains lead to no effect at all on crystallization while longer chains appear to optimize the nucleation. We reasoned that this trend could be explained by an increased protein association with nanoparticle-polymer conjugates.

This hypothesis was based on the observation made in this group and other that short molecular weight polymers are densely packed at nanoparticle interfaces; they are

extended in a brush-like conformation with high surface densities (see Chapter 3).[22,27] Consequently shorter polymers are preferred when nanoparticle core surfaces need to be very protected and inaccessible in solution. In contrast, longer molecular weight polymers assume a more coiled, mushroom-like structure and thus have lower packing density at nanoparticle interfaces. What results are fewer polymers protecting a core nanoparticle surface. Additionally, there is a more irregular and more porous polymer layer presenting itself to the aqueous solution. We reasoned that such a surface would have more assocation with proteins.

Lysozyme association with nanoparticle-polymer conjugates was best measured using equilibrium dialysis experiments. In these studies, any protein not bound to a particle can migrate through a dialysis membrane while protein associated with the polymer – nanoparticle conjugate cannot. Figure 4.5 (black line) shows that only 30% of a control sample of lysozyme under these conditions was retained within the membrane after six days. When lysozyme was exposed to citrate stabilized gold nanoparticles, a nanoparticle known to strongly associate with lysozyme, 58% of the protein was retained inside of the filter.[28] For polymer – nanoparticle conjugates the amount of protein retained varied consistently with the molecular weight of the PEG coating (Figure 4.5). Conjugates made from the shortest molecular weight polymers (1K and 2K) showed relatively small retention of proteins inside of the filter, 45 ± 5% and 55 ± 9% respectively. Once coatings were longer than 5000 molecular weight, however, the retention of lysozyme by the nanoparticle increased smoothly: 60 ± 4% (5K), 69 ± 6% (10K), 72 ± 3% (20K), and 76 ± 1% (30K).

Typically, biomolecule associations can be measured by analytical ultracentrifugation (AUC), where changes in the sedimentation properties of a nanoparticle sample in a protein rich environment indicate that an interaction has occurred.[29] Given our experience with AUC, we initially turned to this tool for probing the association of free proteins with nanoparticles. However, we could find no significant change in the sedimentation coefficients of particles exposed to lysozyme. It may be that the shearing force on the sedimenting particles was enough to strip weakly associating proteins from the conjguate surfaces.

The strength of the interaction between the protein lysozyme and the nanoparticle-polymer surface is not easily measured. We can infer, based on our AUC and equilibrium dialysis data, that it is relatively weak interaction. Our crystallization data also supports this inference. Strong nanoparticle – protein associations have been shown to disrupt a protein's structure.[30] Proteins in partially unfolded or in super folded conformations would not be appropriate nucleation sites for addition proteins, and in fact would be likely to reduce nucleation events, rather than to enhance them as we observe. Additionally, as will be presented in Chapter 6, the diffraction from crystals formed in the presence of nanoparticles matches the native lysozyme structure indicating little disruption to the protein structure.

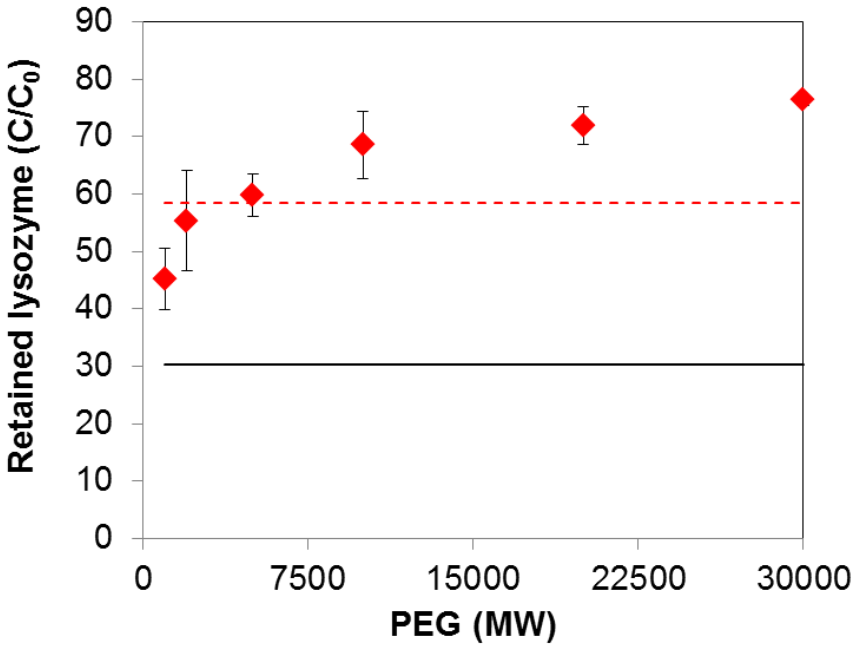

Figure 4.6. Nanoparticle – protein association.

Lysozyme association, as determined from equilibrium dialysis, increases with PEG molecular weight. All samples containing nanoparticle retained more of the protein than the control sample (black line), while only samples with polymer molecular weight coatings >5K exceeded the retention for bare nanoparticles (red dashed line), which are known to associate with lysozyme. Error bars are the standard deviation from n=3.

4.3.6. Effect of nanoparticle-polymer conjugates on protein nucleation

One observation about the mechanism for the nanoparticle-polymer conjugate effects on protein crystallization is that there is a concentration dependent decrease on the time to nucleation even in protein concentrations below the supersolubility region. The T_{nuc} for lysozyme without a nucleant is highly concentration dependent. Figure 4.6A shows that

protein concentrations greater than 4 mg/mL easily overcome the free energy barriers for crystallization and have a similar T_{nuc} as samples with a nanoparticle nucleant present. However, by reducing the initial protein concentration the control sample shows a significant increase in T_{nuc}. Adding short molecular weight polymer – nanoparticle conjugates result in the same concentration dependent T_{nuc} as the control sample for all concentrations. In contrast, the large molecular weight polymer – nanoparticle conjugates nucleate crystal formation at a reduced T_{nuc} regardless of the initial protein concentration. This results in crystal formations that are three times faster at 3.5 mg/mL and seven times faster at 3.0 mg/mL. Figure 4.6B, shows at 3.5 mg/mL, when there are 10 million times more proteins than nanoparticles, there is still a 2.4 fold decrease in the time to nucleation. As the concentration of nanoparticles is increased for a particular protein concentration, nucleation is faster but eventually reaches a plateau corresponding to a five fold reduction in nucleation time. From these results we can conclude that large molecular weight polymer – nanoparticle conjugates are heterogeneous nucleants. They are able to promote nucleation even when protein concentrations are well below the supersolubility limit.

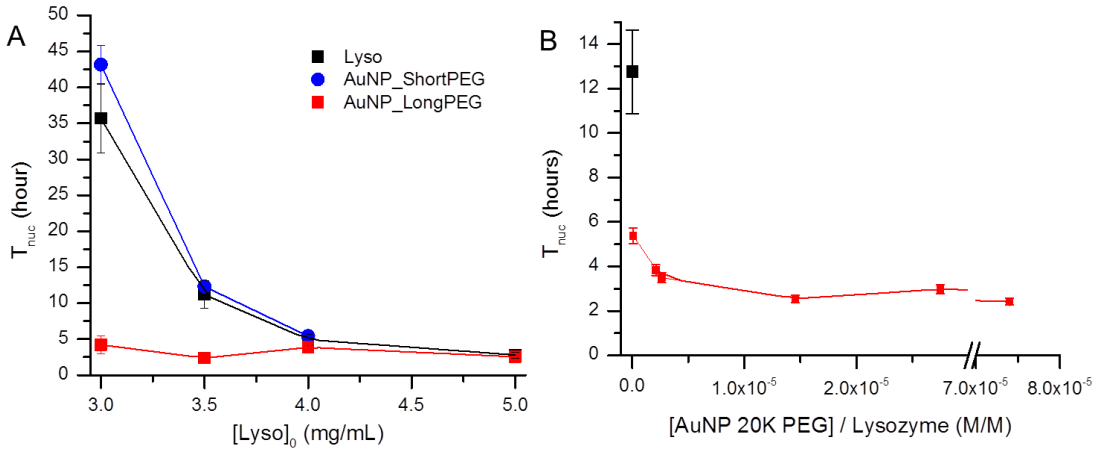

Figure 4.7. Concentration dependent changes in T_{nuc}.

(A) Lysozyme concentration and (B) nanoparticle per protein concentration effects on the time to nucleation (T_{nuc}) for lysozyme control (black squares), short polymer – nanoparticle conjugates (blue circles) and long polymer – nanoparticle conjugates (red squares). Nanoparticle concentration dependent curve was run at the 3.5 mg/mL initial lysozyme concentration.

In addition, phase diagrams with and without nanoparticle nucleants (Figure 4.7) show that nanoparticles expand supersolubility for lysozyme which promotes the formation of crystals while reducing precipitation. Small volume batch method crystallization conditions with lysozyme concentrations from 5 to 60 mg/mL and ionic strength solutions from 0.5 to 4.0 M with long polymer – nanoparticle conjugates have more "hits" (conditions that form crystals) and a decrease in conditions that produce protein aggregates. Protein crystals are found in 43% of the conditions with protein alone and 58% with nanoparticle additives. The experiment was repeated (not shown) and found that the same expansion of protein solubility and similar increase in conditions had crystal hits: 40% and 56% without and with nanoparticles, respectively.

The consequences of this observation are significant as it suggests the use of nanoparticle-polymer conjugates as additives to improve high-throughput protein crystallization. Current methods for high throughput screening subject a protein to a multitude of conditions, which differ in solvent, buffer composition, pH, buffer strength, ionic strength and/or additive concentrations. The object is to determine the best set of conditions to produce crystals. However, these screening methods suffer from a low success rate, time consuming crystal formation, and tedious sample evaluation to detect crystals.[3] By including polymer-nanoparticle conjugates there is a greater probability that crystals will form during the screen. Also, crystals are more easily visualized due to their strong color.

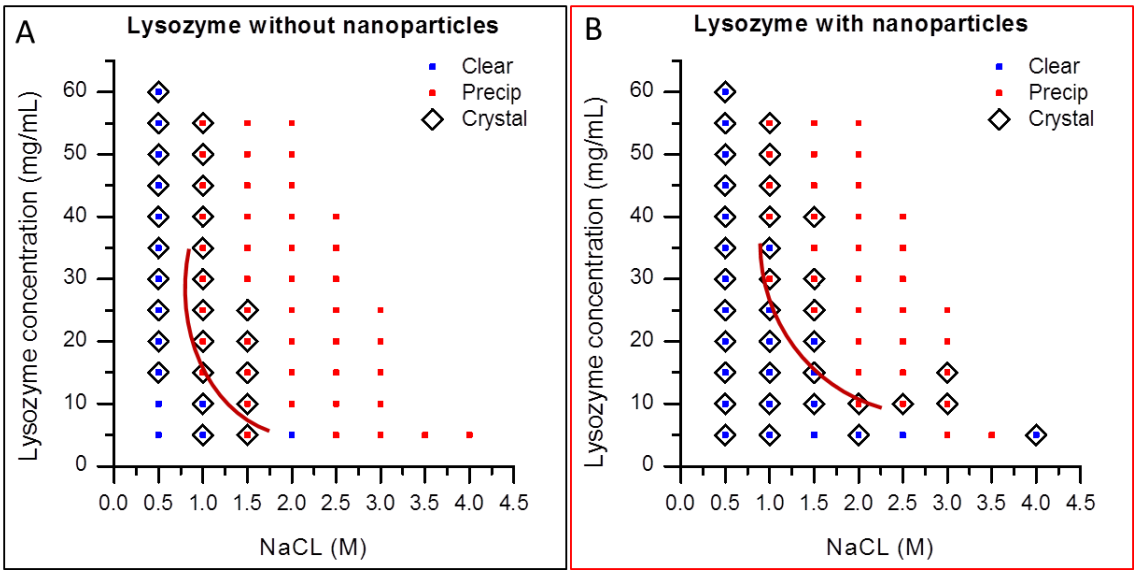

Figure 4.8. Lysozyme phase diagrams.

Lysozyme phase diagrams were generated for protein concentrations from 5 to 60 mg/mL in ionic strength solutions containing NaCl from 0.5 to 4.0 M. Blue squares represent clear conditions, red squares are conditions that formed precipitates and the black diamonds are conditions that produced crystals. Supersolubility curves are show for each sample; (A) without nanoparticles and (B) with nanoparticles.

As an example, Figure 4.8 shows that nanoparticle-polymer conjugates expanded the number of crystal forming conditions and also decreased the precipitate formation for lysozyme. Two sets of 96 crystal screening solutions; PEG Suite (Qiagen) and Index Screen (Hampton Research) were used to prepare 192 unique conditions for three samples: a control protein stock solution, and the same stock solution with either 1 nM or 10nM nanoparticle-polymer conjugate (gold 10nm, 20000 MWt PEG). At either concentration the nanoparticle-polymer conjugates increased the number of protein crystal forming conditions and decreased the occurrence of precipitates (Figure 4.8A). The control sample crystallized in 63 of the conditions, while the low nucleant concentration yielded 72 crystal forming conditions and the higher nanoparticle concentration had crystals form in 70 cases. In this case, the additive didn't prevent the formation of precipitates at 1 nM, however they slightly reduced precipitate formation at the higher concentration. There were 38 precipitating solutions for the control and low concentration samples and 34 for the higher nucleant concentration.

Nanoparticles behave ideally for use in current screening strategies, they are easy to introduce and facilitating crystal formation without disruption to the set of conditions that were favorable for the control sample. A measure of this is the number of unique crystallization conditions; cases where crystals formed for either the control or the samples containing nanoparticles but not for both. Figure 4.8B shows 4 uniquely crystallizing conditions for the control, and 26 with nanoparticles. Meaning screens with nanoparticles enhance crystallization without detraction from the native sample.

Nanoparticle nucleants were easily incorporated into high throughput strategies and improved the crystallization process. However, lysozyme is a protein that is already straightforward to crystallize. To evaluate the generality of the results, a set of five additional proteins were evaluated to determine if nanoparticle-polymer conjugates could be advantageous as nucleants for harder to crystallize proteins.

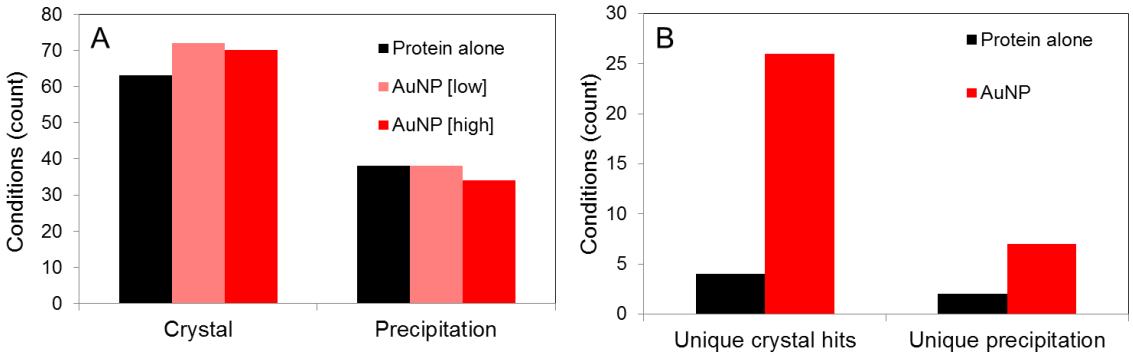

Figure 4.9. High throughput crystallization of lysozyme.

High throughput crystallization of lysozyme count of the conditions that (A) form crystals or precipitate without nanoparticles (black bars), with 1 nM polymer – nanoparticle conjugates (pink bars), and with 10 nM polymer – nanoparticle conjugates (red bars). (B) Unique conditions are those that form crystals or precipitates either without nanoparticles (black bars) or with nanoparticles (red bars), but not in both cases.

4.3.7. Nanoparticle-polymer conjugates nucleate the crystallization of diverse proteins

The five additional proteins evaluated were ferritin, human serum albumin (HSA), lipase B, xylanase, and glucose isomerase; Table 4.2 shows the characteristics of all the proteins used to evaluate the use of nanoparticle nucleants in high throughput strategies. The net

surface charge for each protein will be different because their isoelectric points range from 3.0 to 11.0. The protein dimensions range from 12.5 x 12.5 nm for ferritin to 4.5 x 3 nm for lysozyme. For size comparison the core gold nanoparticle are on the order of 10 nm (11.7 nm) and the average 20K PEG thickness is ~30 nm, resulting in a conjugate diameter of ~70nm; Figure 4.10 represents pictorially the relative sizes of the proteins to the core particle.

Table 4.2. Protein characteristics.

		Dimensions (nm)			
	MW (kDa)	a	b	c	Isoelectric point
FERRITIN	450	12.5			6.0
HUMAN SERUM ALBUMIN	66	8.5	3.8	4	4.7
LIPASE B	35	9.2	6.2	4.7	6.0
XYLANASE	21	9.1	3.9	5	9.0
GLUCOSE ISOMERASE	173	10.3	9.4	9.9	3.0
LYSOZYME	14.6	4.5	3	3	11.0
Nanoparticle		10			
PEG layer	20	30			

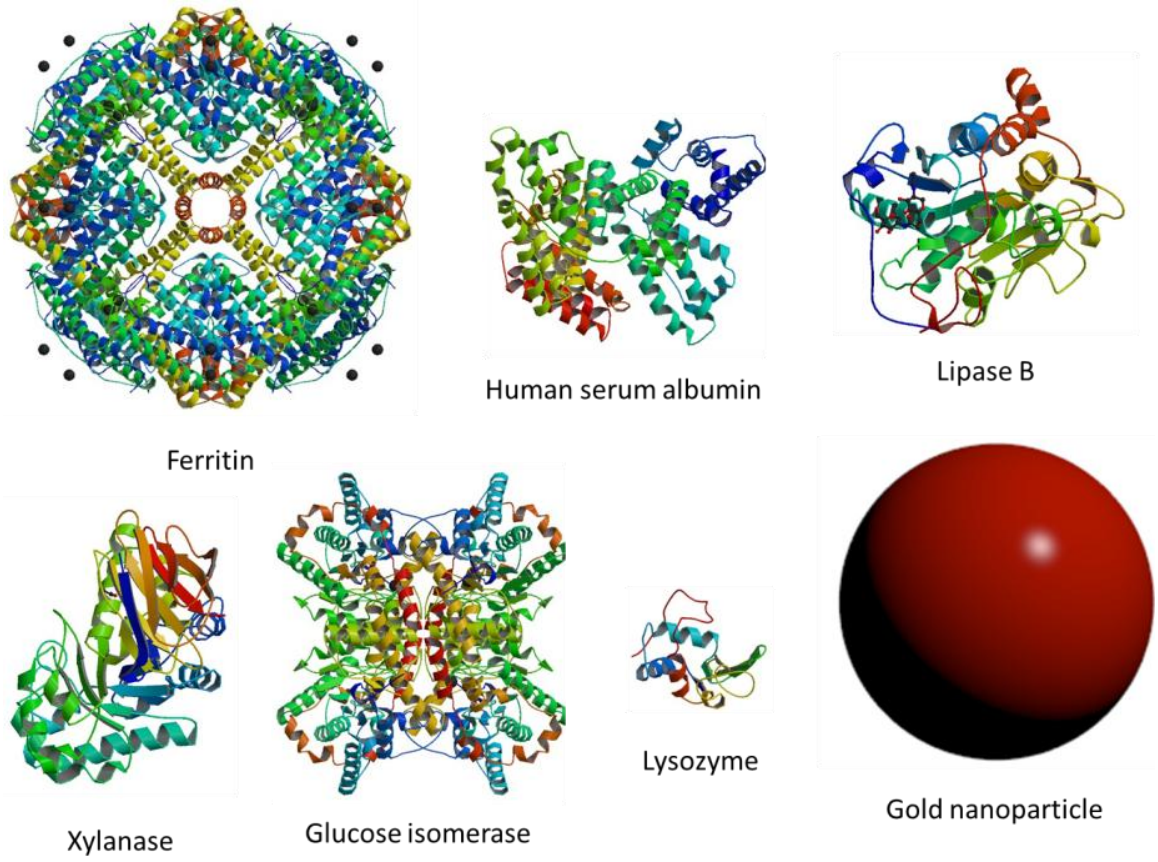

Figure 4.10. Relative sizes of the proteins and the core nanoparticle, d=10 nm gold.

Protein structures obtained from the protein data bank and displayed for their size relative to the 10nm gold nanoparticles. Sizes of the proteins range from 12.5 nm for ferritin to 3x3x4 nm for lysozyme.

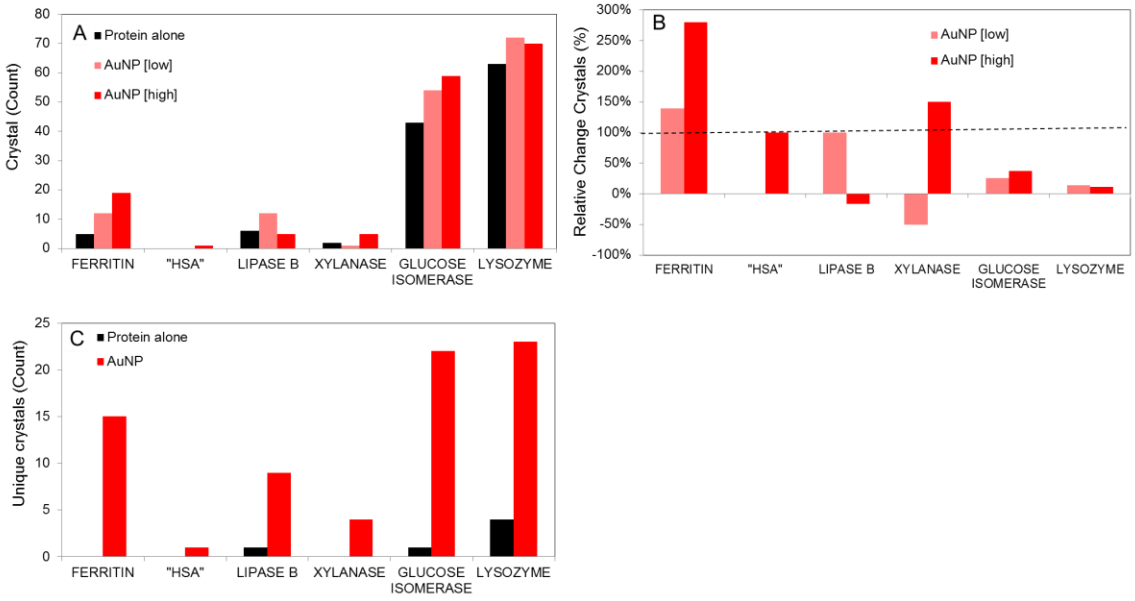

Figure 4.11. High throughput crystallization screens of ferritin, human serum albumin (HSA), lipase B, xylanase, glucose isomerase and lysozyme.

High throughput crystallization screen results for ferritin, human serum albumin (HSA), lipase B, xylanase, glucose isomerase and lysozyme. Counts of (A) the total number of conditions that form crystals and (B) their change relative to the control. (C) Unique crystals forming conditions* for the control samples without nanoparticles (black bars), with 1 nM polymer – nanoparticle conjugates (pink bars), and with 10 nM polymer – nanoparticle conjugates (red bars). Dashed line was added at 100% as a guide to the eye.

*Unique conditions are those that form crystals either without nanoparticles (black bars) or with nanoparticles (red bars), but not in both cases.

Figure 4.10A&B show graphically the information in Table 4.3; polymer – nanoparticle nucleants are successful at increasing the number of crystal forming conditions, or ‘hits’, for all the proteins evaluated. Ferritin crystals formed in only 5 solutions for the control sample as opposed to 12 and 19 hits for a relative change of 140% and 280% over the

control with the 1 nM and 10 nM nanoparticle additives, respectively. Human serum albumin had only one macroscopic crystals form and it occurred in a condition prepared with the high concentration of nucleant (100% relative change). Lipase B had a slightly higher number of control crystal hits, forming crystals in 6 solutions. For samples with a 1 nM addition of nanoparticle nucleants the number of crystal forming conditions increased from 6 to 12, (100%) while the high concentration of nucleants only had 5 (-17%) conditions that formed crystals. The xylanase control sample had 2 crystal hits, while the nucleant samples induced 1 and 5 hits for a -50% and 150% relative change for the 1nM and 10nM concentrations. Glucose isomerase, like lysozyme, has a high success rate of crystallization (43, 22% of all conditions tested) for the control sample. However, glucose isomerase had a more significant relative increase, 26% (11 more conditions) with the low concentration and 37% (16) with the higher nanoparticle concentration.

Unique crystal forming conditions have crystals form only with or without nanoparticles, but not for both. A total of only six unique conditions formed without nanoparticles for all of the samples, in contrast with 74 unique conditions found with nanoparticle and every protein has at least one (Figure 4.10C). Nanoparticle nucleants increase the crystal hit rate by facilitating the formation of crystals in conditions that do not work for the native protein control sample. Ferritin, glucose isomerase, and lysozyme had 15, 22, and 23 unique conditions with nanoparticles which account for 48%, 19% and 16% of all their crystal forming conditions, respectively. The proteins that had fewer crystals hits also had fewer unique conditions with nanoparticles, but these conditions account for a greater percentage of crystallizing conditions, i.e., human serum albumin has 1 unique

condition, which is 100% of crystal forming conditions, lipase B has 9 which are 53% and xylanase has 4 for 67%. Nanoparticle nucleants are able to form crystals in unique conditions by expanding the phase space and allowing crystallization in metastable regions, thus increasing the success of a crystallization screen.

Table 4.3. High throughput crystallization results for multiple proteins.

	CRYSTAL			PRECIPATATE			UNIQUE CONDITIONS	
	-	+	++	-	+	++	-	+
FERRITIN	5	12	19	20	20	17	0	15
HUMAN SERUM ALBUMIN	0	0	1	11	7	6	0	1
LIPASE B	6	12	5	13	11	8	1	9
XYLANASE	2	1	5	1	0	0	0	4
GLUCOSE ISOMERASE	43	54	59	41	33	36	1	22
LYSOZYME	63	72	70	38	38	34	4	23

(-) is without nanoparticles (+) is with 1 nM nanoparticles, (++) is with 10 nM nanoparticles

We also evaluated pre-crystalline materials such as microcrystals, blobs or fibrils in the screens with and without the nanonucleants. Such products can indicate a region where favorable protein interactions are possible and therefore the set of conditions could possibly be optimized to yield a viable crystal. Distinguishing between precipitates and microcrystals can be difficult. For consistency, we considered two main properties to differentiate the two: reflectivity and placement in the well. As seen in Figure 4.11A the precipitates tend to be more buoyant, less reflective, and not isolated in defined sections of the well. Microcrystals, as shown in Figure 4.11B, are typically more reflective and

dense; which allow them to settle to the bottom of the well, usually in a uniform fashion. Determining the cutoff from microcrystal to crystals was done through visible identification of facets using a microscope at 10 X magnifications or below, microcrystals are too small to make out individual faces at these magnifications.

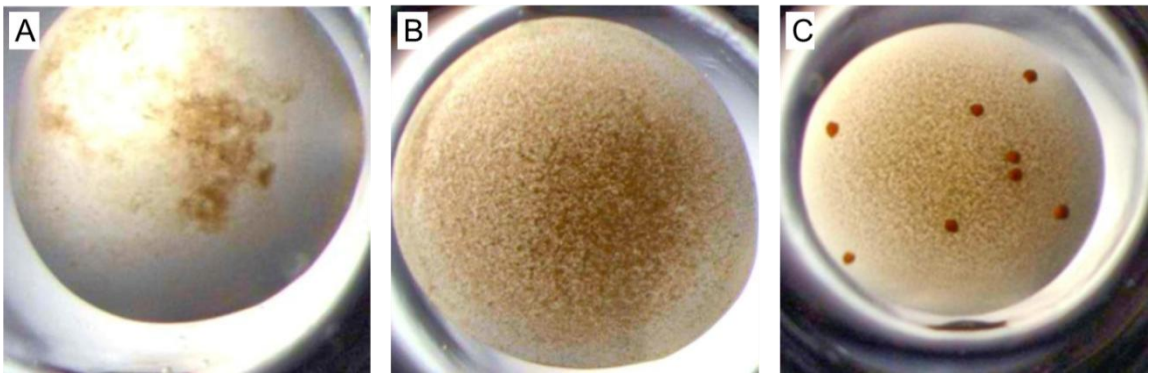

Figure 4.12. Products of crystallization.

Images of crystallization products: precipitate (A), microcrystals (B), crystals (C).

Figure 4.12 shows that the nanoparticle-polymer conjugates also decrease the number of conditions that form unfavorable precipitates and increase the total crystallization hits including pre-crystalline materials. Human serum albumin and lipase B have similar nucleant concentration dependent decreases in the number of conditions that form precipitates and increases in total hit counts. Ferritin and lysozyme behave similarly, neither protein sample decreases in the precipitate forming conditions with the low concentration of nanoparticle nucleants, yet they both show a greater total hit count at that nucleant concentration. Glucose isomerase has a significant decrease in precipitation with the lower concentration nanoparticles, but many of the conditions that precipitated with the higher concentration of nanoparticles formed pre-crystalline microcrystals with

the lower concentration, signifying how closely related these conditions tend to be. Xylanase only had one precipitate forming condition and that was for the control sample, with the addition of nanoparticles that condition did not form precipitates. For lysozyme the total hit count and the number of crystals hits are the same because lysozyme only formed crystals or precipitates.

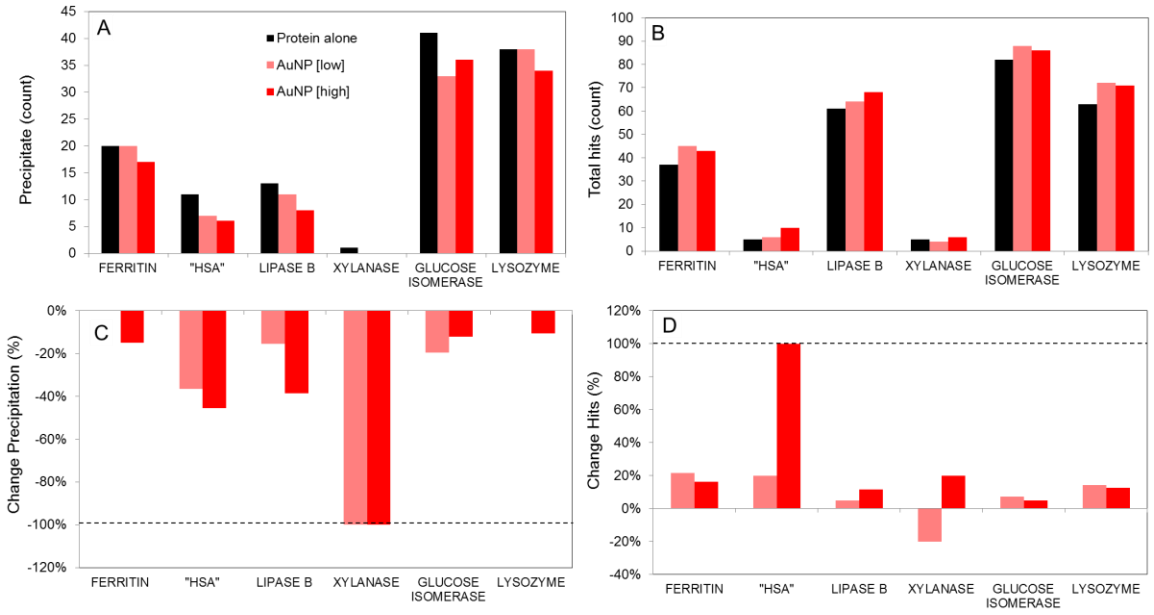

Figure 4.13. High-throughput results.

Crystallization wells typically form either precipitates, microcrystals or crystals. (A) Number of conditions that form precipitates and (B) total "hits" including crystals and precrystalline materials increase for all protein samples. The change relative to the for (C) precipitate formation and (D) total hits. Black bars are control proteins without nanoparticles, pink with 1 nM nanoparticles, and red bars are for 10 nM nanoparticles; dashed lines added at 100% change as a guide to the eye.

Another observation during the crystallization of the high crystal hit rate samples (ferritin, glucose isomerase and lysozyme) was the increase in crystal quantity with increased nanoparticle-polymer conjugate concentration. The time it takes to nucleate

crystal formation affects the quantity and size of produced crystal sample; a faster nucleation results in more abundant and smaller crystals. Many of the screened conditions for ferritin, glucose isomerase and lysozyme formed crystals, these conditions also tended to have crystal count increases as the nanoparticle concentration was raised from 1 nM to 10 nM. For the condition shown, ferritin crystal quantity increases from zero without nanoparticles, to 8 with 1nM AuNP and to 26 with 10 nM AuNP (Figure 4.13A). Glucose isomerase crystals are shown in Figure 4.13B and form in quantities of one, four and ten with 0, 1 and 10 nM AuNP additives respectively. For the condition shown in Figure 4.13C lysozyme crystals counts are zero, two and three with increasing nanoparticle concentrations.

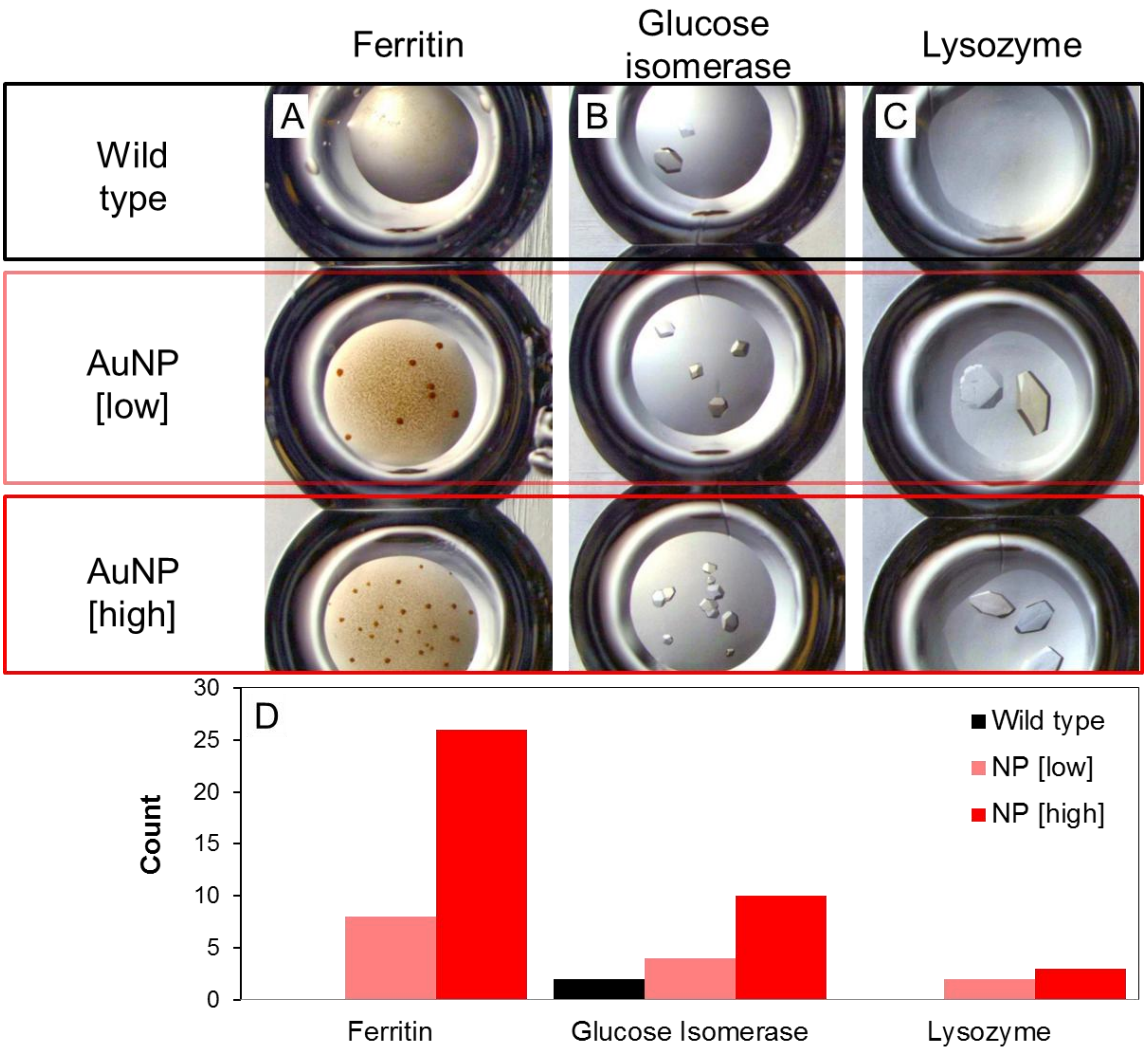

Figure 4.14. Concentration effects of nanoparticles.

Concentration effects of nanoparticles on crystal counts for (A) ferritin, (B) glucose isomerase and (C) lysozyme. (D) The increase in nanoparticle concentration correlated with an increase in the number of crystals that formed; black bars are without nanoparticles, pink with 1 nM nanoparticles, and red bars are for 10 nM nanoparticles.

4.4. CONCLUSION

Nanoparticle-polymer conjugates can be designed to nucleate protein crystallization. Large molecular weight PEG assume a mushroom-like coiled conformation creating surfaces that allow protein association; this association promotes nucleation in a manner similar to heterogeneous nucleation. These sterically stabilized nanoparticle-polymer conjugates remain non-aggregating in crystal growth media. They produce more protein crystals in a shorter amount of time than protein alone; this effect is due to the nanoparticle-polymer conjugate as opposed to free polymer or free nanoparticle. Polymer – nanoparticle conjugates could be easily incorporated into high throughput crystallization screens. In this setting, they increased the occurrence of crystal "hits" as well as unique crystal forming conditions. They also decreased the prevalence of protein precipitation in many different kinds of proteins. Nanoparticle-polymer conjugates can have significant effects on protein crystallization, and offer as nucleants many properties useful for improving high throughput crystallization strategies

4.5. REFERENCES

(1) Chayen, N. E. *Trends in biotechnology* **2002**, *20*, 98.

(2) Saridakis, E.; Chayen, N. E. *Trends in Biotechnology* **2009**, *27*, 99.

(3) Thakur, A. S.; Robin, G.; Guncar, G.; Saunders, N. F. W.; Newman, J.; Martin, J. L.; Kobe, B. *PLoS ONE* **2007**, *2*, e1091.

(4) Chayen, N. E.; Saridakis, E.; Sear, R. P. *Proceedings of the National Academy of Sciences of the United States of America* **2006**, *103*, 597.

(5) Ino, K.; Udagawa, I.; Iwabata, K.; Takakusagi, Y.; Kubota, M.; Kurosaka, K.; Arai, K.; Seki, Y.; Nogawa, M.; Tsunoda, T.; Mizukami, F.; Taguchi, H.; Sakaguchi, K. *PLoS ONE* **2011**, *6*, e22582.

(6) Chayen, N. E.; Saridakis, E.; El-Bahar, R.; Nemirovsky, Y. *Journal of Molecular Biology* **2001**, *312*, 591.

(7) McPherson, A.; Shlichta, P. *Journal of Crystal Growth* **1988**, *90*, 47.

(8) van Meel, J. A.; Sear, R. P.; Frenkel, D. *Physical Review Letters* **2010**, *105*, 205501.

(9) Kallio, J. M.; Hakulinen, N.; Kallio, J. P.; Niemi, M. H.; Kärkkäinen, S.; Rouvinen, J. *PLoS ONE* **2009**, *4*, e4198.

(10) Hodzhaoglu, F.; Kurniawan, F.; Mirsky, V.; Nanev, C. *Crystal Research and Technology* **2008**, *43*, 588.

(11) Bessho, Y.; Ataka, M.; Asai, M.; Katsura, T. *Biophysical Journal* **1994**, *66*, 310.

(12) Kreibig, U.; Althoff, A.; Pressmann, H. *Surface Science* **1981**, *106*, 308.

(13) He, Y. Q.; Liu, S. P.; Kong, L.; Liu, Z. F. *Spectrochimica Acta Part A: Molecular and Biomolecular Spectroscopy* **2005**, *61*, 2861.

(14) Zhulina, E. B.; Borisov, O. V.; Priamitsyn, V. A. *Journal of Colloid and Interface Science* **1990**, *137*, 495.

(15) Zhang, F.; Skoda, M. W. A.; Jacobs, R. M. J.; Zorn, S.; Martin, R. A.; Martin, C. M.; Clark, G. F.; Goerigk, G.; Schreiber, F. *The Journal of Physical Chemistry A* **2007**, *111*, 12229.

(16) Asanithi, P.; Saridakis, E.; Govada, L.; Jurewicz, I.; Brunner, E. W.; Ponnusamy, R.; Cleaver, J. A. S.; Dalton, A. B.; Chayen, N. E.; Sear, R. P. *ACS Applied Materials & Interfaces* **2009**, *1*, 1203.

(17) Galkin, O.; Vekilov, P. G. *Proceedings of the National Academy of Sciences* **2000**, *97*, 6277.

(18) McPherson, A. *Journal of Biological Chemistry* **1976**, *251*, 6300.

(19) Munishkina, L. A.; Cooper, E. M.; Uversky, V. N.; Fink, A. L. *Journal of Molecular Recognition* **2004**, *17*, 456.

(20) Heuberger, M.; Drobek, T.; Spencer, N. D. *Biophysical Journal* **2005**, *88*, 495.

(21) Gennes, P. G. d. *Macromolecules* **1980**, *13*, 1069.

(22) Krueger, K. M.; Al-Somali, A. M.; Mejia, M.; Colvin, V. L. *Nanotechnology* **2007**, *18*, 475709.

(23) Lee, J.; Tripathi, A. *Analytical Chemistry* **2005**, *77*, 7137.

(24) Kruger, K. M.; Al-Somali, A. M.; Mejia, M.; Colvin, V. L. *Nanotechnology* **2007**, *18*, 475709 (7pp).

(25) Plunkett, K. N.; Zhu, X.; Moore, J. S.; Leckband, D. E. *Langmuir* **2006**, *22*, 4259.

(26) de Gennes, P. G. *Advances in Colloid and Interface Science* **1987**, *27*, 189.

(27) Dukes, D.; Li, Y.; Lewis, S.; Benicewicz, B.; Schadler, L.; Kumar, S. K. *Macromolecules* **2010**, *43*, 1564.

(28) Jamison, J.; Bryant, E.; Kadali, S.; Wong, M.; Colvin, V.; Matthews, K.; Calabretta, M. *Journal of Nanoparticle Research* **2011**, *13*, 625.

(29) Calabretta, M.; Jamison, J. A.; Falkner, J. C.; Liu, Y.; Yuhas, B. D.; Matthews, K. S.; Colvin, V. L. *Nano Letters* **2005**, *5*, 963.

(30) Lundqvist, M.; Sethson, I.; Jonsson, B.-H. *Langmuir* **2004**, *20*, 10639.

Chapter 5

MESOSCOPIC BIOTEMPLATES FORMATION OF COMPOSTITE (NANOPARTICLE-PROTEIN) CRYSTALS

In the last Chapter we illustrated how nanoparticle – protein associations can promote the nucleation of protein crystals. Here, we consider the properties of the resulting crystals. Nanoparticle-polymer conjugates are examples of nucleating agents that become internalized into the growing crystal. What results are composite nanoparticle-protein

*Work performed within this chapter is the collaborative efforts of me and members of the Colvin lab, Hafner lab and Shamoo lab. Courtney Payne (Hafner lab) provided all of the PEGylated shaped gold nanoparticles, Dr. Huiguang Zhu (Colvin lab) provided all of the PEGylated quantum dots and iron oxide materials, Dr. Carolina Avendano (Colvin lab) ran and processed all SQUID data, Kasia Walkiewicz (Shamoo lab) provided training for crystallization techniques. In addition, I had help from many Colvin lab interns including: Montoya Savala (Preliminary work with quantum dots), Ajoke Williams (UV-vis spectroscopy), Raymond Verm (UV-vis spectroscopy), Michael Lillierose (nanoparticle sample prep and characterization), and Naushaba Ali (nanoparticle sample prep and characterization).

materials with relatively high concentrations of nanoparticles. One interesting finding is the sheer range of nanoparticles that can be incorporated at high concentrations into protein crystals. Gold nanoparticles up to 50 nm diameter; gold prisms and rods; iron oxide nanoparticles and quantum dots all could be incorporated. The only critical design feature was the polymer surface coating: they had to provide steric stabilization in the crystal growth medium and long enough poly(ethylene) glycol chains to ensure that the polymers were close to a mushroom-like conformation. The properties of the resulting nanoparticle-polymer composites are reflective of the type of nanoparticle that is incorporated. For most examples, the properties of the composite are similar to that of the individual nanoparticles. The one exception was found for iron oxide nanoparticles which were apparently non-magnetic at low temperatures in these crystals.

5.1. INTRODUCTION

The collection of nanoparticles into solid phase hosts – either randomly arranged or ordered – has great potential value in areas as diverse as catalysis and medicine.[1-7] In such structures the individual properties of the nanoparticles can simply be multiplied by their collection into a larger material; alternatively, nanoparticle-nanoparticle interactions can give rise to new optical and magnetic phenomena. Supraparamagnetic particles, for example, if they are within several of their diameters from each other can align their magnetic dipoles giving rise to large, permanent magnetization.[8,9] Optically active resonances in metals can lead to smaller energy excitations.[10-12] Such collective

properties provide an additional level of tunability for nanoscale materials and in some cases entirely new kinds of behavior.

A challenge for the material chemist is the formation of these nanoparticle collections in three-dimensional and optically transparent substrates. Costly lithography processes can provide only a two dimensional pattern; for three dimensions other strategies based on chemical assembly are more practical. Natural systems provide excellent examples of the assembly of organic and inorganic materials into bulk composite materials. Biomolecules can have functions that interact with inorganic components, and also present moieties that help define a larger hierarchical ordering for a macroscopic structure.[13] Bone is perhaps the best example of this.[14]

These observations have inspired chemists to leverage the association of biomolecules to collect and in some cases even order nanoparticles in three dimensional composite materials. One of the first examples was the use of two-dimentional arrays of s-layer proteins to template nanoparticle binding to surfaces.[15] Other methods have used nanoparticles modified with peptides, proteins, RNA, or DNA which form arrays that can incorporate the bionanoconjugates.[16-20] Protein and virus crystals have also been used to define arrays of metal nanostructures.[6,21-24] In some examples, a nanoparticle is first grown inside of a protein or virus capsid which his subsequently crystallized; in other cases, the nanoparticles are formed after the crystallization process by the infusion of precursor salts and subsequent reactions to form solid state materials.[6,22-24] These approaches allow only materials to be formed within the pores and cavities of the biomolecule, a constraint which necessarily limits the size and composition of particles.

In this Chapter, we show that through the design of the appropriate surface, nanomaterials can be driven to incorporate into three dimensional protein crystals. Central for this incorporation is the use of surface attached polymers at nanoparticle interfaces. These coatings both provide steric stabilization to the nanoparticles during the crystal growth process, as well as ensure weak interactions with proteins. When proteins subsequently begin to crystallize, nanoparticles are incorporated into the growing crystal. What results is a very concentrated protein-nanoparticle crystal that contains a highly organized protein lattice with inorganic nanoparticles evenly distributed throughout the structure. The incorporation process can be applied to wide range of nanoparticle compositions (e.g. quantum dots, magnetic oxides, nobel metals) and even shapes. Most examples of nanoparticle-protein composites exhibit optical, fluorescent and magnetic properties reflective of the incorporated nanomaterials. In the case of nanorods, however, the protein crystallization process serves to align the rods along one axis leading to strong polarization in the resonant plasmon modes.

5.2. RESULTS AND DISCUSSION

5.2.1. The dynamic incorporation of nanoparticles into protein crystals

As discussed in Chapter 4, nanoparticle-polymer conjugates can be designed to weakly associate with many proteins. The most critical parameter to control is the length of the surface attached polymer chain. Large molecular weight poly(ethylene glycol) (PEG) coatings allow for the weak association of proteins with the nanoparticle-polymer

conjugates, and consequently the rapid nucleation of protein crystals (Chapter 4, Figures 4.5 and 4.6). By way of review lysozyme crystallization solutions are shown in the Figure 5.1(A-H) for four samples: the control, without any nanoparticles, with the addition of citrate coated gold nanoparticles (AuNP) and two samples containing polymer – nanoparticle conjugates (AuNP_PEG); a short molecular weight polymer and a longer. The lysozyme control sample, image 1A, is a clear solution. After 24 hours at 10 °C clear crystals have formed on the cuvette walls and deposited on the floor of the cuvette from the solution. The middle case, a non-sterically stabilized gold nanocrystal, becomes aggregated in solution – turning purple and resulting in no change to the crystal number or size. However, nanoparticle-polymer conjugates remained dispersed and the sample containing the longer polymer had rapid formation of many red protein crystals.

A feature not discussed in Chapter 4 is the notable color of the crystals for the rapidly nucleating crystals. As is apparent in Figure 5.1, nanoparticle-polymer conjugates that promote nucleation also result in the formation of crystals with a distinct red color. Also notable is that the color of the gold nanoparticle solution becomes less pronounced. We reasoned that the gold nanoparticles must incorporate into the growing protein crystals. Over time this depletes the solution of gold nanoparticles as the red crystallites transfer from the solution phase into the growing crystals (Figure 5.1H).

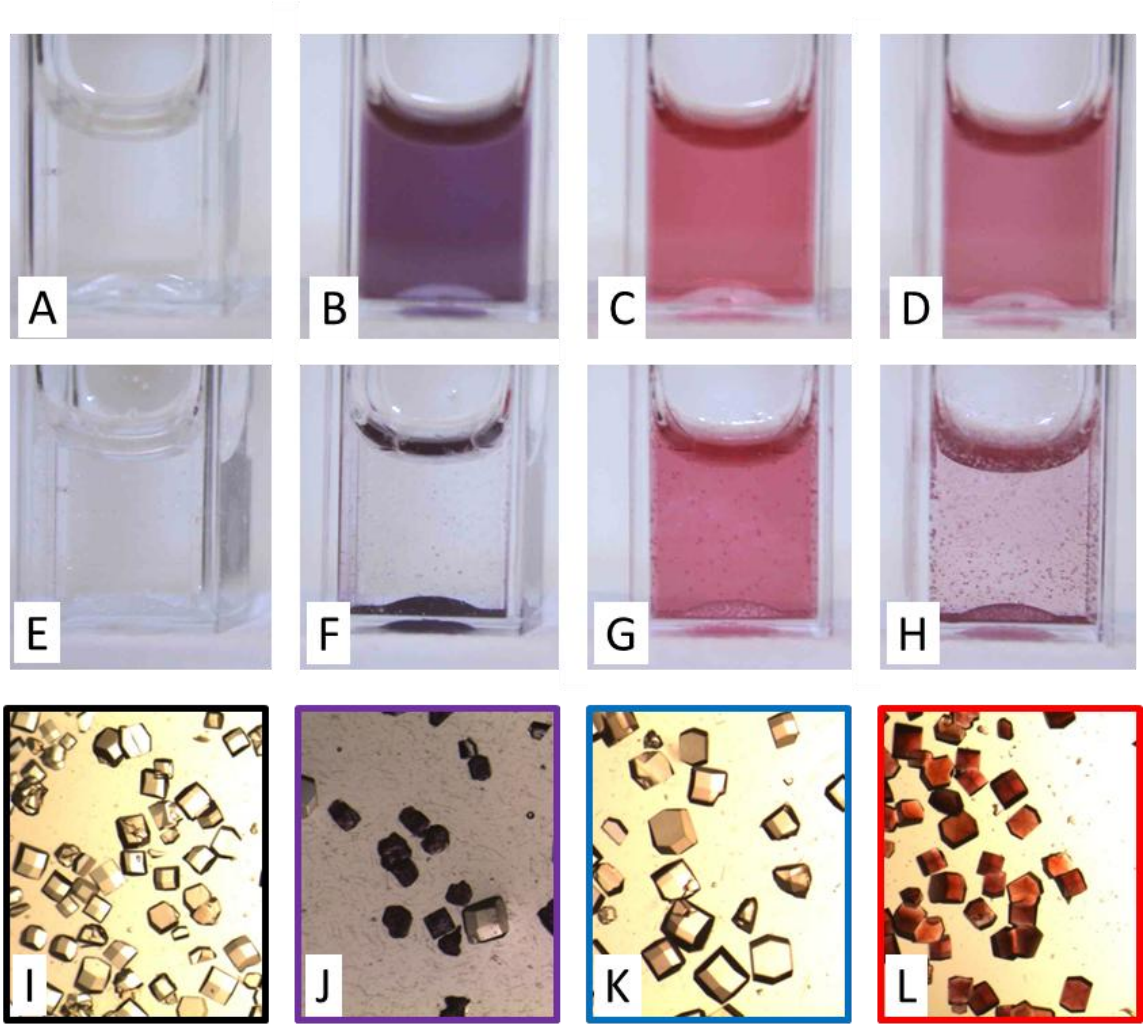

Figure 5.1 Lysozyme crystallization images.

(A,E,I) Lysozyme control sample, (B,F,J) with citrate coated gold nanoparticles, (C,G,K) AuNP_1KPEG coated gold nanoparticles and (D,H,L) AuNP_5KPEG coated gold nanoparticles (A-D) at time 0 hours, (E-H) after 24 hours at 10 °C and (I-L) the resulting microscope images a 4X magnification.

We used absorbance spectroscopy to measure the change in the solution concentration versus time. The absorbance at 301 nm (Figure 5.2A) and 523 nm (Figure 5.2B) were used to determine the change in lysozyme concentrations (Figure 5.2C&D) spectroscopically for four crystallization samples: a control sample, an ionically

stabilized gold nanoparticle (5 nM), and two nanoparticle-polymer conjugates; a short 2000 molecular weight coated sample and a long 20,000 molecular weight coated sample. Two concentrations of nanoparticle polymer conjugate were analyzed 5 nM and 10 nM. The black curve (only at 301 nm) shows the control sample for which only protein is present; because nucleation is not rapid, its concentration changes only slightly in the first several days. After correcting for the nanoparticle absorbance contribution in the UV region of spectrum lysozyme curves could be determined for all the samples. The ionically stabilized nanoparticle rapidly aggregates and is removed from solution, resulting in a drastic and rapid drop in the absorption due to sedimentation of the gold nanoparticle aggregates (Figure 5.2B). Some protein is also removed as it is known to surface associate with the charged gold surface (Chapter 4, section 4.3.4).

The nanoparticle-polymer conjugates had different behavior in the crystallization growth media than these two controls. Over sixty hours, the sample with the shortest polymer chain (blue) had little change in either the protein or nanoparticle-polymer concentration, regardless of loading. This is consistent with the observations noted in Chapter 4 which found these particles had little impact on protein crystallization. In contrast, the nanoparticle-polymer conjugate with the longer 20,000 molecular weight polymer coating had a steady decrease in both the protein and the nanoparticle concentration. Each component was removed from the solution at a constant rate, an observation consistent with a co-crystallization of both species. The depletion of the lower concentration of nanomaterials was complete at 38 hours, while the protein continued to decrease. In this sample, the nanoparticle-conjugate was used up in the early stages of the crystallization process.

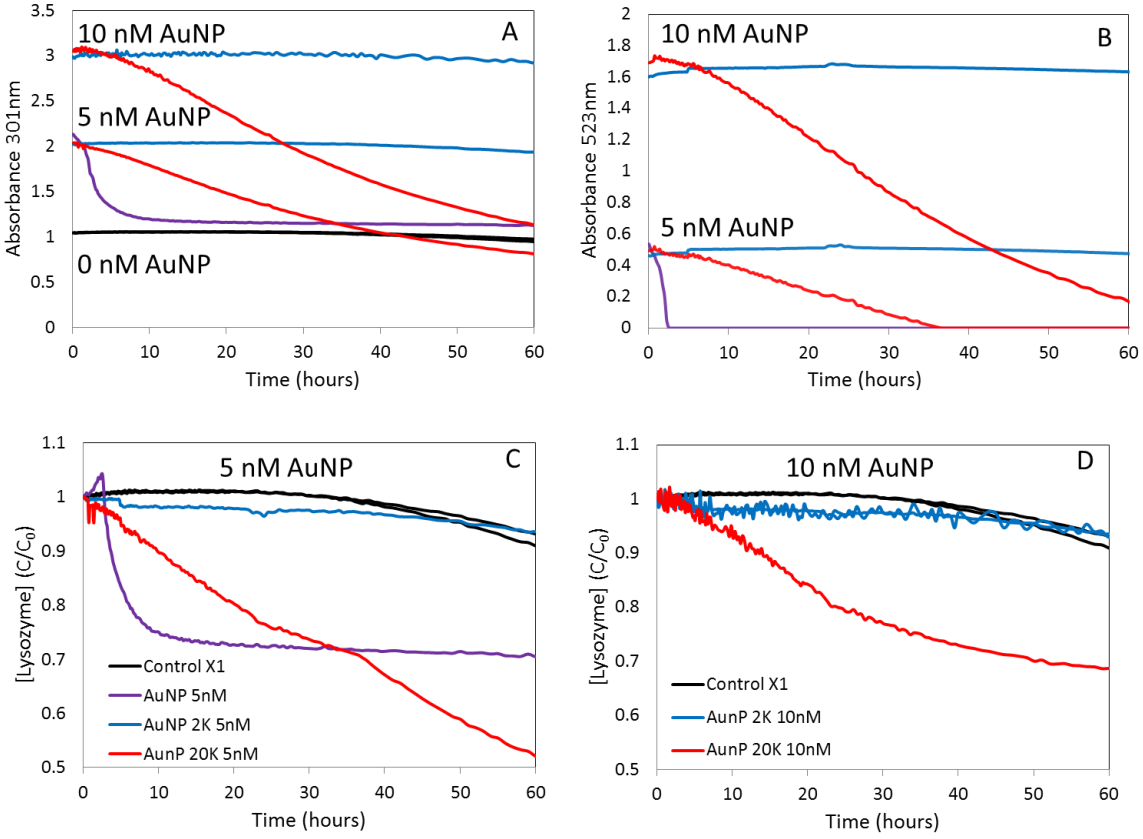

Figure 5.2 Change in protein and nanoparticle concentrations

The raw absorbance at (A) 301 nm and at (B) 523 nm over time, used to determine lysozyme concentrations during crystallization for a control sample (black), citrate coated gold nanoparticles (AuNP, purple), 2K PEG-SH coated gold nanoparticles (AunP 2KPEG, blue) and 20K PEG-SH coated gold nanoparticles (AuNP 20KPEG,red). After correcting the absorbance at 301 nm for the contribution from the gold nanoparticle in solution it was show that the lysozyme concentration changes most over time, for samples with AuNP 20KPEG. Lysozyme concentration change for (C) samples that had 5nM or (D) 10 nM gold nanoparticles added.

5.2.2. The relative incorporation of nanoparticles into protein crystals: distribution coefficients

Distribution coefficients (K_D) are used to evaluate the relative ratios of incorporation of two materials. K_D is defined based the ratio of the molar concentrations of nanoparticles (AuNP) and lysozyme (protein) in the crystal (x) and the initial solution (0).

Equation 5.1. Distribution coefficient.

$$K_D = \frac{\frac{[\mathbf{AuNP}]_x}{[\mathbf{Protein}]_x}}{\frac{[\mathbf{AuNP}]_0}{[\mathbf{Protein}]_0}}$$

K_D values are used to determine preferential incorporation of one material over the other; a value of 1 means the materials crystallize equally, resulting in the same ratio of protein to nanoparticles in the crystals as in the initial solution. Values greater than 1 occur when the nanoparticles are incorporated into the crystal at a higher yield and values less than 1 show that the protein was preferentially crystallizing, without the nanoparticles. Studies of hen egg-white lysozyme crystallization with turkey egg-white lysozyme found distribution coefficients near one, illustrative of the fact that these two proteins are chemically highly similar.[25] In this work the concentration of each species in solution was found from the initial absorbance spectrum, while the concentration in the crystal was deduced from the difference between the final solution concentrations and the starting concentrations.

Figure 5.3 shows the K_D for nanoparticle – protein composite crystals formed over a wide range of conditions and polymer chain lengths. Figure 5.3A shows a concentration dependent decrease in the distribution coefficients. As the concentration of nanoparticle-polymer conjugate formed with longer PEG increased from 0.004 to 40 nM ([lysozyme]= 0.25 ± 0.01 mM) the K_D values went from 2 to ~1. The high K_D values at the low concentrations show that the nanomaterials were preferentially incorporating into the crystals, presumably because at lower concentrations the only nucleation sites were at the nanoparticles. However, as the nanoparticle concentration increased the protein and nanoparticle incorporation becomes uniform and resulted in K_D values near 1. While there are variations in the uptake of nanoparticles over the range of conditions, the consistency of distribution coefficient values near 1 suggests that the nucleation object – which is likely a lysozyme associated nanoparticle - is similar thermodynamically to that for free lysozyme.

The nanoparticle to protein ratio also affected the percent yield for protein crystallization; the control sample had 46% of the lysozyme formed into crystals after 3.5 days. Increasing the nanoparticle-polymer conjugate concentration produced crystallization yields greater than 80%. Also, for nanoparticle (5.0 ± 1.0 nM) and protein (0.28 ± 0.02 mM) concentrations an increase in K_D as well as the crystallization yields was seen with increased molecular weight (Figure 5.3B&D). The two shortest molecular weight coated particles have low K_D values of near zero as they have no impact on crystallization. As the chain length of the polymer around the nanoparticle conjugate increased, the distribution coefficients approached 1. We measured K_D values of 1.9, 1.5, 1.5 and 0.8 for 5K, 10K, 20K, and 30K PEG chain lengths.

A closer inspection of the dependence of both the distribution coefficient and crystallization on polymer chain length revealed the crystallization yield as well as the distribution coefficient are sensitive to the total volume occupied by nanoparticle-polymer conjugates. The largest (30,000 MWt) polymer-nanoparticle conjugates occupy 100 times more space in the crystal per particle than the smallest nucleating (5000 MWt) polymer-nanoparticle conjugates. For the same concentration, the more compact 5,000 MWt conjugates coating had a greater incorporation as compared to the much larger 30,000 MWt polymer-nanoparticle conjugate, but a minimal impact on the crystallization yield. Lower concentration of the larger nanoparticle-polymer conjugates also showed the same set of results, a significantly higher K_D values with no increase in crystallization yield. For these larger conjugates, an increased crystallization yield was only observed at relatively high concentrations of nanoparticle conjugates. This suggests that the net volume of the crystal occupied by the nanoparticle-polymer conjugates changes with polymer coating and smaller coated materials may have a higher loading capacity in the crystal.

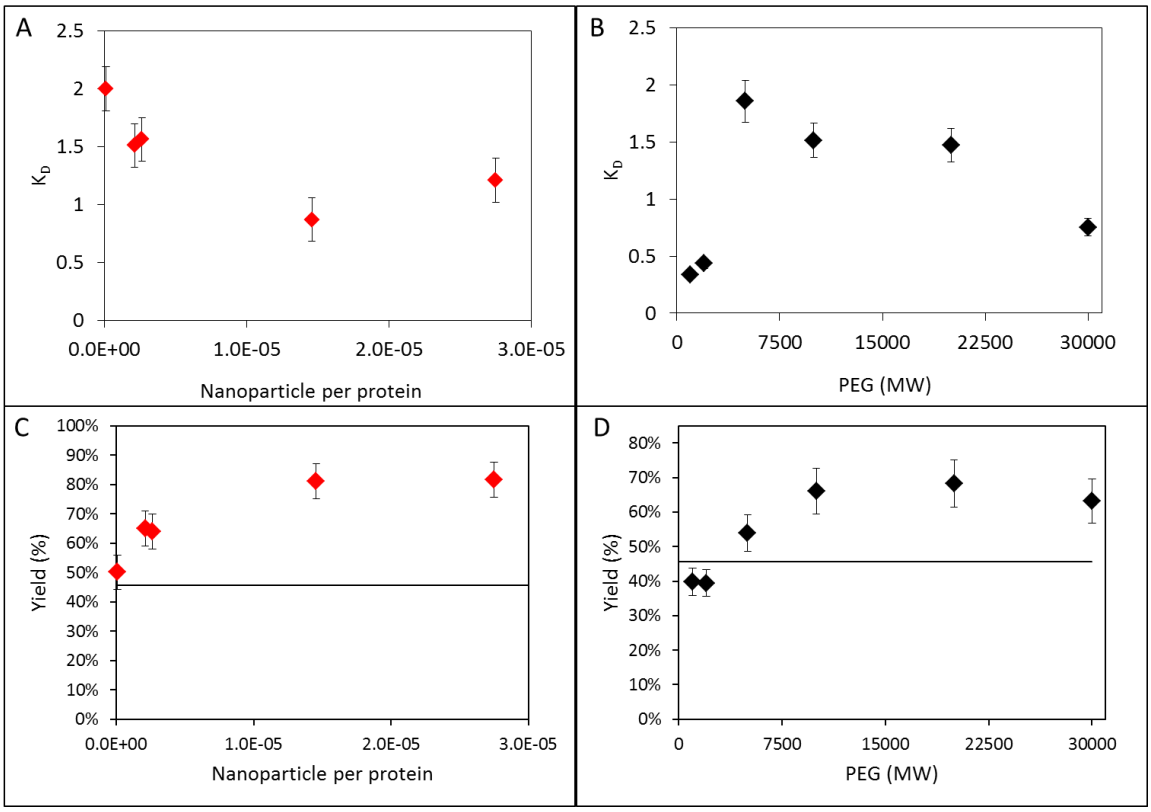

Figure 5.3 Distribution and percent yield graphs

The distribution coefficients (top row) and percent yields (bottom row) for polymer-nanoparticle conjugates in protein crystals. Changes based on (A&C) increases in the AuNP 20KPEG nanoparticle concentration and (B&D) the polymer coating's molecular weight (B&D). Black lines are the percent yield for a control crystal sample.

5.2.3. The incorporation of nanoparticles into protein crystals is a general phenomenon that depends solely on the surface polymer interface

All polymer–nanoparticle conjugates with PEG coatings that have an extension less 50% of the total hydrodynamic diameter of the coiled free polymer in solution are incorporated into composite crystals (See Chapter 4.3.4). Figure 5.4 shows images of the protein crystals produced using polymer–nanoparticle conjugates with AuNP from 5 to 20 nm and PEG coatings from 1K – 30K. The images outlined in blue represent visibly clear crystals and those outlined in red are crystals that appeared red. Every sample with a blue box has a corresponding polymer extension > 50%. This leads to Scheme 1A, showing that short molecular weight polymers which extended >50%, prevent the binding of protein on the surface and form clear protein crystals. Whereas all of the long molecular weight coatings with extensions <50% incorporated and formed protein – nanoparticle composite crystals, which are red. These incorporations are driven by the association of protein with interface of the nanoparticle-polymer conjugates as shown in Scheme 1B. The proteins are able to associate with the polymer layer; this association, which is weak, raises the local concentration of protein around the conjguates and promotes the formation of a crystal nucleus.

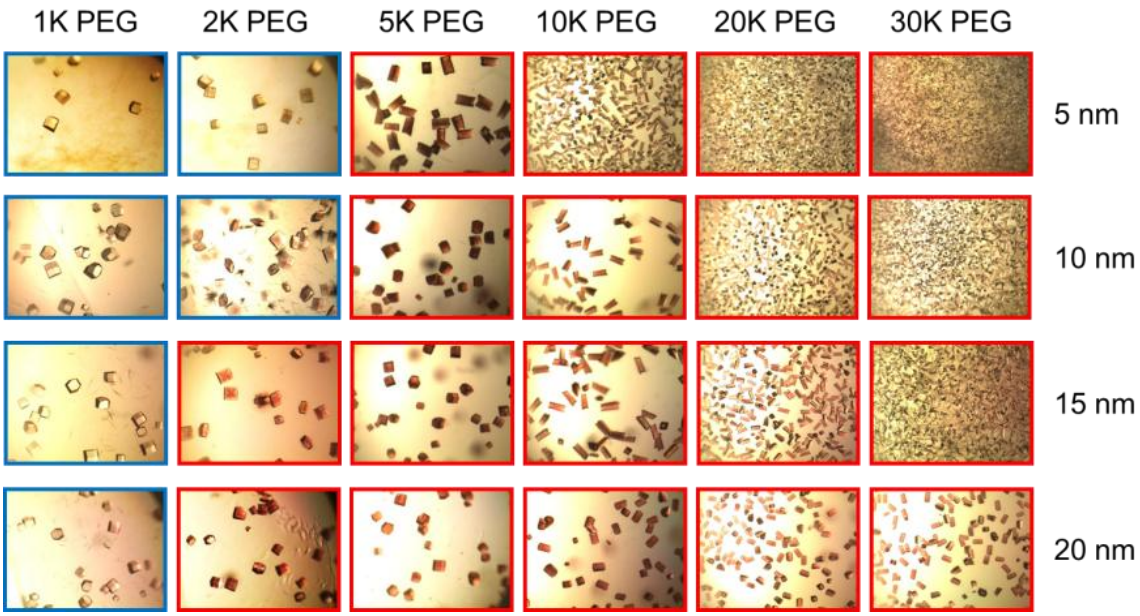

Figure 5.4. PEG chainlength dependence

images

Incorporation of nanoparticles from 5 nm – 20 nm with PEG coatings from 1K to 30K shows a dependence on the polymer extension at the nanoparticle surface for all sizes of gold.

Scheme 5.1 PEG MWt and crystallization

Short molecular weight PEG prevents incorporation long molecular weight PEG promotes protein association and leads to the formation of composite crystals.

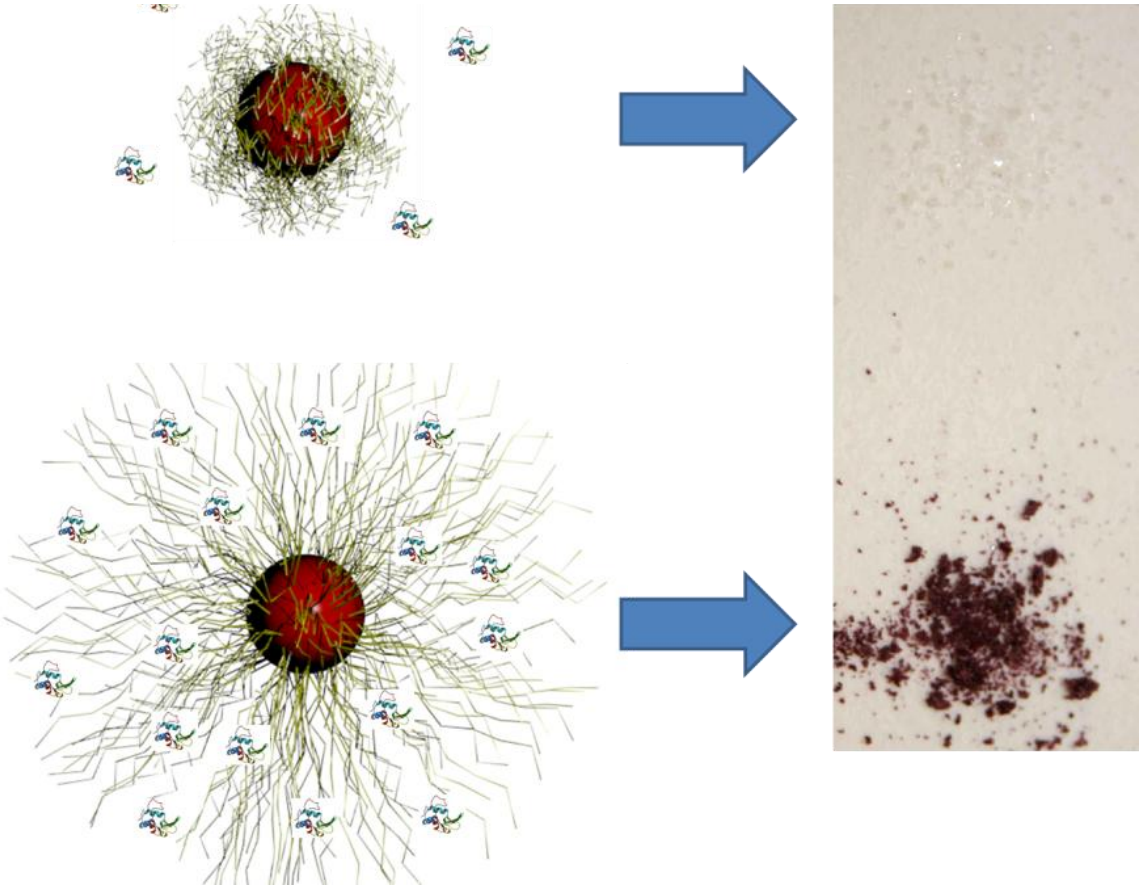

Nanoparticle-polymer conjugates formed from poly(ethylene glycol) larger than 5000 molecular weight are incorporated into protein crystals regardless of their diameter, shape or core composition. Figure 5.4 shows gold nanoparticles with core diameters from 5 to 50 nm coated with 20,000 molecular weight poly(ethylene) glycol. All samples yielded red-colored crystals. Moreover, other shapes of gold nanomaterials: cuboidal, bipyramidal, rods, and high aspect ratio rods, when coated with the same polymer also incorporated (Figure 5.6). Furthermore, nanomaterials composed of silver, iron oxide,

cerium oxide and semiconductor materials, when coated with the 20K PEG were incorporated (Figure 5.7). Therefore, the protein association that drives the formation of composite crystals does not rely on surface charge for electrostatic interactions, or sulfur – gold bonding. Instead the conformation and structure of the polymer coating defines the protein association, and subsequent promotion of nucleation and nanoparticle incorporation.

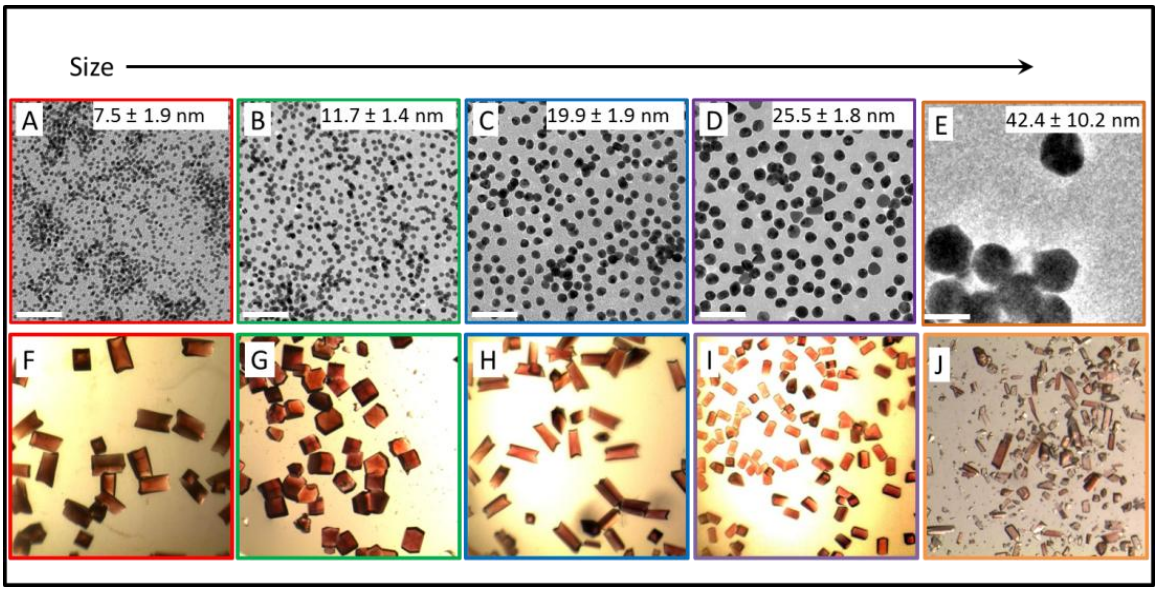

Figure 5.5. Incorporation of nanoparticles based on size.

Incorporation of nanoparticles from 5 nm – 50 nm with PEG coatings of 10K. TEM images of the core gold nanoparticles. All scale bars are 50 nm. Microscope images of the crystals with incorporated nanomaterial.

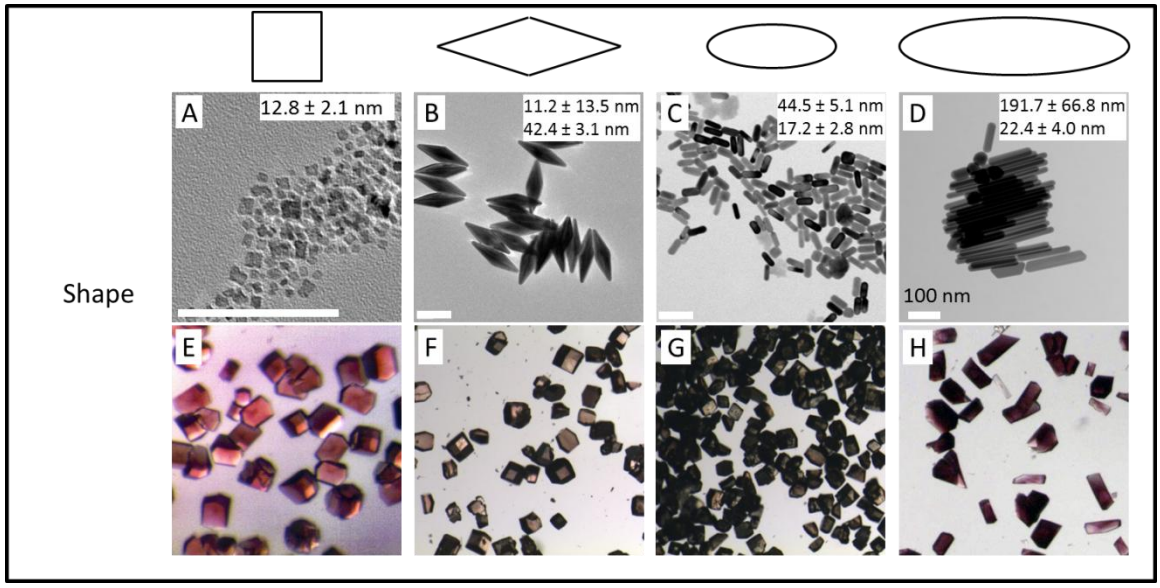

Figure 5.6. Incorporaiton of shape gold nanoparticles.

Top rows: Sketches of the shapes of the nanoparticles determined from the TEM image of the nanoparticles. Bottom row: Images of the composite crystals formed through the incorporation of shaped gold nanoparticles: (A,E) cubes, (B,F) bipyramids, (C,G) rods and (D,H) high aspect ratio rods all with 20K PEG coatings.

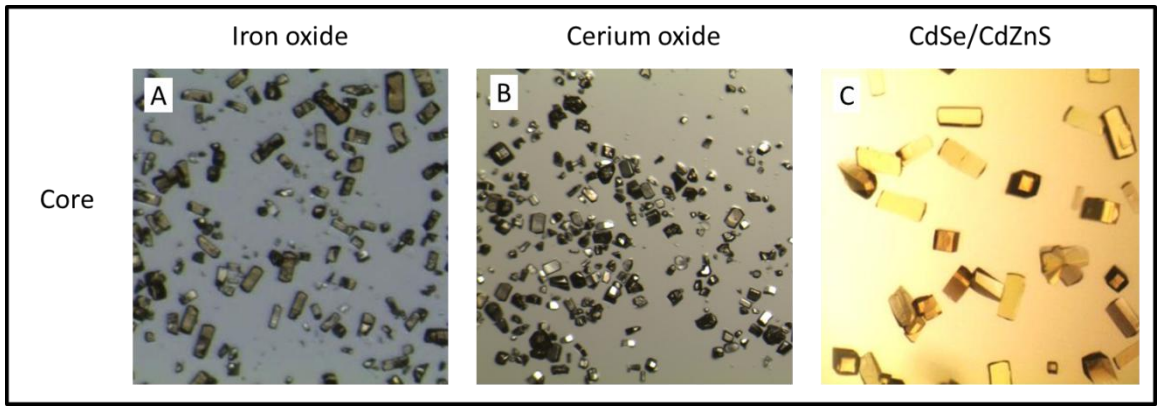

Figure 5.7. Incorporation of other core compostitions.

Composite crystals formed with 20K PEG coated (A) iron oxide, (B) cerium oxide, (C) CdSe/CdZnS quantum dots.

5.2.4. Nanoparticle-protein composites have optical properties similar to that of isolated nanoparticles.

Composite crystals retain the size and shape dependent optical absorbent properties of the incorporated nanomaterials. Absorbance in the visible region of the light spectrum for gold nanoparticles produce the characteristic deep red to purple solutions, which vary depending on size and shape of the particles. Spectral shift in absorbance of gold nanomaterials can yield information about stability, conformation and in our case, distance between particles. Figure 5.8 shows the comparison of the optical absorbance of dried composite crystals formed using 10 nm, 15 nm and 20 nm spherical gold nanoparticle-polymer conjugates as compared to the absorbance of the nanomaterials alone dispersed in solution. The peak positions are shifted by 29, 28, and 21 nm, respectively. These shifts in the plasmon resonance are likely due to the difference in the refractive index (RI) between water and a protein crystal.[26]

We analyzed these peak shifts quantitatively for the gold nanorod (AunRod) composite protein crystals to confirm that the shifts were due solely to refractive index changes and not to cooperative interactions between metal nanoparticles. The shaped gold nanoparticles have interesting absorbance spectrum properties; the width and length of the rod have different peak absorbance positions resulting in two plasmon resonances in the absorbance spectrum. Figure 5.8D shows the absorbance of a gold nanorod sample; the smaller peak around 520 nm is the transverse peak and the larger peak centered around 750 nm is the longitudinal peak. The shape, relative intensities and position of the transverse peak were conserved in the AunRod composite crystal absorbance

spectrum; however the longitudinal peak position shows a shift of 33 nm. From the literature, the expected shift due to refractive index changes is 170 nm per RI unit.[27] We used a RI for water of 1.33 for the initial solution conditions; for the lysozyme crystal we took a refractive index of 1.56 ± 0.01.[28] This data predicts a peak shift between 32 and 38 nm, in good agreement with the measured value. This suggests that the nanorods are non-interacting and non-aggregating in the crystal, and thus separated by at least twice their diameter.

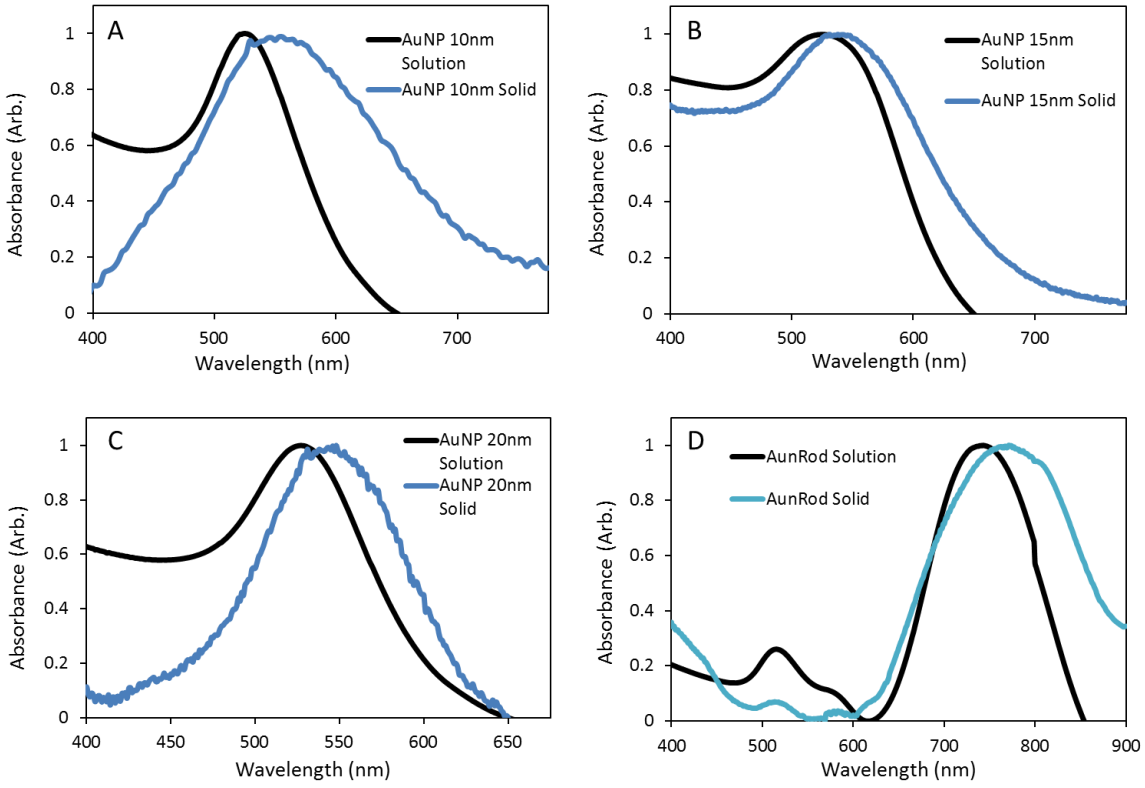

Figure 5.8 Optical absorbance spectrums

Optical absorbance spectrum of solutions (black lines) and composite crystals dried out of solution (blue lines) for gold nanoparticles spherical with diameters of (A) 10 nm, (B) 15 nm, and (C) 20 nm, and (D) gold nanorods with an aspect ratio of 2.6 ±0.3.

Quantum dot composite crystals have a slight blue shift in absorbance and an enhanced relative fluorescence over their materials dispersed in solution. Figure 5.9, shows an image of a UV illuminated solution containing quantum dots and quantum dot composite crystals accumulated on the wall of a cuvette. Both materials are fluorescent at a similar wavelength. The optical absorbance data in Figure 5.9B shows the solid quantum dot composite crystal sample has several additional peaks and a blue-shifted exciton absorption. Like the resonances of the metallic particles, the quantum dot absorption peak is somewhat sensitive to the local refractive index which is likely the cause of the modest blue shift in exciton absorption. The peaks to the red of the primary excitonic feature are more unusual, and could be attributed to absorbances from the crosslinked crystals or charge transfers between quantum dots.[29]

Unlike the optical absorption which is different in the crystal as opposed to the solution, the fluorescence remains identical in its primary emission wavelength (Figure 5.9C). What is different, however, is the relative emission intensity of the solid protein crystals. This value was found by normalizing the emission collected from a set of crystals or a solution to the maximum optical absorption of the same sample; this data reveals that the protein-quantum dot crystals have a 15-fold increase in their effective quantum yield. This is a striking and potentially important finding as maximizing the quantum yields from these materials has been of major interest for decades.[30]

Two factors need to be controlled for future experiments in order to confirm this finding. First, the samples used have an irregular distribution of crystals on the wall of the cuvette and provide variability in the sampling area. This could lead to the absorbance and

fluorescence data being collected on different areas containing different population of crystals, which would mean the normalization for the absorbance intensity would be inaccurate. Another contribution to the difference could have arisen from reflection off of the crystal surfaces. In a fluorescence collection this could have favored emission at ninety degree collection angles. Further work on the linear and non-linear optical properties of these composite materials should be pursued, preferably on a single crystal.

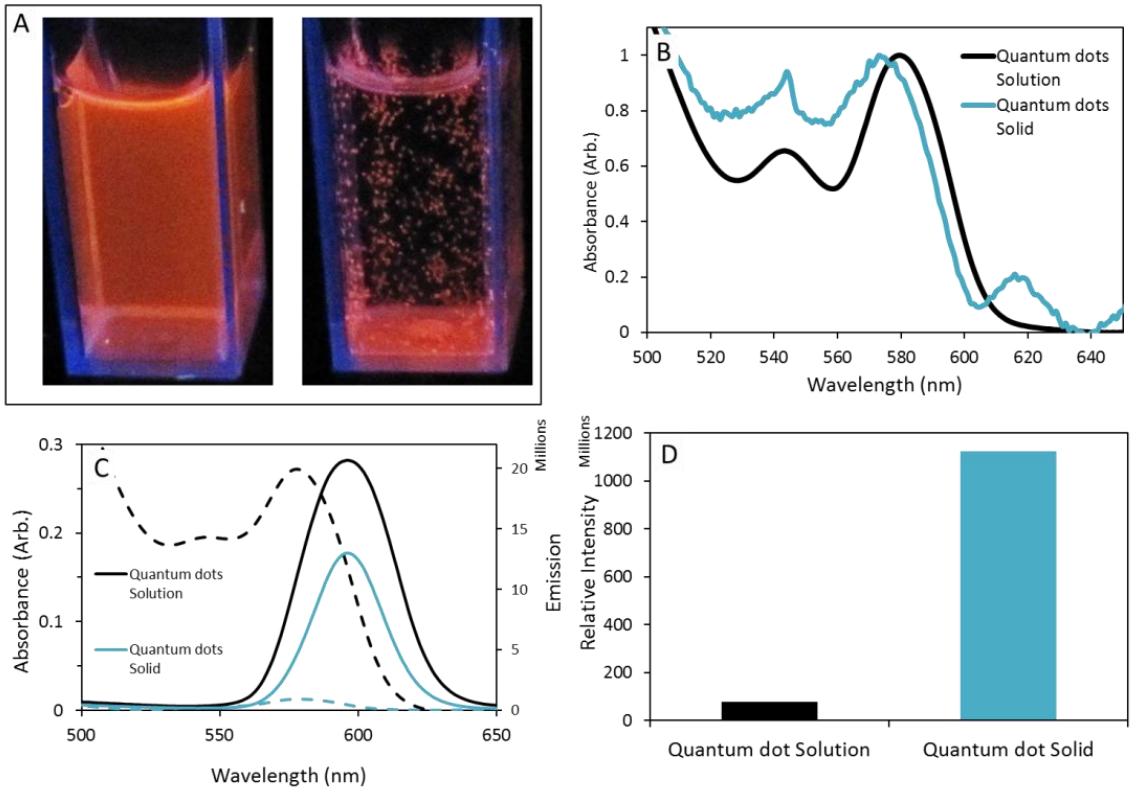

Figure 5.9 Optical properties of crystals containing quantum dots.

Optical properties of composite crystals containing quantum dots. (A) Both the solution and quantum dot composite crystals are fluorescent under UV light. (B) The optical absorbance spectrum of solutions (black lines) and composite crystals (blue lines) dried out of solution. (C) Emission profiles for solution of disperse quantum dots and composite crystals grown on the wall of the cuvette. (D) Relative emission intensity (Emission/Absorbance) for the composite crystal sample is high.

5.2.5. Magnetic nanoparticles in protein crystals have novel behavior

Figure 5.10 A and B shows the accumulation of composite crystals containing magnetic nanoparticles at the site of a small hand held magnet. While this is similar to that seen for the isolated particles, more quantitative studies of the magnetization of the composites

detect substantial differences between the individual magnetic nanoparticle behavior and the behavior in the protein crystal composite. Figure 5.10 C and D show how the magnetization of a collection of composite protein crystals varies as a function of the applied magnetic field. Unlike isolated nanoparticles, or nanoparticles loaded into polymers, these samples do not show any coercivity at low temperatures. They are effectively non-magnetic. Based on the lack of coercivity for the crystals the particles must be non-interacting, separated by more than twice their diameter. Our current hypothesis for why they showed magnetic response in solution and not on analysis is that for this analysis the protein crystals had to be fully dried after cross-linking; the lack of any internal solvent is thus one difference between these samples. There is some suggestion that the magnetic properties of nanoparticles constrained in a porous matrix require the coordination of their magnetic spin with associated solvent molecules.[31,32]

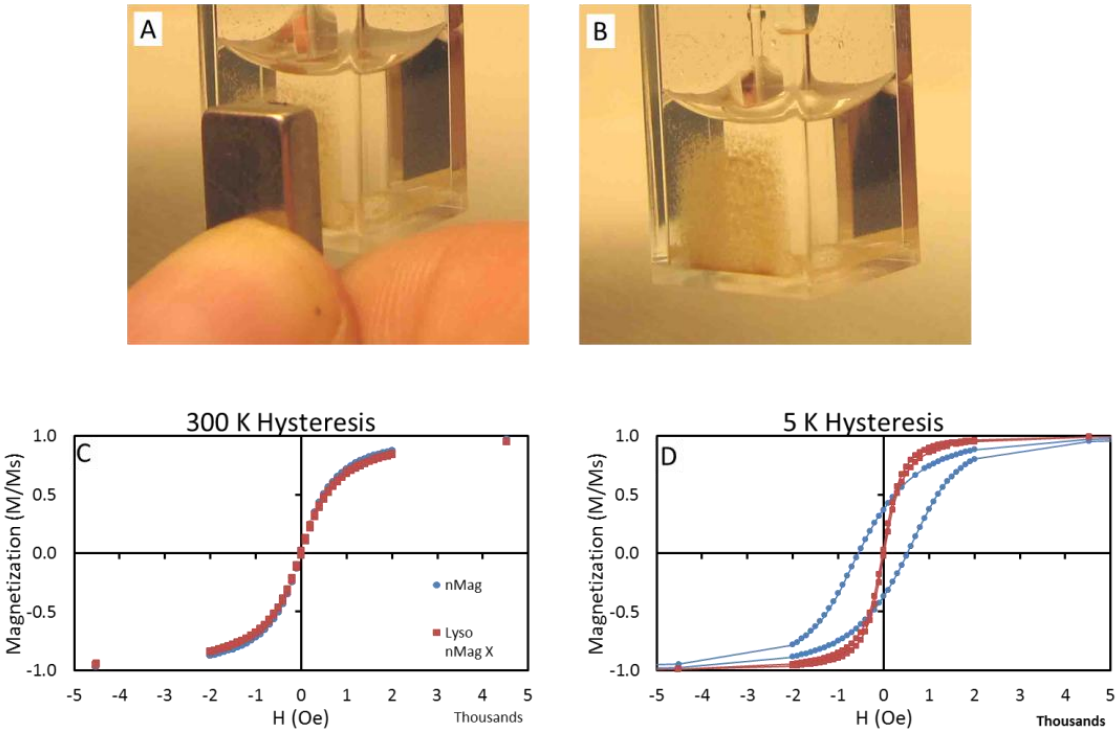

Figure 5.10 Magnetic properties of composite crystals

Magnetic properties of composite crystals containing nanomagnetite. (A&B) The application of a hand held magnet to the solution of composite crystals results in the accumulation of the materials at the site of the magnet. Magnetic response (C) at high temperature and (D) low temperature show superparamagnetic behavior for nanoscale magnetite alone (blue lines) and no magnetic susceptibility for the composite crystals (red lines).

5.3. CONCLUSION

Nanoparticles coated with PEG molecules in a mushroom conformation are incorporated into protein crystal lattices. This observation is quite general and a wide range of nanoparticle diameters, shapes and compositions could be concentrated in the growing

lattice of lysozyme. The composite crystals retain the properties of the incorporated nanomaterials; for quantum dots there may be some cooperative properties that enhance optical emission. In the case of iron oxide particles the low temperature magnetization properties are quite different than bulk nanoparticle powders.

5.4. REFERENCES

(1) Nath, N.; Chilkoti, A. *Analytical Chemistry* **2001**, *74*, 504.

(2) Martins, J. d. R.; Batista, R. J. C.; Chacham, H. l. *Journal of the American Chemical Society* **2010**, *132*, 11929.

(3) Lux, K. W.; Rodriguez, K. J. *Nano Letters* **2006**, *6*, 288.

(4) Xiong, Y.; McLellan, J. M.; Chen, J.; Yin, Y.; Li, Z.-Y.; Xia, Y. *Journal of the American Chemical Society* **2005**, *127*, 17118.

(5) French, R. W.; Milsom, E. V.; Moskalenko, A. V.; Gordeev, S. N.; Marken, F. *Sensors and Actuators B: Chemical* **2008**, *129*, 947.

(6) Takeda, Y.; Kondow, T.; Mafuné, F. *Chemical Physics Letters* **2011**, *504*, 175.

(7) Ding, Y.; Chen, M.; Erlebacher, J. *Journal of the American Chemical Society* **2004**, *126*, 6876.

(8) Kechrakos, D.; Trohidou, K. N. *Applied Physics Letters* **2002**, *81*, 4574.

(9) Nakata, K.; Hu, Y.; Uzun, O.; Bakr, O.; Stellacci, F. *Advanced Materials* **2008**, *20*, 4294.

(10) Nie, Z.; Petukhova, A.; Kumacheva, E. *Nat Nano* **2010**, *5*, 15.

(11) Pileni, M. P. *The Journal of Physical Chemistry B* **2001**, *105*, 3358.

(12) Taleb, A.; Petit, C.; Pileni, M. P. *The Journal of Physical Chemistry B* **1998**, *102*, 2214.

(13) Fendler, J. H. *Chemistry of Materials* **1996**, *8*, 1616.

(14) Weiner, S.; Wagner, H. D. *Annual Review of Materials Science* **1998**, *28*, 271.

(15) Pum, D.; Neubauer, A.; Györvary, E.; Sára, M.; Sleytr, U. B. *Nanotechnology* **2000**, *11*, 100.

(16) Okuda, M.; Kobayashi, Y.; Suzuki, K.; Sonoda, K.; Kondoh, T.; Wagawa, A.; Kondo, A.; Yoshimura, H. *Nano Letters* **2005**, *5*, 991.

(17) McMillan, R. A.; Paavola, C. D.; Howard, J.; Chan, S. L.; Zaluzec, N. J.; Trent, J. D. *Nat Mater* **2002**, *1*, 247.

(18) Coomber, D.; Bartczak, D.; Gerrard, S. R.; Tyas, S.; Kanaras, A. G.; Stulz, E. *Langmuir* **2010**, *26*, 13760.

(19) Park, S. Y.; Lytton-Jean, A. K. R.; Lee, B.; Weigand, S.; Schatz, G. C.; Mirkin, C. A. *Nature* **2008**, *451*, 553.

(20) Prabhu, V. M.; Hudson, S. D. *Nat Mater* **2009**, *8*, 365.

(21) Falkner, J. C.; Turner, M. E.; Bosworth, J. K.; Trentler, T. J.; Johnson, J. E.; Lin, T.; Colvin, V. L. *Journal of the American Chemical Society* **2005**, *127*, 5274.

(22) Wei, H.; Wang, Z.; Zhang, J.; House, S.; Gao, Y.-G.; Yang, L.; Robinson, H.; Tan, L. H.; Xing, H.; Hou, C.; Robertson, I. M.; Zuo, J.-M.; Lu, Y. *Nat Nano* **2011**, *6*, 93.

(23) Kasyutich, O.; Sarua, A.; Schwarzache, W. *Journal of Physics D: Applied Physics* **2010**, *43*, 179801.

(24) Abe, S.; Tsujimoto, M.; Yoneda, K.; Ohba, M.; Hikage, T.; Takano, M.; Kitagawa, S.; Ueno, T. *Small* **2012**, n/a.

(25) Schutt, K. J.; Gosavi, R. A.; White, D. B.; Schall, C. A. *Journal of Crystal Growth* **2009**, *311*, 4062.

(26) Chen, H.; Kou, X.; Yang, Z.; Ni, W.; Wang, J. *Langmuir* **2008**, *24*, 5233.

(27) Mayer, K. M.; Lee, S.; Liao, H.; Rostro, B. C.; Fuentes, A.; Scully, P. T.; Nehl, C. L.; Hafner, J. H. *ACS Nano* **2008**, *2*, 687.

(28) Fredericks, W. J.; Hammonds, M. C.; Howard, S. B.; Rosenberger, F. *Journal of Crystal Growth* **1994**, *141*, 183.

(29) Simserides, C. D.; Hohenester, U.; Goldoni, G.; Molinari, E. *physica status solidi (b)* **2001**, *224*, 745.

(30) Crosby, G. A.; Demas, J. N. *The Journal of Physical Chemistry* **1971**, *75*, 991.

(31) Maspoch, D.; Ruiz-Molina, D.; Wurst, K.; Domingo, N.; Cavallini, M.; Biscarini, F.; Tejada, J.; Rovira, C.; Veciana, J. *Nat Mater* **2003**, *2*, 190.

(32) Ferey, G. *Nat Mater* **2003**, *2*, 136.

Chapter 6

THE ARRANGEMENT OF NANOPARTICLES WITHIN PROTEIN CRYSTALS

6.1. INTRODUCTION

At the end of Professor Alivisatos' 1996 article in Science he stated, "New physics and chemistry are sure to be discovered as [controlled arrangements of nanostructures in] complex assemblies are investigated."[1] Indeed the arrangement of inorganic nanomaterials of all types has led to the discovery of interesting properties, above and beyond the size dependent phenomena that have been intriguing investigators for years.

*Work performed within this chapter is the collaborative efforts of me and members of the Colvin lab, Hafner lab and Shamoo lab. Courtney Payne (Hafner lab) provided all of the PEGylated shaped gold nanoparticles, Dr. Carolina Avendano (Colvin lab) ran powder XRD, acted as a liaison between myself and the Advance Photon Source for synchetron powder XRD collection, Zuzanna Lewicka (Colvin lab) sputter coated and acquired all SEM images, Lindsey Anderson (Hafner lab) ran all single crystal polarization dependent spectroscopy experiments, Kasia Walkiewicz (Shamoo lab) provided training for crystallization techniques, and ran and processed single crystal diffraction data. In addition, I had help from an intern: Michael Lillierose (composite crystal preparation).

Architectures of nanoparticles generate unique cooperative and ensemble dependent properties. For clarity, cooperative properties will be defined as those driven by interactions between two adjacent nanomaterials, while ensemble properties are those based on interactions between all nanomaterials within three dimensional organized arrays.

The cooperative effects have been studied extensively for two dimensional arrangements of metallic, semiconducting and magnetic nanomaterials. The distance between particles plays a major role in the demonstration of cooperative effects. Generally, particles closer than two times their diameter are coupled altering expected characteristics or producing new properties. Two interacting spherical metallic nanoparticles have predictable shifts in the spectral absorbance peaks based on the particles' diameters, interparticle distance and the polarization of the incident light.[3] Anisotropic metal nanomaterials' cooperative properties are additionally effected by the symmetry and orientation of the particles relative to one another.[4] There is a strong distance dependence for the coupling effects of quantum dots, where closer particles have decreased photoluminescence intensities due to increased decay rates and charge transfers.[5-7] Like quantum dots, close interparticle distances for magnetic nanomaterials lead to loss of their size dependent properties; however, being too separated will lead to the loss of the materials ability to respond to a magnetic field.[8-10] From these studies in two dimensional systems an understanding of the parameters for interactions between nanoparticles necessary to produce measurable changes in spectral absorbance, emission and magnetic response has been advanced.

Unfortunately, ensemble properties are not as well understood and can differ from the cooperative properties seen for the same materials. Metallic nanoparticle ensembles show greater spectral shifts, but surprisingly there are also decreased bandwidth for 3D arrangements, over the 2D structures.[11,12] The photoluminescence intensity for superstructures of quantum dots was shown to increase with the addition of layers in a 3D arrangement.[13] However, most of the reported ensemble properties are for multiple layers of self-assembled hexagonal-close-packed lattices of nanoparticles, with little to no long range control over the distance between particles or variations in their arrangement. By utilizing biomolecules for the spatial organization of nanoparticles, the distance and coordination of nanoparticles can be controlled in three dimensions and their properties explored to obtain a better understanding of the ensemble effect within disperse arrays of nanoparticles.

Here we use four methods to determine the arrangement of nanoparticles within a protein crystal: qualitative imaging and quantitative approaches of diffraction, high magnification visualization and polarization dependent single crystal spectroscopy. Light and confocal microscopy techniques were used to assess general incorporation based on the uniformity and distribution of observable color or fluorescence within the crystals. More quantitative approaches were aimed at determining the actual distances and spatial arrangement of the nanomaterials; which is exceedingly difficult given that the nanoparticles are tens of nanometers and the crystals are greater than 100 μm, effectively creating features that span size differences of four orders of magnitude. Unfortunately, diffraction patterns were unable to provide conclusive evidence of the nanoparticle

arrangement. However, the electron microscopy techniques (TEM and SEM) were effective means for the visualization of some of the nanoparticles. TEM successfully resolved smaller nanoparticles, but could only be used on small areas or thin sections of the crystal. SEM images were able to provide more useful information and allow determination of the spatial arrangements because it could be used to image both large areas and small nanoparticles on a single surface of the crystals. Images from both electron microscope techniques showed a distribution of unaggregated nanomaterials throughout the crystal, with regions of alignment for samples containing anisotropic particles. Nanorods on the surface and interior of the crystal had less than a 20 degree deviation from the average angle of the sample and aligned perpendicular to the c-axis of the lysozyme crystals. Polarization dependent spectroscopy confirmed these results showing long range alignment throughout the protein crystal for anisotropic materials, based on a significant decrease in the optical absorbance at their longitudinal peak with changes in the polarization of incident light.

6.2. RESULTS AND DISCUSSION

6.2.1. Microscopic examination

The arrangement of nanoparticles within any three dimensional array is of the utmost importance, because the regularity and interparticle distance are the major factors influencing the occurrence of cooperative and ensemble properties for arrays of nanoparticles. Nanomaterials incorporated into protein crystals show uniform coloration and intensity when, assessed visually, using light or confocal microscopy. Figure 6.1,

shows the {110} and the {101} faces for control crystals, gold nanoparticle composite crystals imaged by a light microscope and quantum dots composite crystals imaged by a confocal microscope. The nanoparticle distributions in these images appear to be uniform from one edge of the crystals to the other. For the incorporation of most polymer-nanoparticle conjugates such homogeneous colors were typical. However, a more controlled distribution of materials could be obtained by altering the nanoparticle – protein associations or the crystallization conditions.

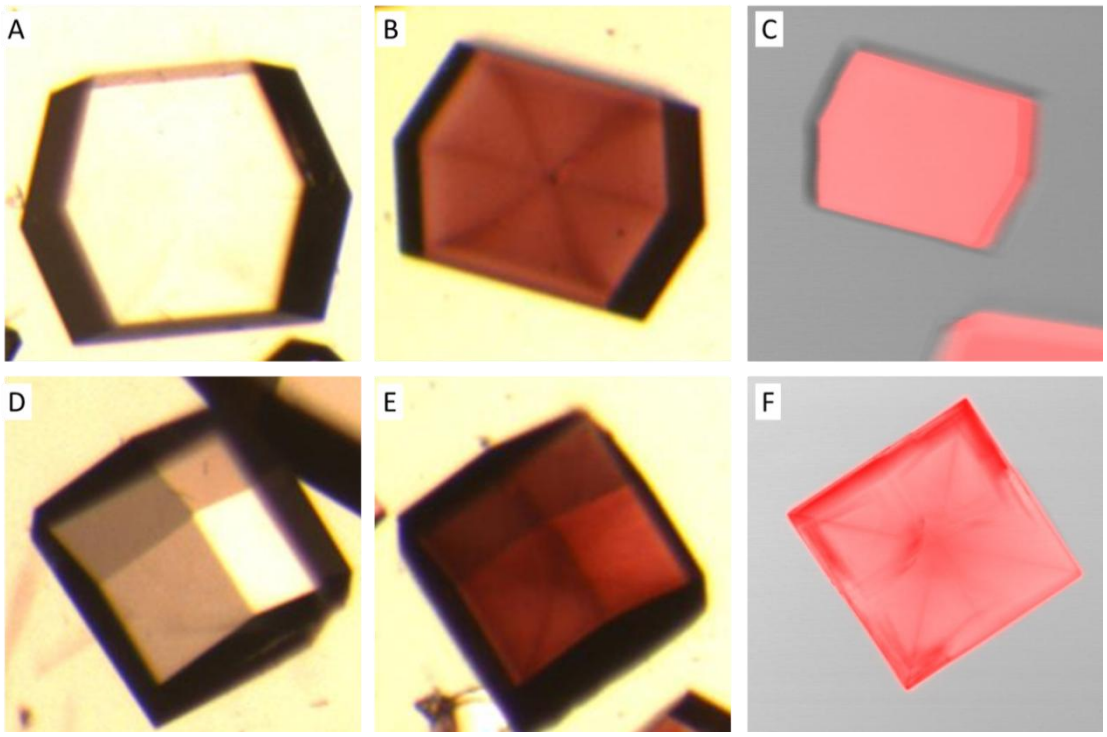

Figure 6.1 Microscopic images of lysozyme crystals

Light microscope (A,B,D,E) and confocal microscope (C,F) images of lysozyme crystals {101} planes (A-C) and {110} (D-E) for control crystals formed without nanoparticles (A,D), AuNP_5KPEG (B,E), and quantum dot (C,F) composite crystals.

More complicated macroscopic architectures could be formed including what we term selective domain crystals, (Figure 6.2A) or core / shell structures (Figure 6.2B). Figure 6.2C, from ref [2], shows the sectors of a lysozyme crystal; there are 8 {101} and 4 {110}. Takeda et. al. produce similar architectures and they postulated that the distributions occurred due to electrostatic associations between poly(acrylic acid) coated onto gold nanoparticles (AuNP_PAA) and lysozyme.[2] Similarly, short molecular weight PEG nanoparticle-conjugates that are not fully sterically stabilized by poly(ethylene) glycol can be rendered stable while still maintaining a net negative surface charge. These states have mainly been seen for short molecular weight polymer coated nanoparticles, after being stored for > 1 month without any excess PEG in solution. Through dynamic equilibrium, the coating materials are depleted creating a surface charge for electrostatic associations with lysozyme. Takeda et al, reported that electrostatic associations are greater with the crystal {101} surface than the {110} surface due to differences in the growth kinetics between the faces.[2] These crystals show the typical "hourglass" coloration pattern from the selective regions where incorporation occurs.

Another selective incorporation formation occurs when nanoparticles are restricted only to the core of the protein crystal (Figure 6.2B); this geometry is fairly simple to achieve simply by diluting the nanoparticle concentration after crystal growth has started or starting with low initial concentrations of nanoparticles that deplete as the crystals grow. The crystals shown in Figure 6.2B were formed from a concentration gradient which was produced when large, high aspect ratio gold nanorods slowly settled out of solution. The scheme in Figure 6.2D shows that core/shell crystal form only at the top of the vial,

where the nanoparticle concentration was depleted the fastest. Low initial concentrations of nanoparticles were also used to form crystals with a higher concentration of nanoparticles at the core. Because of the selective uptake of nanoparticles the concentration of nanoparticles in the center are greater than the edges however the distribution between core and shell for these samples were more diffuse.

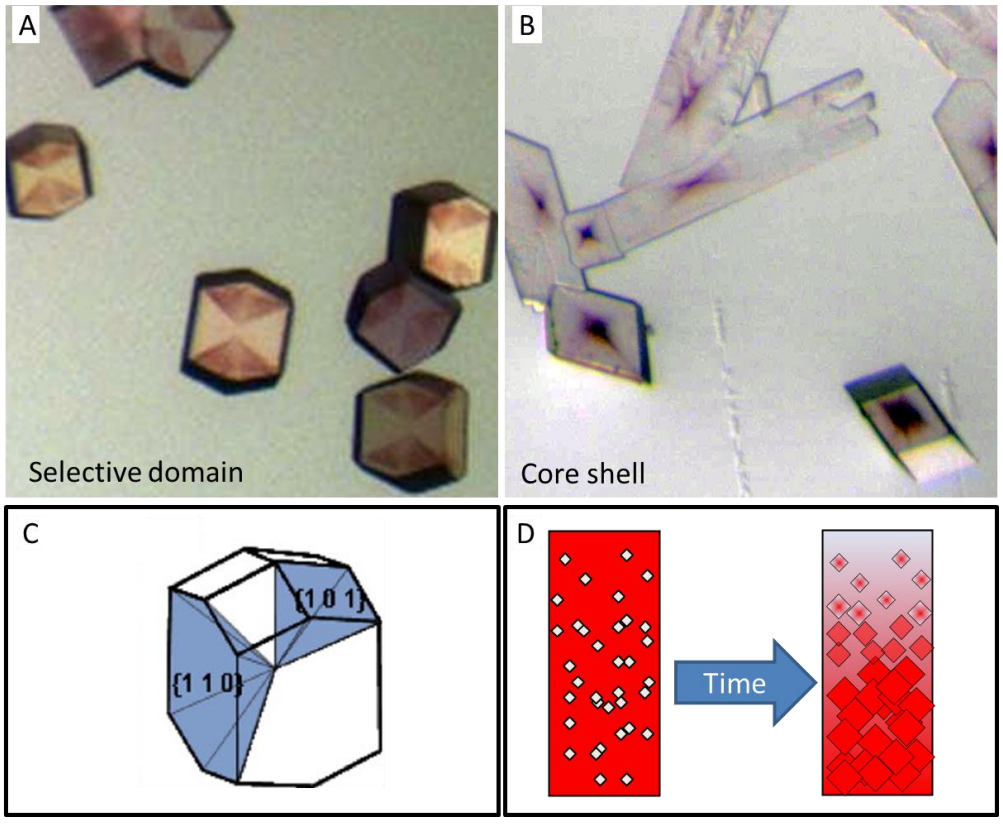

Figure 6.2. Selective domain and core/shell distribution of nanoparticles

Uneven incorporations, (A) selective domain composite crystals produced for under coated AuNP_2KPEG nanoparticles. (B) Core /shell distributions have nanoparticles at the core and clear outer edges of the crystals. (C) Preferential incorporation into the 8 {101} face results in an hour glass shaped red color, image from ref [[2]]. (D) Core / shell crystals form when the nanoparticle concentration is depleted out of solution, through processes such as sedimentation.

6.2.2. Diffraction analysis

While micrographs provide qualitative information about the distribution of nanomaterials in macroscopic crystals, they do not show the spacing or arrangement of the particles on a nanometer scale. The first approach used to determine the crystallographic arrangement of nanoparticles was diffraction. Powder and single crystal X-ray diffraction patterns were collected for four crystal samples: one control lysozyme without any nanoparticles, and three composite crystals formed with gold nanoparticles coated with 10,000 molecular weight PEG. The first two composite crystal samples were prepared with 10 nm spherical particles at two loading concentrations: a low concentration, 1 nM and a high concentration, 10 nM. Additionally, composite crystals saturated with gold nanorods (AunRod) were also analyzed.

The diffraction patterns collected on all protein crystals showed reflections consistent with the lysozyme crystal lattice. For all four samples the lysozyme structure remained identical in terms of the symmetry point group and unit cell dimensions. The only observable changes with the addition of gold nanoparticles were decreases in crystal diffraction quality as seen in the decreased resolution limit and increased mosaicity. Table 1 is a comparison of the diffraction data collected for a control crystal and the high concentration protein crystal-nanoparticle composite. The resolution limits for the control, AuNP_[low], AuNP_[high], and AunRod crystals. were 1.60, 1.60, 1.60 and 2.0 Å and the mosaicity values were 0.55, 1.1, 2.76 and 0.8, respectively.

Table 6.1 Summary of single crystal diffration data collection statistics

Table 1. Summary of Data Collection Statistics[a]

	Lysozyme Control		Lysozyme + AuNP_[high]	
Wavelength (Å)	1.54		1.54	
Resolution (Å)	39.39 - 1.60	(1.66 - 1.60)	38.77 - 1.60	(1.66 - 1.60)
Space group	$P4_32_12$		$P4_32_12$	
Unit Cell (Å)	a = b =78.77		a = b = 77.55	
	c = 36.91		c = 37.01	
	α = β = γ = 90.0°		α = β = γ = 90.0°	
Observed reflections	90882		85033	
Unique reflections	14954		15161	
Mosaicity	0.55		2.76	
Average redundancy	6.08	(5.57)	5.02	(1.28)
Completeness (%)	94.3	(78.6)	98.3	(98.6)
R_{merge}[b] (%)	4.8	(14.8)	12.3	(55.6)
Output <I/sigI>	22.5	(9.3)	4.3	(1.3)

[a] Values for the last shell are in parenthesis
[b] $R_{merge} = \Sigma \left| I - \langle I \rangle \right| / \Sigma I$, where I is measured intensity for reflections with indices of hkl.

Powder x-ray diffraction was also explored for these materials in the hopes of determining low angle peaks that might signify crystallographic arrangement of nanoparticles. Samples for powder diffraction were first cleaned and crosslinked, then further purified and dried; finally they were smashed or ground to a fine powder. Without the additional cleaning step only peaks arising from the buffer salts used in the crystallization growth media were observed. Powder diffraction data was first collected on a Rigaku XRD with a copper Kα source and a zero background holder. Figure 6.3 shows the comparison of the lysozyme control pattern and the AuNP_[high] pattern. The large two theta angles show the pattern for crystalline gold, which confirms the presence

of the nanoparticles in the samples. At low two-theta angles there are peaks that are consistent with those observed for the cross linked lysozyme crystal controls; these peaks showed no significant shifts, as shown in table 2.[14] However, the amount of noise and the interference from the small angle X-ray scattering made resolving the protein peaks difficult.

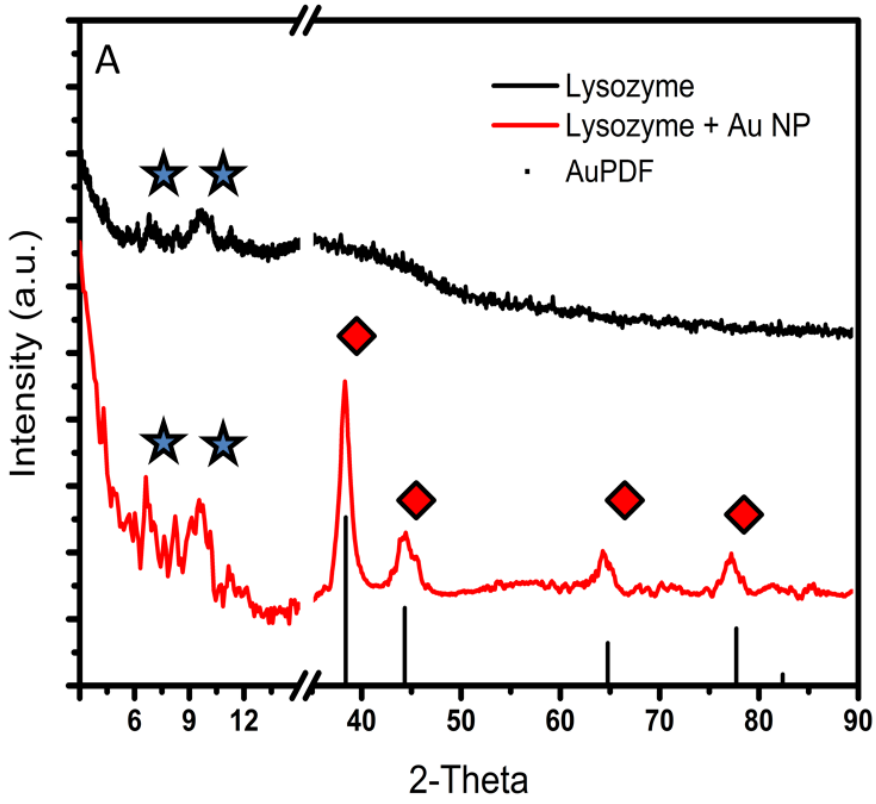

Figure 6.3 Powder X-ray diffraction data

Powder X-ray diffraction data (offset for clarity) collected for lysozyme control crystals (black line) and AuNP_[high] composite crystals. Lysozyme peaks are seen in the low two-theta angles (blue stars) and gold peaks are seen in the larger two-theta angles (red diamonds).

Table 6.2 Lattice spacing for lysozyme

D-space crosslinked HEWL	Associated Lattice Plane	Lysozyme Control Crystal	Lysozyme + AuNP 20K PEG
3.12	111	ND	ND
2.51	211	2.05	2.10
1.31	600	1.34	1.34
1.2	630	0.94	0.94
NR	NR	0.80	0.80

ND = None detected
NR = Not reported

To obtain better powder diffraction data at the low two theta angles, samples were sent to the Advanced Photon Source at Argonne National Laboratories, where the diffraction data was collected on a syncetron beam line for angles from 1 – 42 degrees. The series of peaks, shown in Figure 6.4A, at the low two-theta were similar for all four samples and closely matched in position and intensity. In the higher two-theta the incorporation of gold nanoparticles was again confirmed by the presence of concentration dependent gold peaks in the composite crystal samples.

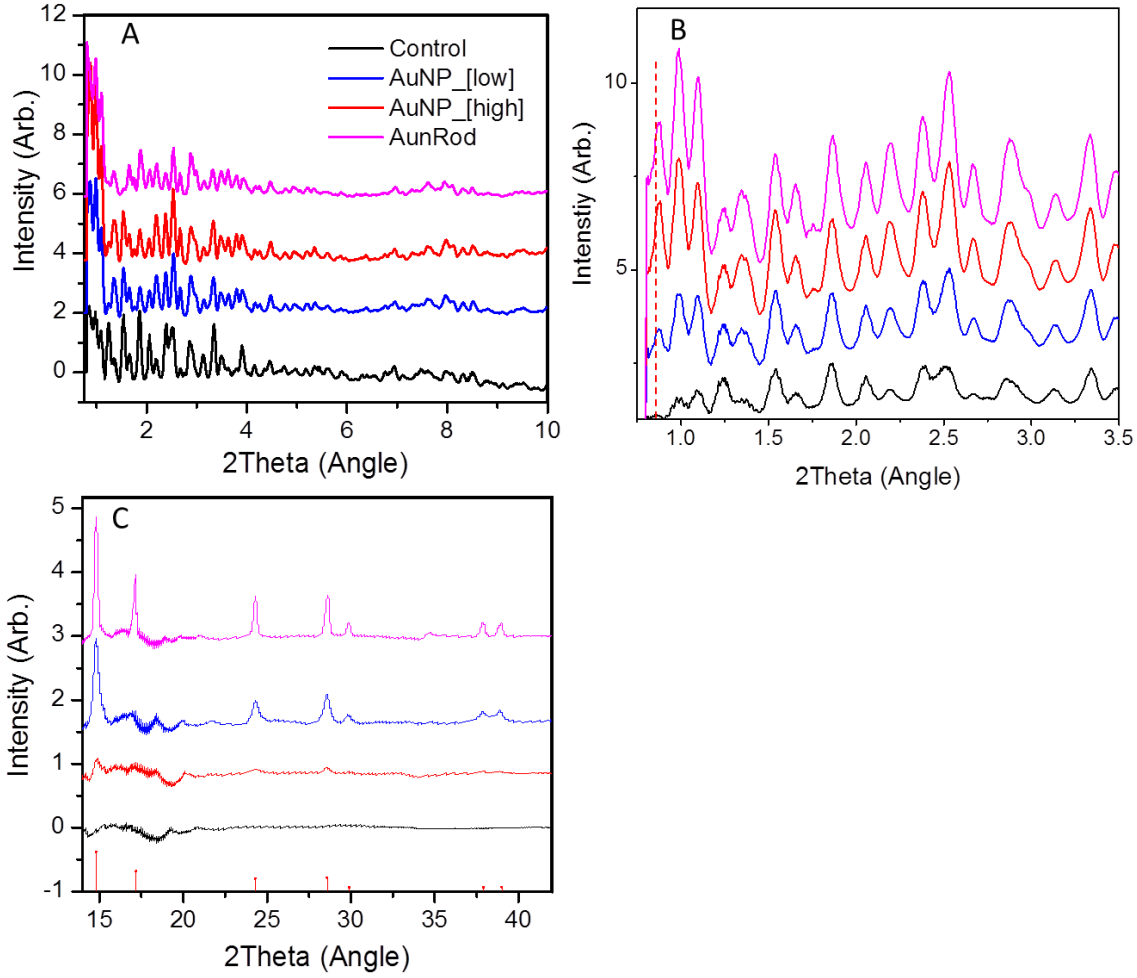

Figure 6.4 High resolution-low angle powder X-ray diffraction data

Data shown was collected at 20eV on the BM-1 rapid access powder diffraction beam line. Samples are lysozyme control crystals (black), AuNP_[low] (blue), AuNP_[high] (red), and AunRod (purple) composite crystals (baseline subtracted and offset for clarity). (A&B) Low angle 2theta data show peaks that match well to the lysozyme control crystals. (B) Zoomed in on the lowest 2theta region of graph A, the red dotted line indicates the only peak that is absent in the control sample and increases with gold concentration in this region of the spectra. (C) High angle 2theta have concentration dependent gold peaks.

Based on the diffraction data, all peaks were identified as either lysozyme or gold and did not indicate the placement of particles within the crystal. If there were regular patterns of

nanoparticles within the protein lattice, then very small two-theta peaks may be present. A careful examination of Figure 6.4 (B) shows a low angle peak just above 1 that grows with nanoparticle loading volumes. To further examine this region requires larger distances between the sample and detector with better resolution at low two-theta position. Currently, there is too much interference from the lysozyme diffraction to draw and conclusions regarding the nanoparticle arrangement using diffraction data.

6.2.3. Electron microscopy

Electron microscopes were used at high magnification to detect the presence and arrangement of nanoparticles within the protein crystal composites. Transmission electron microscopy (TEM) was used with an analytical scanning imaging device (ASID) to perform scanning transmission electron microscopy (STEM) imaging in high angle angular dark field (HAADF) to image the thick composite crystals and detect the nanoparticle positions. Figure 6.5 shows the HAADF images of AuNP_[high] crystals at two magnifications. The nanoparticles are distributed throughout the crystal even at the edge. However, determining the distribution of these nanoparticles within the crystals was impossible because the sample sections were relatively thick and the crystallographic angle for the exposed surfaces was not known.

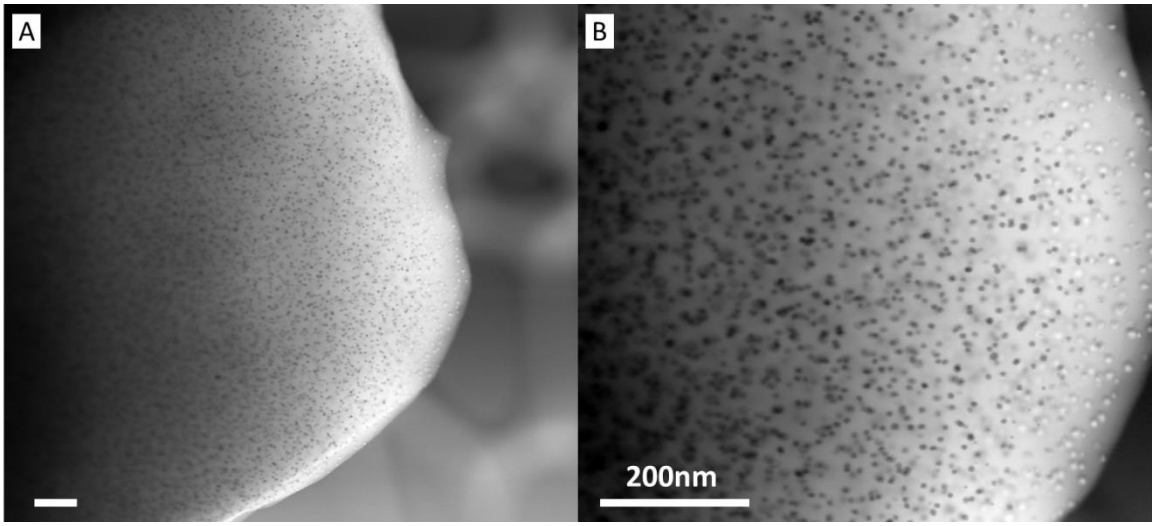

Figure 6.5 HAADF images of AuNP [high] composite crystals.

All scale bars are 200 nm.

Scanning electron microscopy (SEM) images were obtained of the crystal surfaces and used to analyze the arrangement of nanoparticles at or near the surface. Since SEM images are acquired for just one plane of the crystals the influence of depth, which plagued the analysis of TEM images was eliminated. Figure 6.6 are SEM images obtained from the surface of control, AuNP_[low], AuNP_[high] and AunRod samples. The lysozyme control sample is smooth without any pitting. The AuNP composite crystal surfaces have shadowy pits that are on the scale of the 10 nm particles and the AunRod crystal surface clearly shows the large gold nanorods. The AuNP_[high] sample image was adjusted for contrast and brightness then analyzed using ImagePro software to perform radial distribution functions and determine the average distance between particles and their first and second closest neighbor.

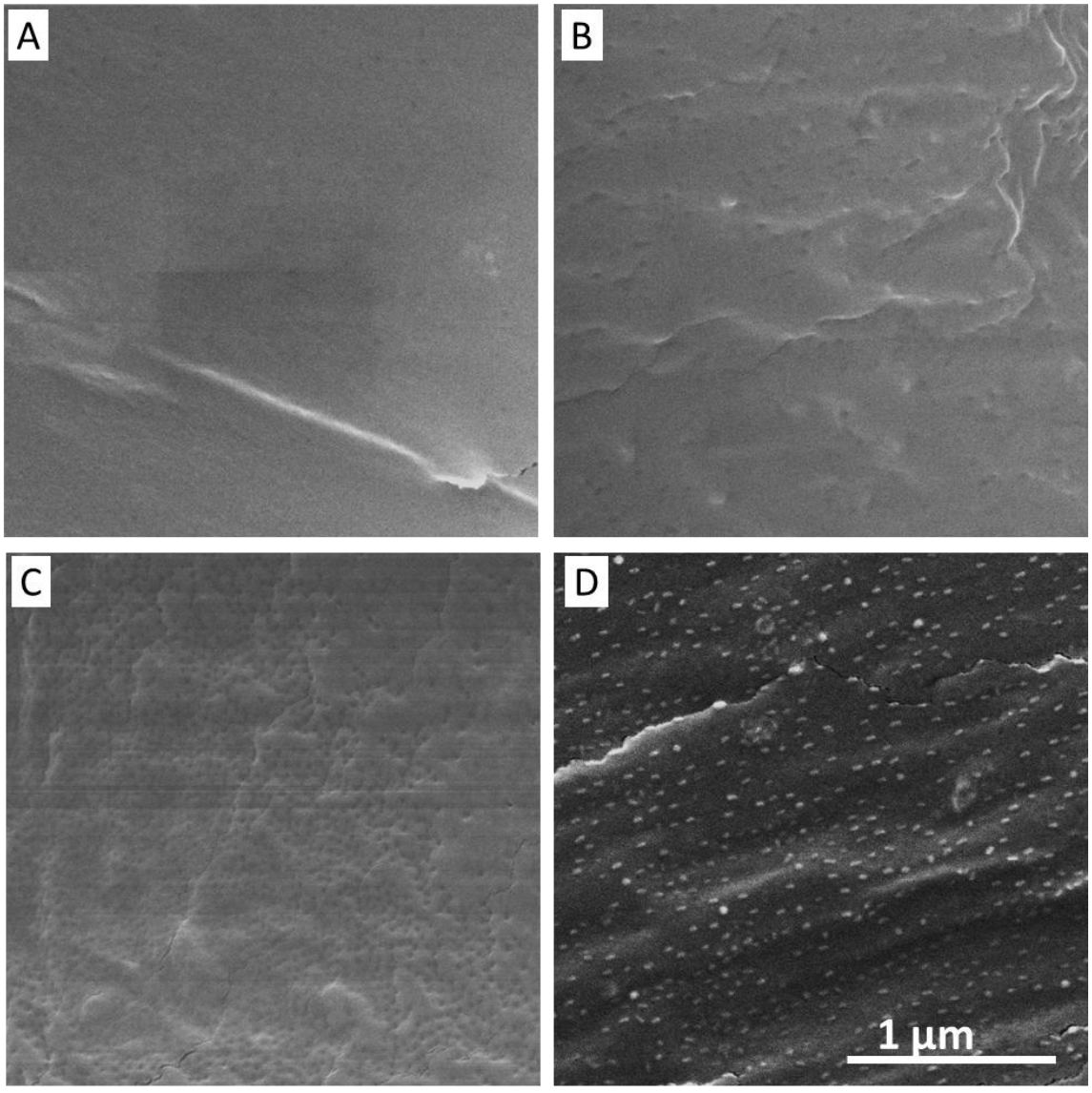

Figure 6.6 SEM images of crystal surface

SEM images of a crystal surface for the control sample (A), AuNP_[low] (B), AuNP_[high] (C) and AunRod (D) composite crystals.

This analysis revealed that the distribution of 10 nm gold nanoparticles was not entirely random; there was a fairly narrow average distance and some consistency in the interparticle arrangements. Figure 6.7 shows the adjusted AuNP_[high] SEM image from which a mask was generated to determine the center position for all the darkened divots on the surface. Next, the coordinates for the particles were used to determine the distances between single particles and all other particles in the image (1355). The distances were used to determine the average spacing for the closest and second closest neighbors. The histograms shown in Figure 6.7B are the distances to first and second closest neighbors for 123 particles chosen at random revealing an average to 47.5 ± 1.9 nm and 63.0 ± 3.4 nm, respectively. The low variance in distances suggests that the particles are regularly spaced.

Next, the position of a central particle was used to calculate the radial distribution function (RDF), g(r), for the arrangement. RDFs are used to determine how a distribution of particles varies based on the distance from a reference particle. First, the number of particles (n) within a given area away from the central particle was calculated for the whole image in 10 nm incremented radial changes. Then the number of particles per volume of the shell ($V_{radial\ shell}$) was determined where $V_{radial\ shell}$ was approximated using equation 6.1; where r, was the radial distance from the particle and δr, was the incremented change (10 nm).

Equation 6.1. Volume of the radial shell

$$\mathbf{V_{radial\ shell} = 4\pi r^2 \delta r}$$

Then g(r) is calculated using equation 2; where N was the total number of particles and V_{total} was the the total image analyzed:

Equation 6.2. Radial distribution function

$$\mathbf{g(r) = \frac{n}{V_{shell}} \times \frac{N}{V_{total}}}$$

The RDF for the AuNP_[high] sample is shown in Figure 6.7C&D are consistent with 10 nm particles at arranged spacings within 250 nm of the central particle. Further away the distributions become more irregular.

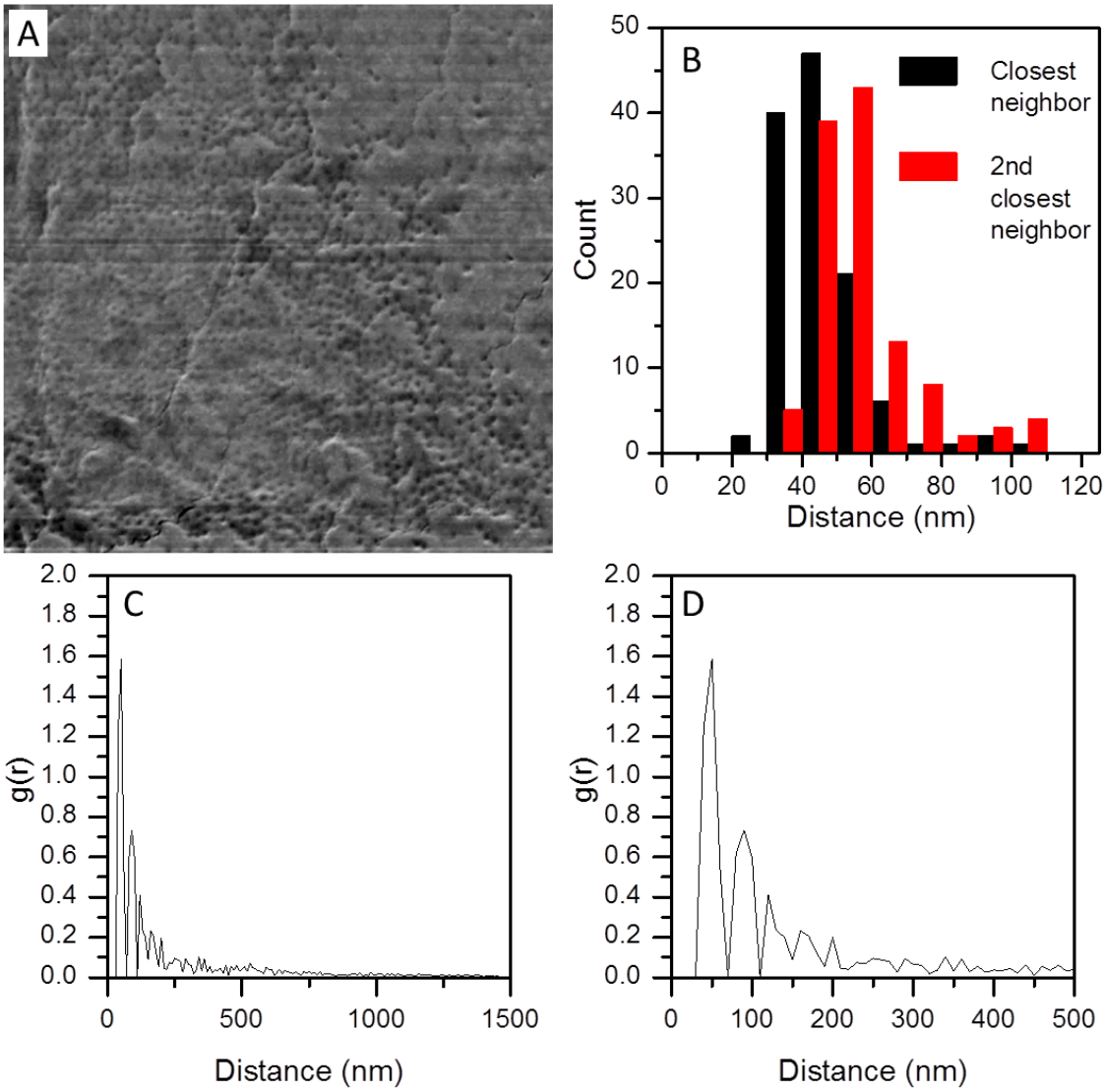

Figure 6.7 SEM image and analysis for nanoparticle arrangement in AuNP [high] crystal

(A) The SEM image from Figure 6 of the AuNP_[high] crystal surface was enhanced for contrast and brightness. (B) Average distance to first and second closest neighbors was found to be 47.5 ± 1.9 nm and 63.0 ± 3.4 nm, respectively. The radial distribution function from a single central particle for (C) 1.5 μm and (D) 0.5 μm area around the central particle.

These data allow us to better understand the optical data presented in Chapter 5.2.4. Interparticle distances must be less than twice the diameter of gold nanoparticles in order to couple plasmon resonances in adjacent gold nanoparticles. Here their spacing was on the order of five times their diameter.[3]

The evaluation of the gold nanorods based on the center to center distance and RDF are shown in Figure 6.8 and were calculated for the surface exposed nanoparticles in the SEM images in a fashion similar to that applied to the spherical nanparticles. The center to center distance between nanorods was found to be 79.4 ± 8.7 nm. The RDF for the rods showed a similar trend in arrangement, namely a regularity in the spacing for the distribution within two neighbors. However, more significant in this anlaysis was the degree of alignment for the exposed rods.

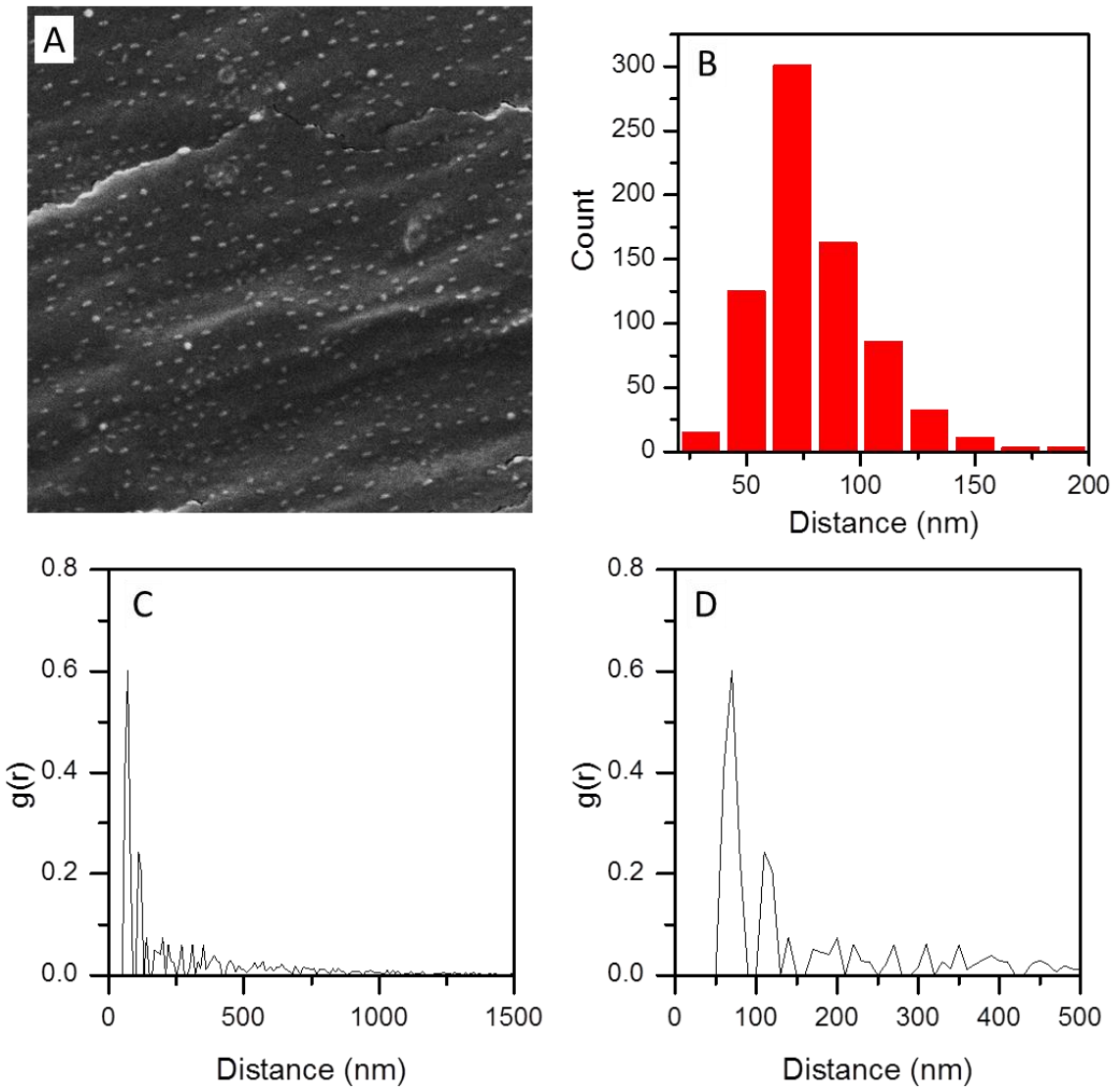

Figure 6.8 Image and analysis of arrangement of AunRod composite crystal

(A) The SEM image from Figure 6 of the AunRod composite crystal. (B) Average distance to the closest neighboring particle, 79.4 ± 8.7 nm. The radial distribution function from a single central particle for (C) 1.5 μm and (D) 0.5 μm.

Nanorods are highly aligned on the surface and within the interior of the composite crystals, Figure 6.9. Composite crystals were evaluated based on the particles that could be visualized both on the surface of the crystal and within the interior; crystals were embedded in resin and sliced in half to image deeper into the crystal. Analysis of the SEM images show the nanorods on the surface align within 21.4° of the average angle (1050 particles, even without correcting for surface defects) and within 11.2° for all interior rods (180 particles). These highly aligned particles show different orientations on each of the faces, Figure 6.9C shows the intersection of two faces of the crystal with rods aligning perpendicular to the long axis of the crystal, but also orthogonal to each other. Images obtained over a large area of a single face showed all the rods oriented the same way across the face.

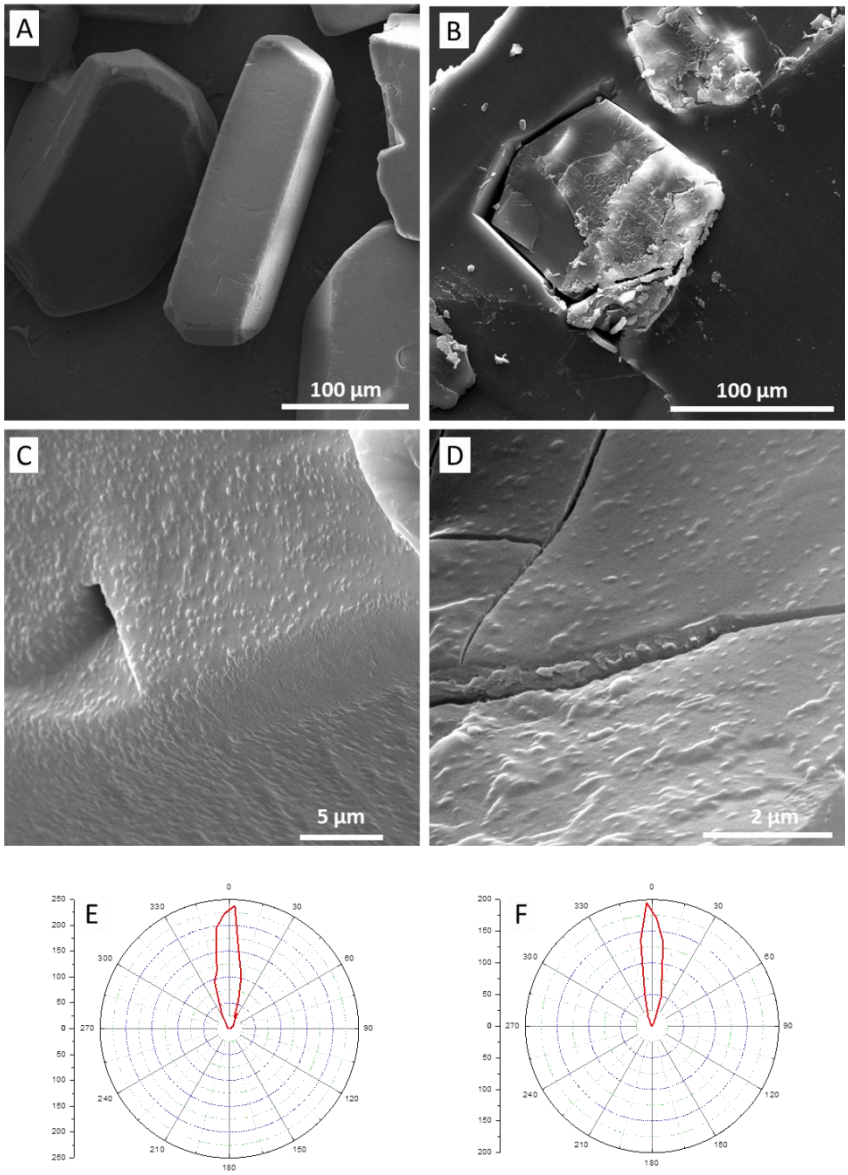

Figure 6.9 Nanorod Alignment Images and Analysis

(A & C) Nanorods at the surface of as prepared protein crystals and (B &D) the interior of resin embedded, crystals that were sliced in half. Polarization plots were used to show the nanomaterials alignment throughout the crystal sample, (E) surface rods, (F) interior rods.

6.2.4. Polarization dependent optical signal from aligned nanorods

The long range alignment of the nanorods within the composite crystal leads to a strong polarization dependent optical signal in the longitudinal peak spectrum. Figure 6.10 shows the optical properties of the crystals as collected on a single crystal at two locations. The arrangement of the eight {110} segments form the characteristic hourglass shape in image A. From the SEM data it was determined that the gold nanorods align perpendicular to the long axis of the crystal, and that the faces align perpendicular to each other. Therefore, along the {101} surfaces facing towards and away from the camera the rods would be oriented parallel with the direction of the slits, and the rods within the faces on the left and right sides would be pointed towards the camera. This orientation of the rods would look like a sphere to the camera and incident light, which should show no interaction with the polarized light.

Image A and spectrum D show that the {101} segments on the two sides of the crystal do not interact with polarized light and are therefore arranged with the long axis towards the camera. However, the loss of color and decreased spectral absorbance for the top and bottom areas crystal is notable. It suggests that the long axis of the rods interacts with polarized light; at 0 degrees the polarized light is parallel to the slit direction while at 90 degrees the incident light is perpendicular to the long axis of the rod.

Protein crystals are known to interact with polarized light, and so we checked that the observed polarization properties were due to rod alignment and not to the native crystals themselves. Single crystal polarization dependent spectrum was collected for spherical AuNP composite crystals as well. The decrease in absorbance at the peak position for the

two domains of the spherical AuNP crystals were 25% and 20%. The non-interacting domain of the composite crystal had a decrease in absorbance of 29%, while the interacting domain decreased in absorbance by 64%. Therefore the reflections within the crystal may account for up to ~30% of the polarization dependent decrease in the absorbance spectrum, but the interacting, aligned anisotropic materials have a more significant decrease in optical absorbance.

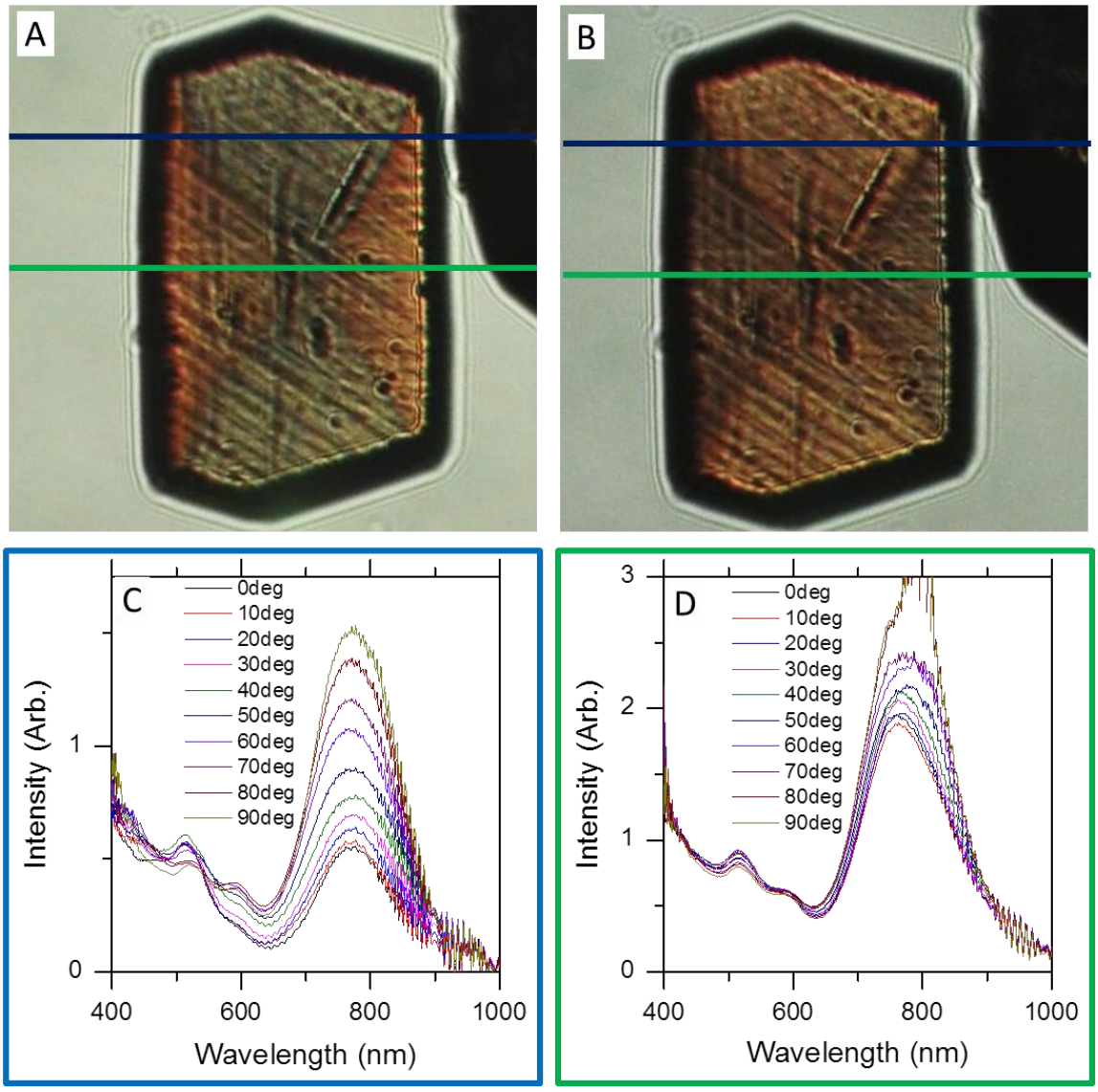

Figure 6.10 Polarization of AunRod Composite Crystal

Images of a single AuRod composite crystal for two incident light polarization positions; (A) at 0 degrees and (B) 90 degrees. Polarization dependent absorbance spectra collected on the crystal in 10 degree increments at two slit positions, (C) for the slit represented by the blue line position and (D) the green line position.

6.2.5. Mechanism of arrangement

The incorporation and arrangement of nanoparticles at regular distances within the protein crystal is reflective of the fact that the nanoparticles help form protein crystal nuclei; for lysozyme, these nuclei have been studied via both light scattering and diffraction. Most studies find that they consist of four or more lysozymes with dimensions near 9 to 18 nm.[15,16] In this the presence of nanoparticles, these proto-nuclei form in and around nanoparticle-polymer conjugates that can themselves can have polymer shells as thick as 30 nm. This would suggest that incorporated nanoparticles could have as much as 40 to 50 nm of surface polymer and protein surrounding them, giving rise to a lower limit for the interparticle separations that is in good agreement with that found from the radial distribution function (e.g. 47 nm). The composites grow when these proto-nuclei encounter other similar structures and begin to crystallize, leading to the formation of composite crystals.

Alignment of the anisotropic materials is believed to be due to increased interactions with the protein on the higher radius of curvature ends of the nanoparticles. For spherical nanoparticles the radius of curvature polymers of sufficient length are less extended, yet as the nanoparticle radius increases the polymer extension increases to a brush conformation[17]. This would prevent protein association with the long sides of the rod, and create proto-nuclei more at the ends of rods. Accumulation of proteins increases the protein – protein associations and leads to the nucleation of crystal growth preferentially at the ends in a matter that decorates their tips. These then link with other tip-decorated rods to form aligned arrays.

6.3. CONCLUSION

Evaluation of the arrangement of nanoparticles within composite crystals was approached via four methods. Visually, composite crystals show controlled distributions of nanoparticles throughout their structure, but no information can be obtained about the nanometer scale spatial arrangements. More quantitative approaches such as diffraction were also of limited utility, primarily because peaks from the lysozyme crystal itself overwhelmed any weaker scattering patterns from aligned nanoparticles. Electron microscopy resolved the particles on the nanometer scale, but for transmission electron microscopy the inability to look along specific axes made it challenging to assess the arrangement of nanoparticles. SEM proved to be most useful for detecting nanoparticles in a single plane and showed some regularity in spacing and a high degree of alignment for anisotropic materials. Long range alignments of anisotropic materials were confirmed with single crystal polarization dependent spectroscopy. Through surface design it was possible to produce concentrated composites of a variety of nanoparticles with some degree of control over interparticle spacing as well as rod alignment.

6.4. REFERENCES

(1) Alivisatos, A. P. *Science* **1996**, *271*, 933.

(2) Takeda, Y.; Kondow, T.; Mafuné, F. *Chemical Physics Letters* **2011**, *504*, 175.

(3) Rechberger, W.; Hohenau, A.; Leitner, A.; Krenn, J. R.; Lamprecht, B.; Aussenegg, F. R. *Optics Communications* **2003**, *220*, 137.

(4) Funston, A. M.; Novo, C.; Davis, T. J.; Mulvaney, P. *Nano Letters* **2009**, *9*, 1651.

(5) Kohei Tai, W. L., Ikurou Umezu, Akira Sugimura *Appl. Phys. Express* **2010**, *3*, 035202.

(6) Simserides, C. D.; Hohenester, U.; Goldoni, G.; Molinari, E. *physica status solidi (b)* **2001**, *224*, 745.

(7) Xu, X.; Stöttinger, S.; Battagliarin, G.; Hinze, G.; Mugnaioli, E.; Li, C.; Müllen, K.; Basché, T. *Journal of the American Chemical Society* **2011**, *133*, 18062.

(8) Kechrakos, D.; Trohidou, K. N. *Applied Physics Letters* **2002**, *81*, 4574.

(9) Nakata, K.; Hu, Y.; Uzun, O.; Bakr, O.; Stellacci, F. *Advanced Materials* **2008**, *20*, 4294.

(10) Yang, H. T.; Hasegawa, D.; Takahashi, M.; Ogawa, T. *Applied Physics Letters* **2009**, *94*, 013103.

(11) Oonishi, T.; Sato, S.; Yao, H.; Kimura, K. *Journal of Applied Physics* **2007**, *101*, 114314.

(12) Taleb, A.; Petit, C.; Pileni, M. P. *The Journal of Physical Chemistry B* **1998**, *102*, 2214.

(13) Hsu, C.-C.; Hsu, R.-Q.; Wu, Y.-H. *Journal of Electron Microscopy* **2010**, *59*, S149.

(14) Guli, M.; Lambert, E. M.; Li, M.; Mann, S. *Angewandte Chemie* **2010**, *122*, 530.

(15) Georgalis, Y.; Umbach, P.; Raptis, J.; Saenger, W. *Acta Crystallographica Section D* **1997**, *53*, 691.

(16) Yaminsky, I.; Gvozdev, N.; Sil'nikova, M.; Rashkovich, L. *Crystallography Reports* **2002**, *47*, S149.

(17) Hill, H. D.; Millstone, J. E.; Banholzer, M. J.; Mirkin, C. A. *ACS Nano* **2009**, *3*, 418.

CONCLUSION

The work documented within this thesis aimed to accomplish three main goals: 1) understand and control protein association through surface engineering of nanoparticles, 2) use the protein – nanoparticle association for protein crystal nucleation and 3) manipulate nanoparticles into three dimentional assemblies using mesoscopic biotemplates.

First, protein-nanoparticle associations were found to be dependent on the polymer surface grafting density for poly(ethylene glycol) (PEG) coated 10 nm gold nanoparticles. Two analytical methods: analytical ultracentrifugation (AUC) and total organic carbon analysis (TOC), were developed to quantitatively measure the polymer grafting density on small volumes of polymer – nanoparticle conjugates in solution. These methods were validated, evaluated for sensitivity and used to characterize grafting density trends based on molecular weight and nanoparticle diameter. The two main parameters that can be used to lower grafting density to allow for nanoparticle – protein associations are decreased polymer concentrations or increased molecular weights. Nanoparticles with incomplete polymer coverages have lower grafting densities, but are not stable in ionic solutions, such as biological media or buffers. Increasing the molecular weight of the PEG coating on the nanoparticles allow for lower surface grafting densities while maintaining the stability in solution. Therefore, large molecular weight coated nanoparticles are able to remain dispersed and isolated in solutions and exhibit protein associations.

Sterically stabilized large molecular weight polymer coated nanoparticles associate with lysozyme and act as heterogeneous crystal nucleants: increasing crystal counts, decreasing sizes and times to nucleation and increasing the chance of obtaining crystallization hits using high throughput sparse matrix screening strategies. In contrast, uncoated citrate stabilized gold nanoparticles are unable to remain disperse in the high ionic strength crystallization buffers. These particles fall out of solution and have little to no impact on protein crystallization. Similarly, short molecular weight polymer-coated nanoparticles, which do not exhibit protein association, have little to no influence on protein crystallization. Nanoparticle nucleants in the protein stock solution are easily incorporated into high throughput crystallization strategies where they increase the crystal forming conditions while also decreasing the precipitate forming conditions for a diverse set of six proteins: ferritin, human serum albumin, lipase b, xylanase, glucose isomerase and lysozyme.

Finally, nanoparticles coated with large molecular weight PEG were incorporated into the protein crystal lattice forming mesoscopic, three dimensional, biotemplated, architectures of well-formed nanoparticles. Surface modification of nanoparticles, such as coating with PEG, can be used to form composite crystals with nanomaterials of a wide range of sizes (7.5 – 42 nm), shapes (cube, bipyramid, rod and high aspect ratio rods) and core compositions (iron oxide, cerium oxide and quantum dots). Based on interparticle distances, nanomaterials exhibit optical, fluorescent and magnetic properties that can differ from the size dependent properties of the same materials dispersed in solution. For gold nanoparticle composite crystals it was determined that the distance between particles must be greater than twice their diameter and therefore, no significant spectral shifts were

observed (over those attributed to the change in refractive index). Increased quantum yields for quantum dot composite crystals are an indication that the incorporated nanomaterials were separated more than twice their diameter. Additionally, the magnetic response of iron oxide nanoparticles changed after incorporation as indicated by the inability of constrained, isolated nanoparticles to coordinate their spins which is necessary to exhibit a magnetic response. While these properties consistently point to a large separation of nanomaterials, possibly the most interesting results come from the long range ordering of anisotropic nanorods. Analysis of nanorods on the faces and interior planes of crystals where they incorporated, showed less than 20 degree deviation from the average alignment angle. Polarization dependent optical properties confirmed the high degree of alignment was consistent throughout the crystal and produced a measurable decrease in the optical absorbance at the longitudinal absorbance peak.